Spring 2026 – Systems Biology of Reproduction
Discussion Outline – Gametogenesis / Stem Cells / Cloning
Eric Nilsson – Biol 475/575
10:35-11:50 am, Tuesday & Thursday
March 26, 2026
Week 11

Gametogenesis / Stem Cells / Cloning

Primary Papers:

1. Ball, et al. (2016) BMC Genomics 17:628
2. Yoshino, et al. (2021) Science 373:298
3. Guo, et al. (2020) Cell Stem Cell 26:262-276

Discussion

Student 16: Reference 1 above
- What was the experimental design?
- What are the different stages of prophase I of meiosis?
- Since each sample contained a mix of germ cells of different stages, how were certain genes associated to certain stages?

Student 17: Reference 2 above
- What are the technologies used?
- What are the limitations of organ cultures?
- What clinical applications could be considered?

Student 18: Reference 3 above
- What developmental stage and cell types were investigated?
- What technology was used, and what are its advantages compared to other technologies?
- What conclusions were made about the onset of testis function and gametogenesis?

BMC Genomics

CrossMark

Regulatory complexity revealed by integrated cytological and RNA-seq analyses of meiotic substages in mouse spermatocytes

Robyn L. Ball[1†], Yasuhiro Fujiwara[1†], Fengyun Sun[1], Jianjun Hu[1], Matthew A. Hibbs[1,2], Mary Ann Handel[1*] and Gregory W. Carter[1*]

Abstract

Background: The continuous and non-synchronous nature of postnatal male germ-cell development has impeded stage-specific resolution of molecular events of mammalian meiotic prophase in the testis. Here the juvenile onset of spermatogenesis in mice is analyzed by combining cytological and transcriptomic data in a novel computational analysis that allows decomposition of the transcriptional programs of spermatogonia and meiotic prophase substages.

Results: Germ cells from testes of individual mice were obtained at two-day intervals from 8 to 18 days post-partum (dpp), prepared as surface-spread chromatin and immunolabeled for meiotic stage-specific protein markers (STRA8, SYCP3, phosphorylated H2AFX, and HISTH1T). Eight stages were discriminated cytologically by combinatorial antibody labeling, and RNA-seq was performed on the same samples. Independent principal component analyses of cytological and transcriptomic data yielded similar patterns for both data types, providing strong evidence for substage-specific gene expression signatures. A novel permutation-based maximum covariance analysis (PMCA) was developed to map co-expressed transcripts to one or more of the eight meiotic prophase substages, thereby linking distinct molecular programs to cytologically defined cell states. Expression of meiosis-specific genes is not substage-limited, suggesting regulation of substage transitions at other levels.

Conclusions: This integrated analysis provides a general method for resolving complex cell populations. Here it revealed not only features of meiotic substage-specific gene expression, but also a network of substage-specific transcription factors and relationships to potential target genes.

Keywords: Meiosis, Spermatogenesis, Maximum covariance analysis, Mouse, Transcriptome, RNA-seq

Background

Spermatogenesis is a complex developmental process with a unique cell division, meiosis, as a major defining event. The entire process includes maintenance of a small population of spermatogonial stem-cells, mitotic divisions of differentiating spermatogonia, meiotic prophase and ensuing divisions of spermatocytes, and post-meiotic differentiation of spermatids, by a process known as spermiogenesis. In mammalian testes, spermatogenesis occurs within seminiferous tubules, where all germ cells associate with one kind of somatic cell, the Sertoli cell, which provides the appropriate niche and microenvironment for the spermatogenic process. The adult testis is characterized by presence of all of the cells types in the spermatogenic lineage, with waves of differentiation throughout the testis propelled by retinoic acid signaling [1]. In mice, the first wave of spermatogenesis is initiated by spermatogonia shortly after birth, producing a sequential and orderly appearance of each of the more differentiated stages at regular intervals though the first four weeks of life. Although semi-synchronous with respect to the advancing wave of the most differentiated cells, the juvenile onset of

* Correspondence: maryann.handel@jax.org; greg.carter@jax.org
†Equal contributors
[1]The Jackson Laboratory, Bar Harbor, ME, USA
Full list of author information is available at the end of the article

Ball et al. BMC Genomics (2016) 17:628

Page 2 of 17

spermatogenesis also includes regular and asynchronous initiation of subsequent waves of spermatogenic differentiation. This asynchronous and continuous process of spermatogenesis has made it difficult to achieve molecular characterization of specific cell types in the lineage. This has been particularly the case with respect to analysis of the defining process of gametogenesis, meiosis, which occurs in spermatocytes. The complex events of meiosis I prophase include recombination, homologous chromosome pairing, and synapsis, taking place as spermatocytes progress through the leptotene, zygotene, pachytene and diplotene substages. These events culminate in the first meiotic division, a reductive division in which homologous chromosomes are separated, producing secondary spermatocytes that rapidly undergo the second, equational, meiotic division to produce haploid round spermatids. Because of the genetic importance of meiotic recombination for the production of chromosomally normal gametes and offspring, there has been great interest in elucidating the molecular hallmarks and their underlying transcriptional signatures that define the meiotic spermatocyte substages.

Toward the goal of achieving a molecular understanding of spermatogenesis, considerable effort has been devoted to separation of specific germ-cell differentiation substages from the histologically complex seminiferous epithelium. A widely used approach, commonly known as the "STA-PUT" sedimentation process [2–4], involves enzymatic dissociation of germ and somatic cells and enrichment for specific stages by cell-size-based sedimentation at unit gravity on a bovine albumin gradient. Reasonably good enrichment of the most uniquely sized cells (large pachytene spermatocytes and small round spermatids) can be obtained from testes of adult mice. However, many cells of interest (spermatogonia, early meiotic prophase spermatocytes) are not retrieved from adults because of their anatomical position bounded by Sertoli cell tight junctions. While these early cell types can be retrieved from juvenile testes, the amount of biological material required is daunting and enrichment is not robust. Isolation of specific cell types by fluorescence-activated cell sorting, FACS [5–8] is promising and becoming more widely applied; however sample sizes are small. Finally, rather than cell separation, total testis germ-cell populations can be collected in a developmental continuum during the first two to three weeks of juvenile development of mouse testes, to take advantage of the first wave of spermatogenesis. In this way, molecular features have been defined with respect to the sequential appearance of more advanced cell stages of spermatogenesis. This approach is useful primarily for correlating the appearance of a molecular entity to the developmental appearance of a specific cell type. However, the degree of resolution has been suboptimal, because gene or protein expression has not

been related to absolute frequencies of cell stages, a challenge we tackle in this study.

Together, these methods for enriching or inferring spermatogenic (and meiotic) substages have contributed to studies over the past decade on the developmental transcriptome of mammalian spermatogenesis, as recently reviewed [9]. Most such studies have taken advantage of microarrays querying known coding sequences [6, 10–12], and thus sequence-biased, but also provided interesting views of alternative splicing and other features of the spermatogenic transcriptome [13], and identified previously unknown potential targets for contraception and fertility [14]. More recently, methods for unbiased high-throughput deep sequencing of the transcriptome by RNA-seq have been employed [5, 15–19]. These studies have revealed unappreciated regulation of piRNAs [17], and global whole-genome views of the male germ-cell transcriptome [5, 18, 19]. However, the challenge for all transcriptomic analyses, particularly RNA-seq approaches, has been to computationally deconstruct the entire testis or germ-cell transcriptome into substage-specific transcriptomes. This is an important goal, given both the abundance and complexity of RNA species in the testis, particularly with respect to the imputed contribution of both coding and non-coding RNA from spermatocytes and spermatids [19]. In one example of such a computational approach, frequencies of specific germ-cell stages throughout the first wave of spermatogenesis previously published in another analysis [4] were used to estimate cell type-specific expression patterns in a separate data set [18]. While coming closer to the goal of substage-specific transcriptomes, this study relied on a low sample size and on integrating non-contemporaneous data. Other approaches [5, 6], employed cell sorting by FACS and subsequent validation of purity by meiotic markers. While these studies have yielded important insights into global gene expression switches, they rely on FACS, not always available or practical for small samples, such as from infertile mutant models.

Here we have tackled the problem of deconvolving transcriptomes of complex germ-cell populations into stage-specific transcriptomes by computationally integrating highly detailed and combinatorial cytological staging of the same cell samples as subjected to RNA-seq analysis. Deep and accurate cell stage phenotyping was conducted using antibodies to STRA8, SYCP3, phosphorylated H2AFX, and HISTH1T, all exhibiting meiotic substage specificity of expression and/or localization. By collecting highly enriched germ-cell populations from testes at two-day intervals through the first wave of spermatogenesis, and by multiple sampling of individual mice (30 total) for both cytological composition and RNA composition by high-throughput sequencing, we developed an unusually deep data set that portrays variation in cell substage

Ball *et al. BMC Genomics* (2016) 17:628

Page 3 of 17

composition and transcript abundance. To decompose these data into substage-specific transcriptome patterns in an unbiased way, we chose a nonparametric solution with minimal assumptions about data structure, thus developing a novel permutation-based maximum covariance analysis. This method enabled us to assign co-expressed transcripts to one or more meiotic substages, thereby linking distinct molecular programs to cytologically defined cell states. Moreover, to better understand the regulation of each germ-cell substage transcriptome, we integrated transcription factor information to identify some of the key molecular regulators driving these cell stages. This approach provides a model for deconvolving transcriptomes of complex cell populations with well-defined cytological

attributes. Together, these data provide an unprecedented view of the complexity of meiotic transcription programs and their coordinate regulation.

Results

Experimental design

Germ cells were obtained from individual mice at two day intervals from 8 dpp to 18 dpp ($N = 5$ biological replicates at each age; $N = 30$ samples total) and divided into two aliquots, one for cytology and one for RNA-seq (Fig. 1a). For the C57BL/6J (B6) strain used in this study, this developmental window captures the initial differentiation of spermatogonia into early leptonema, through the stages of pachynema and diplonema. For each sample,
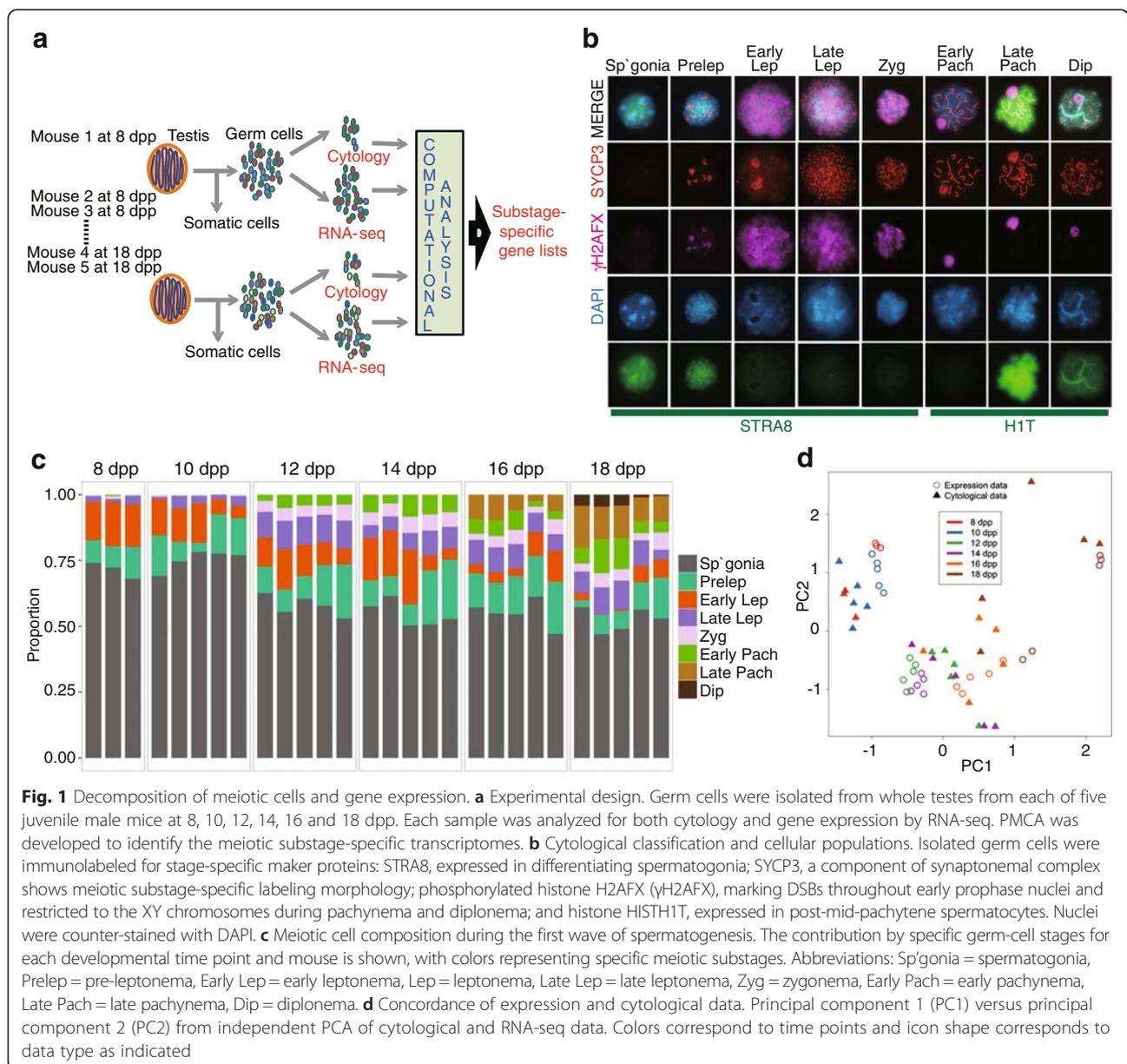

Fig. 1 Decomposition of meiotic cells and gene expression. **a** Experimental design. Germ cells were isolated from whole testes from each of five juvenile male mice at 8, 10, 12, 14, 16 and 18 dpp. Each sample was analyzed for both cytology and gene expression by RNA-seq. PMCA was developed to identify the meiotic substage-specific transcriptomes. **b** Cytological classification and cellular populations. Isolated germ cells were immunolabeled for stage-specific maker proteins: STRA8, expressed in differentiating spermatogonia; SYCP3, a component of synaptonemal complex shows meiotic substage-specific labeling morphology; phosphorylated histone H2AFX (γH2AFX), marking DSBs throughout early prophase nuclei and restricted to the XY chromosomes during pachynema and diplonema; and histone HISTH1T, expressed in post-mid-pachytene spermatocytes. Nuclei were counter-stained with DAPI. **c** Meiotic cell composition during the first wave of spermatogenesis. The contribution by specific germ-cell stages for each developmental time point and mouse is shown, with colors representing specific meiotic substages. Abbreviations: Sp'gonia = spermatogonia, Prelep = pre-leptonema, Early Lep = early leptonema, Lep = leptonema, Late Lep = late leptonema, Zyg = zygonema, Early Pach = early pachynema, Late Pach = late pachynema, Dip = diplonema. **d** Concordance of expression and cytological data. Principal component 1 (PC1) versus principal component 2 (PC2) from independent PCA of cytological and RNA-seq data. Colors correspond to time points and icon shape corresponds to data type as indicated

Ball *et al. BMC Genomics* (2016) 17:628

Page 4 of 17

we determined the relative numbers of cells of each substage by cytological criteria (N = about 400 germ cells per mouse, for a total of 11,990 germ cells scored cytologically by criteria described below); by scoring germ cells from each individual mouse, we captured variability between mice. The purity of germ cells in each sample, computed as germ-cell count divided by total DAPI-stained cell count, was greater than 90 % for all samples. Upon inspection of both cytological and RNA-seq data, two germ-cell samples collected at 8 dpp revealed poor concordance with age-matched samples, likely due to insufficient cell numbers for successful RNA-seq library preparation (Additional file 1: Table S1); thus these samples were omitted from all subsequent analyses (final N = 28).

Cytological deconvolution of the meiotic substage composition of germ cells during the first wave of spermatogenesis

Germ-cell substage frequencies in each cytological preparation were determined by combinatorial immunolabeling with antibodies to meiotic substage marker proteins, scoring 400 germ cells per mouse. Marker proteins assessed were STRA8, a meiosis-initiating factor [20] present in differentiated spermatogonia and some leptotene spermatocytes; SYCP3, a synaptonemal complex (SC) protein present in the chromosomal axes of leptotene and zygotene spermatocytes, in the lateral elements of the mature SC in pachytene spermatocytes, and disassembling in diplotene spermatocytes [21, 22]; the phosphorylated form of histone H2AFX (PH2AFX, also known as γH2AX), which localizes to chromatin surrounding DNA double-strand breaks (DSBs) in characteristic patterns that discriminate early meiotic prophase from the pachytene and diplotene stages [22, 23]; and the testis germ cell-specific histone H1 variant HIST1H1T (herein referred to by its common designation of H1T), which is a marker of the mid-to-late pachytene stage [22]. The combinatorial labeling patterns for each marker protein allowed categorization of germ cells of each sample into eight substages, achieving a higher degree of meiotic

substage discrimination than previous transcriptome analyses (Table 1 and Fig. 1b).

Together, these data provide a comprehensive picture of postnatal spermatogenic progress through meiotic prophase of the first wave of differentiating cells for comparison to data previously obtained by histological analyses [4]. At every time point in the current data, greater than 50 % of the retrieved germ cells were spermatogonia (Fig. 1c), reflecting continually initiating separate waves of spermatogenesis. Representation of these cells decreased over time (Fig. 1c), likely due to initiation of additional waves of meiotic cells, increasing numbers of post-spermatogonial spermatocytes, and establishment of cell junctions that impede cell retrieval. Throughout this period, due in part to initiation of subsequent waves of spermatogenesis, the average contribution to the total germ-cell population by preleptotene and leptotene spermatocytes remained relatively constant (Fig. 1c), thus reducing the power to identify transcripts specific to just these substages. The first appreciable numbers of H1T-negative early pachytene spermatocytes were observed at 12 dpp, and H1T-positive late-pachytene cells were abundant by 16-18 dpp, consistent with previously published data [24]. By 18 dpp, less than 10 % of the cells had progressed to the diplotene stage, and only about 0.1 % to metaphase. Overall substage frequencies were similar at 8 and 10 dpp, and also at 12 and 14 dpp (Fig. 1c). For computational analyses (below), we combined substages that exhibited similar frequency patterns across the developmental time span, specifically late leptotene and zygotene substages, and late pachytene and diplotene substages.

High concordance of gene expression and cytological data

To assess the feasibility of associating gene expression with cytologically-defined substages, we performed independent principal component analyses (PCA) on each data set. The high concordance between the cytological frequency of cell substages and RNA expression data (Fig. 1d) suggested that changes in gene expression in pooled germ cells can be explained by variation in cytological proportions of the

Table 1 Immunolabeling criteria for cell types and meiotic substages

Substages	SYCP3	γH2AX	STRA8	H1T
Spermatogonia[a]	None	Negative	Positive	Negative
Preleptonema	Patches	Negative	Positive	Negative
Early Leptonema	Patches	Positive	Positive	Negative
Late Leptonema	Fine foci	Positive	Weakly positive	Negative
Zygonema	Partially paired	Patches	Negative	Negative
Early Pachynema	Paired	Restricted to XY body	Negative	Negative
Late Pachynema	Paired	Restricted to XY body	Negative	Positive
Diplonema	Partially dissociated	Restricted to XY body	Negative	Positive

[a]Spermatogonia are a separate mitotic stage, not a meiotic substage

Ball *et al. BMC Genomics* (2016) 17:628

Page 5 of 17

differentiation states during spermatogenesis. Although cells in different substages may contribute different amounts of RNA to each sample, this analysis demonstrates an overall quantitative agreement between the two data types. This supported the validity of combining these two datasets to identify meiotic substage-specific transcriptional programs.

Meiotic substage-specific gene expression derived by covariance analysis

To identify signatures for meiotic substage-specific gene expression, we developed a novel permutation-based maximum covariance analysis (PMCA), which maps groups of co-expressed genes to combinatorial cytological marker-based staging based antibodies to STRA8, SYCP3, phosphorylated H2AFX, and HISTH1T. This statistical approach demonstrates *concordance* of distinct cellular programs to each meiotic substage based on the similarity of "cyto-pattern" and "gene-expression pattern" across samples. In brief, the concordant patterns are derived from the most preeminent features of covariance between cytological and transcriptome data across all samples (Methods). In this RNA-seq dataset, a total of 15,025 Ensembl genes (http://www.ensembl.org) and 5267 NONCODE lncRNA genes [25] were detected (at

a Transcripts per Million (TPM) ≥ 3) in at least one sample of the isolated germ cells. We also detected piRNA precursors transcripts that had previously been identified [17] with appropriate substages, although they are not the focus in the current study. Through PMCA, we identified 1235 spermatogonia genes and 6052 meiosis substage-specific genes. Expression of many transcripts could not be assigned to distinct substages and instead, were shared across several consecutive substages; 131 genes were shared among late leptotene, zygotene, and early pachytene stages while 106 genes were shared among early pachytene, late pachytene, and diplotene stages (Fig. 2; Additional file 2: Figure S1; Table 2; Additional file 1: Table S2). Notably, increased numbers of expressed genes were observed at 16 dpp when cells first reach the late pachytene stage (Table 2; Additional file 1: Table S2).

In addition to identifying genes concordant with specific substages, PMCA also identified genes that were *negatively concordant* with specific substages. The negatively concordant genes have patterns of expression that are opposite to the cytological patterns; thus negatively concordant defines gene expression that is lower when the cytological proportion of a specific substage is higher and vice versa (Fig. 2; Additional file 2: Figure S2; Table 2;
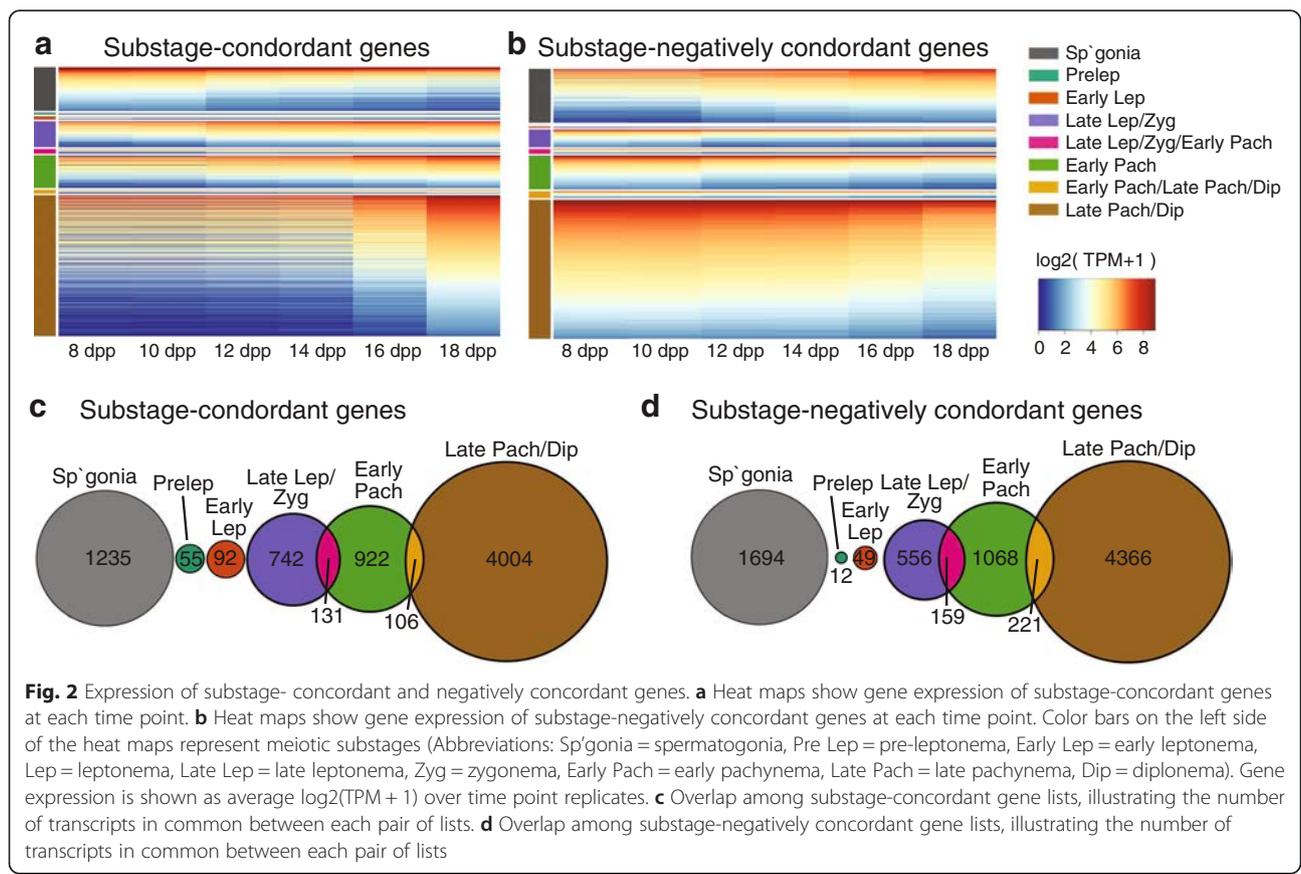

Fig. 2 Expression of substage- concordant and negatively concordant genes. **a** Heat maps show gene expression of substage-concordant genes at each time point. **b** Heat maps show gene expression of substage-negatively concordant genes at each time point. Color bars on the left side of the heat maps represent meiotic substages (Abbreviations: Sp'gonia = spermatogonia, Pre Lep = pre-leptonema, Early Lep = early leptonema, Lep = leptonema, Late Lep = late leptonema, Zyg = zygonema, Early Pach = early pachynema, Late Pach = late pachynema, Dip = diplonema). Gene expression is shown as average log2(TPM + 1) over time point replicates. **c** Overlap among substage-concordant gene lists, illustrating the number of transcripts in common between each pair of lists. **d** Overlap among substage-negatively concordant gene lists, illustrating the number of transcripts in common between each pair of lists

Ball *et al. BMC Genomics* (2016) 17:628

Page 6 of 17

Table 2 Substage-concordant and negatively concordant genes

Substage	Number of genes concordant	Number of genes negatively concordant
Spermatogonia[a]	1235	1694
Preleptonema	55	12
Early Leptonema	92	49
Late Leptonema/Zygonema	742	556
Late Leptonema/Zygonema/ Early Pachynema	131	159
Early Pachynema	922	1068
Early Pachynema/Late Pachynema/Diplonema	106	221
Late Pachynema/Diplonema	4004	4366

[a]Spermatogonia are a separate mitotic stage, not a meiotic substage

Additional file 1: Table S2). Genes detected as negatively concordant with one stage are often detected as concordant with another substage. For example, genes negatively concordant with spermatogonia are genes expressed across the meiotic cell substages, but not enriched in spermatogonia. Not surprisingly, the 1694 genes negatively concordant with spermatogonia were enriched for known meiotic genes. Indeed, among all genes expressed, many of those with known meiotic function and/or Gene Ontology annotation for meiotic function were not concordant with any single meiotic substage, but were expressed across meiotic substages.

Validation of substage-specific gene expression patterns

We bolstered and validated these computationally derived results in three distinctly different ways. First, gene expression analyses by qRT-PCR supported the RNA-seq expression data. Second, the validity of the PMCA procedure was queried by analysis of genes expressed in a highly enriched cell population of mid- to late-pachytene spermatocytes retrieved from adult testes by unit gravity sedimentation. Finally, we used our data to confirm a known pattern of male germ-cell specific gene expression, X-chromosome silencing during meiotic prophase.

We compared transcript expression patterns detected by RNA-seq to independent qRT-PCR assays. We tested representative genes among those increasing, decreasing, or showing little change in expression across the sequential time points, as well as genes known to be highly expressed in pachynema. Germ cells of 10 and 16 dpp males were subjected to qRT-PCR to determine expression of each tested gene relative to a reference housekeeping gene (*Actb*); data are shown in Additional file 2: Figure S3. The qRT-PCR assays reflected RNA-seq findings. For example, in 16 dpp samples we found elevated expression of pachytene-enriched genes and of genes shown by RNA-seq to increase in expression throughout

the juvenile period tested (Additional file 2: Figure S3). Overall, patterns of gene expression are mostly concordant between the two different quantification methods and between sample sets, although, as expected, RNA-seq provides finer resolution and higher information content.

We further validated the PMCA-derived meiotic substage transcriptomes by comparison to highly enriched adult pachytene spermatocytes obtained by sedimentation at unit gravity [2–4, 26], which sorts cells based on size, not cytology or DNA content ($N = 4$ samples, each from germ cells pooled from testes of 6 mice at 9 weeks of age). The purity of late pachytene/diplotene spermatocytes in this preparation was 90 % based on cytological immunostaining with antibodies to stage-specific proteins phosphorylated H2AFX, SYCP3, and HIST1H1T. RNA isolated from the size-enriched pachytene spermatocytes was subjected to RNA-seq, allowing us to compare genes expressed in the pachytene spermatocytes to the meiotic substage-specific gene lists derived by PMCA. Cross-referencing from this dataset, there was a highly significant enrichment of pachynema-expressed genes among the gene lists from later meiotic substages (hypergeometric tests, all $p < 2.86 \times 10^{-18}$), but there was no enrichment for pachytene genes in the gene lists for spermatogonia or the early substages of meiosis (Table 3). In fact, 99 % of the genes in the late pachytene/diplotene list were also found in the enriched adult pachytene spermatocyte samples.

Finally, we queried the meiotic substage-specific patterns of gene expression determined by PMCA by confirming meiotic sex-chromosome inactivation (MSCI), a well-known feature of meiotic gene expression. In spermatocytes, most of the axial length of X and Y chromosomes, which are non-homologous, is not paired or synapsed. By the onset of the pachytene stage of meiotic prophase, the unpaired regions of the sex chromosomes become transcriptionally inactivated [11, 27, 28]. We

Table 3 Representation of enriched pachytene spermatocyte genes in meiotic substages

Substage	Number represented/ total concordant	*p*-value
Spermatogonia[a]	614/1235	1
Preleptonema	17/55	1
Early Leptonema	28/92	1
Late Leptonema/Zygonema	550/742	1.2×10^{-09}
Late Leptonema/Zygonema/ Early Pachynema	97/131	9.0×10^{-03}
Early Pachynema	809/922	2.0×10^{-62}
Early Pachynema/Late Pachynema/Diplonema	102/106	1.3×10^{-15}
Late Pachynema/Diplonema	3955/4004	$<1.0 \times 10^{-62}$

[a]Spermatogonia are a separate mitotic stage, not a meiotic substage

Ball *et al. BMC Genomics* (2016) 17:628

Page 7 of 17

assessed expression of X-linked genes from our RNA-seq data; overall, 788 X-linked genes (and 24 Y-linked genes) were detected in the substage-associated gene lists. Of these, only 190 genes were detected in the highly enriched adult pachytene spermatocytes, providing evidence of robust MSCI. These 190 transcripts, which do not show any specific regional localization on the X chromosome, might reflect ongoing transcription and escape from MSCI, but, perhaps more likely, may represent stable transcripts persisting after inactivation. In the developmental transcriptome, the strongest X-linked gene signals are those represented in the negatively concordant gene lists (Table 4), that is, genes with expression pattern opposite to the cytologically determined frequencies of each substage. This strong signal is particularly apparent for genes in the late-pachytene negatively concordant list, which exhibit relatively constant expression from 8 to 14 dpp but then sharply decrease in expression at 16 and 18 dpp; this is evidence for pachytene substage MSCI. In addition to MSCI being revealed by the negatively concordant gene lists, there is also diminished representation of X-linked genes in gene lists concordant with later stages of meiotic prophase (Table 4). Overall, 730 X-linked genes appear to be down-regulated by pachynema to late pachynema, or even earlier (Fig. 3a) and only 58 X-linked genes with early expression are detected at later stages (Fig. 3b).

In conclusion, evidence from both MSCI and the transcriptome of highly enriched adult pachytene spermatocytes validates the PMCA-derived substage- transcriptome signatures derived by PMCA. Moreover, as discussed below, we find good concordance among our stage-specific gene lists and functions with those derived by other studies.

Enrichment analysis of meiotic substage gene expression

The PMCA-derived meiosis substage-specific gene lists, coupled with Gene Ontology (GO) analysis [29], can provide insight into meiotic and spermatogenic function. Genes assigned to each substage were ranked by their similarity score, a measure of how closely the gene's expression pattern follows the substage's cytological pattern. Using ranked lists, we performed a ranked GO analysis in GOrilla [30]; these ranked lists provide approximations of meiotic substage gene ontology. Significantly, many meiosis-specific genes are not prominently represented among the meiosis substage-specific gene lists derived by PMCA. However, GO terms for genes negatively concordant with spermatogonia were predominantly meiotic terms (16 out of 31 GO terms for process, all $p < 9.97 \times 10^{-4}$), confirming that meiotic genes tend to be expressed across multiple meiotic substages and not unique to a particular meiotic substage (Additional file 1: Table S3). Thus meiotic substage transitions are probably not acutely regulated at the level of transcription of many of the known meiotic genes, although among late leptonema/zygonema-associated GO terms, 8 out of 10 GO "biological process" terms were associated with meiosis regulation (all $p < 8.6 \times 10^{-4}$), and similar GO terms were also identified in the early pachynema gene list (13 out of 33 GO terms for process, all $p < 5.56 \times 10^{-4}$) (Additional file 1: Table S4). We extracted 447 genes for *M. musculus* that are associated with any GO terms containing "meiosis" or "meiotic" (www.mouse mine.org), and of these genes we considered the 404 genes which are expressed in our developmental time series (those genes not expressed in our time series might include female meiosis-related genes). We found that 229 (57 %) genes were not concordant with any specific substage, while 26 (6 %) were concordant with late leptonema and zygonema, 43 (11 %) were concordant with early pachynema, and 92 (23 %) were concordant with late pachynema and diplonema. Of meiotic terms that were negatively concordant with substages, 67 (17 %) were negatively concordant with spermatogonia and 97 (24 %) were negatively concordant with late pachynema and diplonema (Additional file 1: Table S5). GO terms for genes expressed in late meiotic prophase were significantly enriched for spermatogenesis, spermiogenesis and fertilization, reflecting transcription of mRNAs to be stored for later translation during the haploid phase

Table 4 Substage-specific X-linked gene analysis

Substage	X-linked Concordant	Y-linked Concordant	X-linked Negatively Concordant	Y-linked Negatively Concordant
Spermatogonia[a]	28	0	55	2
Preleptonema	2	0	0	0
Early Leptonema	2	0	1	0
Late Leptonema/Zygonema	34	2	6	0
Late Leptonema/Zygonema/Early Pachynema	3	0	1	0
Early Pachynema	21	1	41	0
Early Pachynema/Late Pachynema/Diplonema	0	0	13	0
Late Pachynema/Diplonema	14	3	329	9

[a]Spermatogonia are a separate mitotic stage, not a meiotic substage

Ball *et al. BMC Genomics* (2016) 17:628
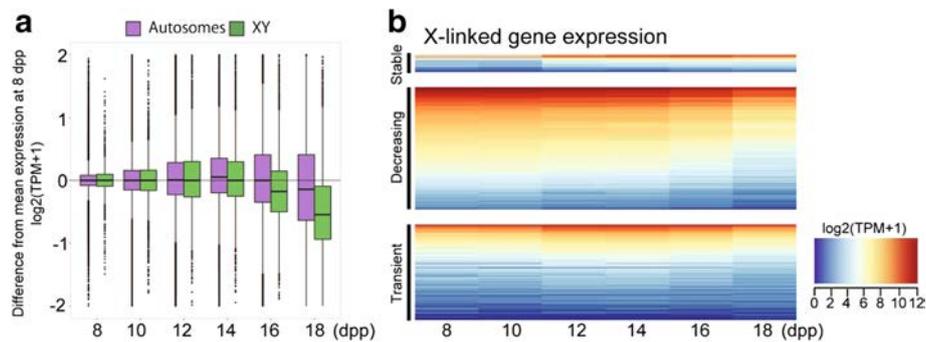
Page 8 of 17

Fig. 3 X-linked gene expression during the first wave of spermatogenesis. **a** Boxplots of the difference from mean gene expression at 8 dpp are shown for each time point, with genes on the autosomes in purple and those on the XY chromosomes in green. Gene expression is log2(TPM + 1). **b** Heatmap of X-linked gene expression at each time point. Genes are clustered based on the pattern of expression: an increase of expression at 12 dpp and then stable throughout (Stable), steadily decreasing over time (Decreasing), or low expression from 8-10 dpp and high expression from 12-14 dpp followed by low expression at 16-18 dpp (Transient). Gene expression is shown as average log2(TPM + 1) over time-point replicates

of spermatogenesis [31]. For example, early pachynema gene lists are enriched for GO terms associated with spermiogenesis (5 out of 33 GO terms for process, all $p < 7.39 \times 10^{-4}$), and the majority of late meiotic prophase- or late-pachynema/diplonema-associated genes were associated with spermiogenesis or fertilization-related GO terms (11 out of 16 GO terms for process, all $p < 7.11 \times 10^{-4}$) (Additional file 1: Table S4). Although genes concordant with early leptonema had transcription-related GO terms in 11 out of 32 GO terms for process (all $p < 1.00 \times 10^{-10}$), we found that many genes negatively concordant with leptotene through zygotene substages have GO terms for transcription and related processes (Additional file 1: Table S3), possibly reflecting the cytologically diminished incorporation of RNA precursors during the earliest meiotic prophase substages [32]. Also among the genes lists for these early stages we found extracellular membrane- or molecular transport-related GO terms prominently represented (Additional file 1: Table S4), which may related to the fact that these cells transit through the Sertoli cell junctions that create the blood-testis barrier [33].

Additionally we performed feature enrichment analysis with the hypergeometric test on the substage-specific gene lists. Interestingly, protein-coding genes are enriched in gene lists concordant with the late-leptotene/zygotene stages ($p = 4.52 \times 10^{-18}$) and the early pachytene stage ($p = 1.19 \times 10^{-8}$). Moreover, they are enriched in the set of genes that is negatively-concordant with late-pachytene and diplotene substages ($p = 5.94 \times 10^{-167}$). However, the genes concordant with late-pachytene and diplotene substages are not depleted in protein-coding gene, which comprise the expected majority of this gene set. This suggests that while certain protein-coding genes are abundant in the Late Pach/Dip substage, large numbers of other protein-coding genes are downregulated in this stage, perhaps reflecting cessation of mRNA transcription in

preparation for the meiotic division stage, or, alternatively, post-transcriptional regulation by PIWI-interacting RNAs (piRNAs). Recent studies show that piRNAs play important roles in genome stability by suppressing harmful transposons as well as by regulating mRNAs [34], and future analyses could integrate piRNA expression with these data.

Transcription factor analysis
Because our results point to a large and diverse meiotic germ-cell transcriptome, also noted by others [19], we inferred the underlying regulatory networks accounting for these patterns, using the iRegulon bioinformatic approach to identify transcription factors (TFs) potentially regulating substage-specific genes (Methods). TFs were identified for each substage-specific gene list with high normalized enrichment scores (NES ≥ 4), corresponding to an estimated false discovery rate of less than 0.01 [35]. We then determined which TF genes were unique to, or shared among, the substages. As can be seen in Additional file 1: Table S6 and Additional file 2: Figure S4, mRNA transcripts for some TFs are substage-specific. For example, *Pou5f1* transcript is specific to the preleptotene stage while *Zbtb33* transcript is specific to the pachytene/diplotene substages. Other TF transcripts, similar to meiosis-specific genes in general, are shared across substages but may be specific to early or late meiosis (Additional file 2: Figure S4); *Zfp143* transcript is shared across late meiosis substages while *Tpbl1* transcript is common to the preleptotene (in the "Jazf1 + 3" cluster) and late leptotene/zygotene/early pachytene (in the "Mybl* + 9" cluster) substages. We also found that some TFs, for example MYBl1, also have target genes that are negatively concordant with substages (Additional file 2: Figure S5; Additional file 1: Table S7). We used the MGI bioinformatics Batch Query tool to determine that 160 of the 181 TFs in this analysis were

Ball et al. BMC Genomics (2016) 17:628

Page 9 of 17

previously found to be highly expressed specifically and/or significantly in the testis or male germ cells and 39 are annotated to male-reproduction-related phenotypes (Additional file 1: Table S6).

To gain a deeper insight into the regulatory patterns of meiosis, we selected the highest scoring TF genes for further analysis, based on iRegulon's NES score which corresponds to a low false discovery rate. Of these highest scoring TFs, half of them are annotated to meiosis-related functions: ETV4, E2F1, GATA2, RFX4, and ZFP143. We included four other well-known meiosis TFs: RARG, MYBL1, ETV5, and TBPL1. We compared the mRNA expression pattern of these TF genes with the expression patterns of their target genes in order to identify putative regulatory relationships, an analysis that is based on the assumption that a relevant TF protein appears more or less contemporaneously with its transcript (i.e., no translational delay). In cases where the expression pattern of the TF gene had the opposite expression pattern of its target genes, we infer that the TF acts as a repressor on these targets; but in cases where the expression patterns of the TF gene and its target genes were concordant, we postulate that the TF enhances expression of its targets. For TFs with genes that did not change over our time course, such as the known candidate NRF1, we could not infer a relationship to target genes and excluded them from further analysis.

Following these assumptions, as illustrated in Figs. 4 and 5, we suggest that OVOL2 and YY1 act as repressors of target genes in early leptonema and ETV5, ETV6, and ZFP143 act as repressors on target genes after initiation of meiosis, beginning with the late leptotene and zygotene substages. Evidence suggests that ZBTB33, GATA2, and ETV4 also act as repressors on gene targets in pachynema (Fig. 4 and Additional file 2: Figure S6); while RFX4 appears to be an enhancer of target genes in late pachytene and diplotene substages (Additional file 2: Figure S6), but may repress its target genes in preleptonema, although this relationship is less clear. Interestingly, these underlying assumptions based on relative expression levels suggest that MYBL1, TBPL1, and E2F1 act as both enhancers and repressors of their target genes. MYBL1 and TBPL1 appear to repress target genes in early meiosis while enhancing target genes in late meiosis, while E2F1 has the opposite pattern and may repress target genes in late meiosis while enhancing target genes in early leptonema (Additional file 2: Figure S6). Similar regulatory switching has been shown to result from changes in protein co-factors [36] and post-translational modifications [37]. Moreover, genes for some of the TFs described above are also themselves target genes associated with specific substages. By considering these relationships, we inferred candidate regulatory interactions among TFs; for example, ZFP143 and ETV5 suppress *Mybl1* gene expression, while

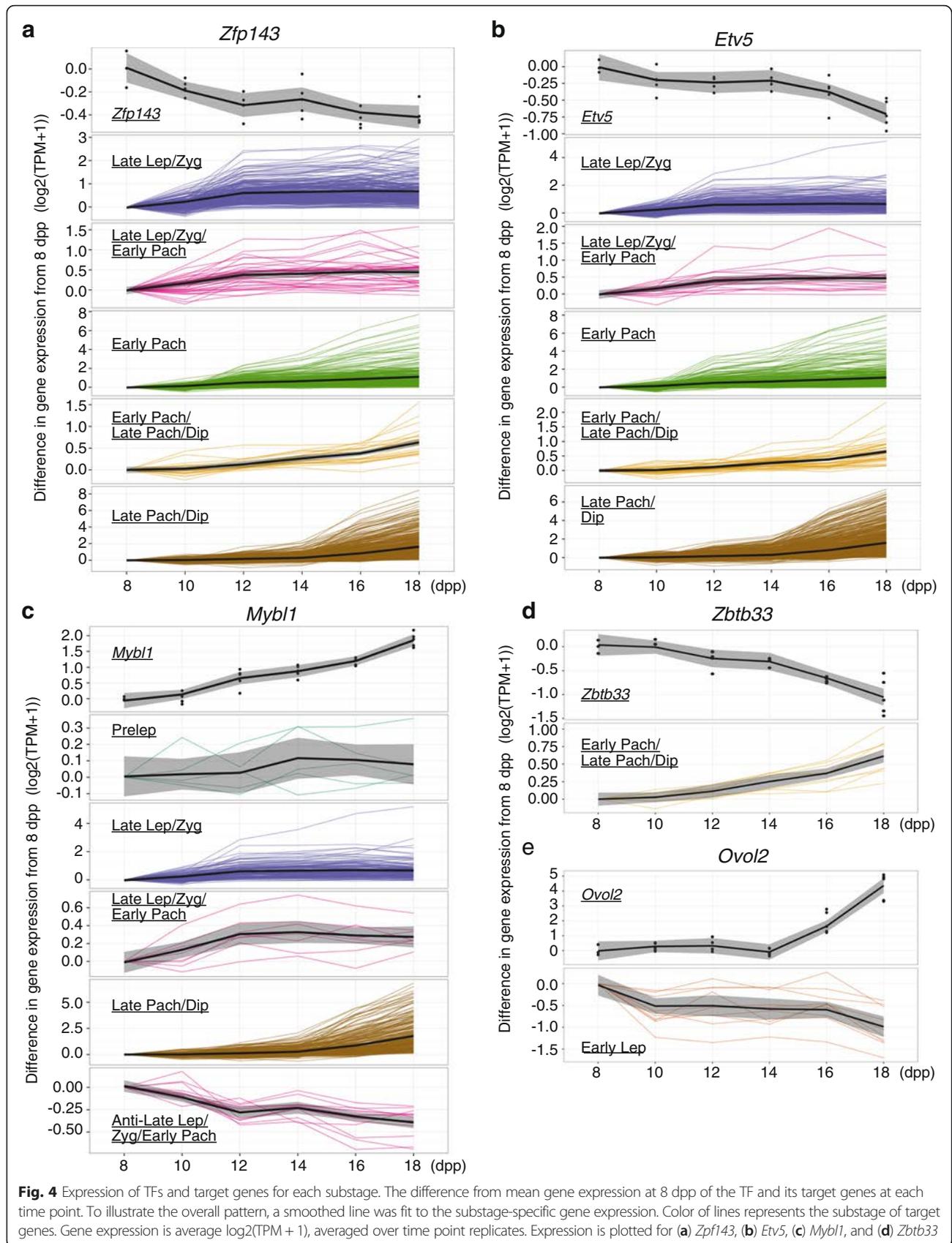MYBL1 enhances expression of *Rfx4*, *Ovol2*, *Yy1*, and *Tbpl1* genes (Fig. 5).

Overall, 41 % of the genes associated with specific meiotic substages (2483 of 6052 genes) are predicted targets of one or more of these eight meiosis-related TFs. This noteworthy observation suggests that this concise regulatory network can account for a substantial portion of the meiotic program of transcription.
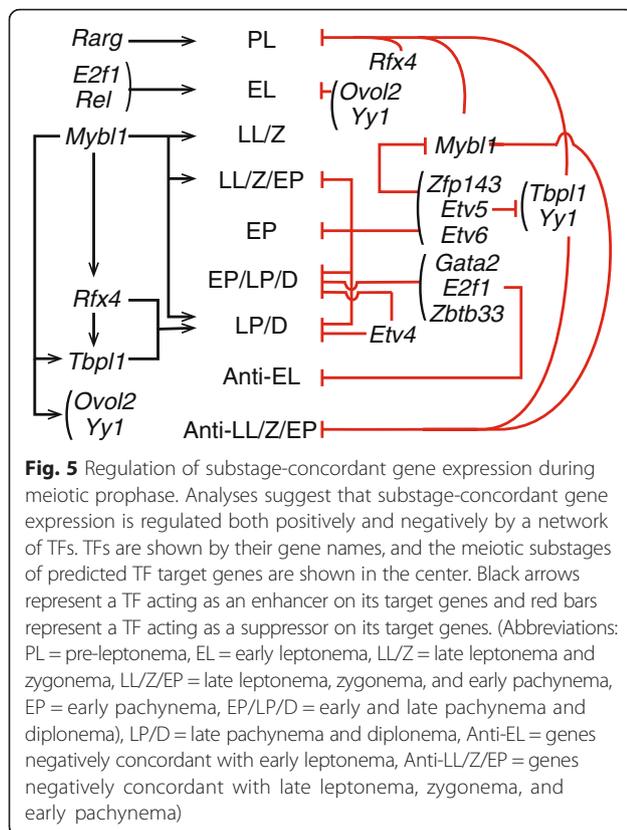
Discussion

Here we identify a male meiotic germ-cell transcriptome using a novel analysis based on a dense dataset of cytological substage-specific signatures. The high concordance between RNA-seq expression data and cytological proportions of isolated germ cells across all samples we analyzed allowed us to develop a novel PMCA to identify the substage-specific transcriptomes for meiotic prophase. This computational method does not require the use of FACS or sedimentation sorting of cells and can be applied to other complex cell populations for which there are well-defined cytological criteria.

Cytological deconvolution of RNA-seq data from the first wave of spermatogenesis

In mammalian males, spermatogenesis is continuous and asynchronous, ensuring daily capacity to deliver sperm backed up by a testis comprised of abundant numbers of germ cells at all stages of spermatogenesis. While advantageous to reproductively active males, this biological imperative has frustrated attempts to isolate stage-purified spermatogenic cells. Methods for stratification of cell samples by either sedimentation [3, 4] or flow cytometry [7, 8] enrich specific spermatogenesis cell stages, while the juvenile first wave of spermatogenesis (used in this study) provides a leading edge of differentiating cells against a background of less differentiated cells. In the laboratory mouse, meiosis is initiated at about 8 dpp in a subset of spermatogonia by retinoic acid stimulation of STRA8 [1, 20]; however, initiation of subsequent waves of meiosis make the cellular population increasingly heterogeneous (Fig. 1c), resulting in a complex histology [4]. The cell-stage frequencies presented here (Fig. 1c) are based on a powerful combinatorial application of antibodies recognizing well-characterized and highly stage-specific marker proteins. We find a continuous and relatively constant background of the earliest spermatogenic cells, namely, spermatogonia and the preleptonema and leptonema (Fig. 1c), and, not surprisingly, these "background" spermatogenic cells are the ones most refractory for computational assignment of a substage-specific transcriptome. On the other hand, pachytene spermatocytes are not present at the earliest juvenile stages, and appear in a discrete time period; consequently, it was possible to assign a robust gene list to this stage.

Ball et al. BMC Genomics (2016) 17:628

Page 10 of 17

Fig. 4 Expression of TFs and target genes for each substage. The difference from mean gene expression at 8 dpp of the TF and its target genes at each time point. To illustrate the overall pattern, a smoothed line was fit to the substage-specific gene expression. Color of lines represents the substage of target genes. Gene expression is average log2(TPM + 1), averaged over time point replicates. Expression is plotted for (a) Zpf143, (b) Etv5, (c) Mybl1, and (d) Zbtb33

Ball *et al. BMC Genomics* (2016) 17:628

Page 11 of 17

Fig. 5 Regulation of substage-concordant gene expression during meiotic prophase. Analyses suggest that substage-concordant gene expression is regulated both positively and negatively by a network of TFs. TFs are shown by their gene names, and the meiotic substages of predicted TF target genes are shown in the center. Black arrows represent a TF acting as an enhancer on its target genes and red bars represent a TF acting as a suppressor on its target genes. (Abbreviations: PL = pre-leptonema, EL = early leptonema, LL/Z = late leptonema and zygonema, LL/Z/EP = late leptonema, zygonema, and early pachynema, EP = early pachynema, EP/LP/D = early and late pachynema and diplonema), LP/D = late pachynema and diplonema, Anti-EL = genes negatively concordant with early leptonema, Anti-LL/Z/EP = genes negatively concordant with late leptonema, zygonema, and early pachynema)

Gene assignments to specific substages were guided by the covariance of transcriptomic data and the cytological data. Assignment of expressed transcripts to cellular subpopulations in heterogeneous samples has long been a computational challenge [18, 38–40]. In this study, we exploited the advantage of paired RNA-seq and cytological data to develop the novel PMCA approach that isolates changes of gene expression specific to each meiotic substage. Maximum covariance analysis (MCA) was first developed in the meteorological sciences [41] and was popularized in the climatological sciences in the 1990s [42, 43]. More recently, an MCA approach has been used in a bioinformatics context to clarify relationships between gene and protein expression [44]. While MCA is often an effective tool for detecting common signals in two sets of variables, it can be limited by a tendency to fit spurious patterns when faced with increased sampling variation [45, 46]. Current methods [47] employ a parametric smoothing model using principal component regression, which requires a normality assumption or rely on GO analysis [44]. We developed a novel PMCA method that not only overcomes the spurious pattern identification liability but that does so without the need for any parametric assumptions or reliance on GO analysis. Our PMCA approach is broadly applicable to multi-dimensional data derived from a common set of samples.

Substage specificity of meiotic gene expression and regulation

Historically, meiotic prophase substages are characterized by the morphology of chromatin, and correlated genetic mechanisms have been revealed in the past decades [48]. It is known that there is widespread transcription of protein-coding genes in the testis [19], and indeed, we found that among germ cells alone, more than 15,000 genes are transcribed, suggesting that a significant portion of testis transcriptional complexity is due to germ cells. Using PMCA, we successfully identified genes with expression patterns that matched the "cyto-patterns" of stage-specific cell frequencies determined by antibody labeling (Fig. 1c). Some genes were shared among substages; for example, late leptotene and zygotene shared 131 genes with early pachytene and early pachytene shared 106 genes with late pachytene and diplotene. Due to the strong temporal signal of contribution of the late pachytene germ cells, which do not appear until 16 dpp and greatly increase in representation by 18 dpp, we identified over 4000 late pachytene genes. However, since the proportion of preleptotene and early leptotene cells did not vary greatly over time, we were unable to deconvolve stage-specific transcriptomes for the earliest meiotic substages as confidently as for the later substages.

We compared these substage-specific gene lists to those developed in other recent analyses of the germ-cell testis transcriptome. The striking increase in number of genes unique to the pachytene stage was also observed by Soumillon, et al. [19], where, in fact, greater numbers of genes were considered expressed than in this study. However, we have used a more stringent cutoff (TPM ≥ 3) to eliminate from the data transcripts expressed at low levels. When we relaxed this requirement and compared the number of genes expressed with a cutoff of TPM > 0, we found the number of expressed transcripts to be similar to that reported by Soumillion, et al. [19]. We also compared the substage-specific gene lists to the relevant clusters identified by Margolin, et al. [18]. In their study, gene lists were temporally clustered from single samples taken at 6, 10, 12, 14, 16, 18, 20, and 38 dpp. While our study was based on multiple replicates at each time point as well as fine-grained cytological analysis, our PMCA gene lists substantially overlapped with their derived gene list clusters (Additional file 1: Table S8). In all, 4013 of the 4077 genes in clusters identified by Margolin, et al. [18] were also expressed in our dataset.

We also compared our results with those derived from flow-cytometry based methods of sorting by DNA content [5, 6]. For both of these studies, we found overall concordance in genes assigned to meiotic substages (Additional file 1: Table S9). These similarities were especially pronounced for late pachytene and diplotene substages due to the large numbers of genes in these

Ball *et al. BMC Genomics* (2016) 17:628

Page 12 of 17

sets. However, we also observed a broader trend of alignment between early and late substages. Furthermore, our use of multiple markers to cytologically characterize cells paired with our PMCA analysis allowed for more precise substage assignment than possible by cell sorting. For instance, our spermatogonia and pre-leptotene sets were the top two strongest overlaps with the "secondary spermatocyte" (2C) cell fraction in da Cruz, et al. [5] (hypergeometric test $p = 4.5 \times 10^{-4}$ and $p = 1 \times 10^{-3}$, respectively), but split these assignments to provide improved substage resolution. Similarly, our joint late-leptotene and zygotene genes and early pachytene genes had the two greatest overlaps with the combined "leptotene and zygotene" and "pachytene spermatocytes" (LZ + PS) genes (hypergeometric test $p = 8.7 \times 10^{-7}$ and $p = 1.4 \times 10^{-3}$, respectively), and further partition these transcripts into more precise substages. Analysis of Fallahi et al. [6] data was limited by different experimental platforms (microarrays versus RNA-seq), different assay timing (adult versus juvenile mice), and generally low numbers of uniquely assigned genes, but also revealed significant overlaps in late substages (Additional file 1: Table S9). By assessing functional concordance by similarity in GO annotations, we determined that our early leptotene and Fallahi et al. [6] preleptotene sets share a common enrichment in RNA transcription genes. Finally, the most prominent divergences between our data and these previous results were in the spermatogonia fraction. We note that cell sorting techniques are susceptible to inclusion of somatic-cells in this fraction, whereas our spermatogonia genes were significantly negatively-concordant with many standard meiosis genes (Additional file 1: Table S3). In sum, these comparisons suggest that our transcript sets encompass and substantially expand these previous findings.

In this study, we characterized each meiotic substage using the list of substage-specific genes from PMCA analysis. Some meiosis genes were associated to particular substages. For example, *Spata22* [49] and *Msh4/5* [50, 51] are both highly associated with late leptotene/zygotene substages, and both are required for recombination. However, many canonical meiosis genes were found throughout all meiotic prophase substages; these genes include *Rad51*, *Rec8*, and *Syce2*. This may well reflect a lack of acute transcriptional regulation for these important transcripts. Rather than transcription at the precise meiotic substage of use, quality and efficiency of meiosis may be ensured by having transcripts present and available for translation throughout meiotic prophase, with substage transitions regulated post-transcriptionally and/or posttranslationally. Further, although we confirmed that spermatogonia negatively concordant genes are enriched with meiotic genes, we found several meiotic genes in the gene list concordant with spermatogonia, including *Fign*, which was reported to be required for meiotic recombination

[52], suggesting that some of the meiotic program is set up prior to meiotic entry.

Not surprisingly, this developmental transcriptome analysis also revealed that many genes expressed during meiosis do not have known functions directly contributing to meiosis. These may instead be part of a parallel program of spermatogenic gene expression. For example, many of the genes expressed in early leptonema are associated with transcription or RNA metabolism, as well as with cellular processes such as cell-cell interactions, which are of considerable importance in the biology of the seminiferous tubule. PMCA also revealed that late pachytene/diplotene-expressed genes are significantly associated with GO terms associated with spermiogenic processes, correlating well with findings of other studies [5, 6]. During post-meiotic stages of nuclear condensation, transcription is globally repressed [28, 53], underlying the biological rationale for prior transcription to support the active protein synthesis during spermiogenesis. In addition, the late pachytene/diplotene-associated gene lists are significantly enriched with non-proteincoding RNAs, including lincRNAs (long intergenic noncoding RNA) and piRNA precursors.

Meiotic regulatory networks

Analysis of predicted TF targets [35] generated a regulatory network that potentially governs the meiotic and spermatogenic programs of gene expression identified by this study (Fig. 5). The protein ZFP143 was central in our network, and is required for embryo development in zebrafish [54] and human [55, 56]. The human ortholog, ZNF143, is ubiquitously expressed [57], and binds to the promoter region of target genes where it is required for formation of chromatin loops by interacting with POLII and RAD21 [58]. Because RAD21 is differentially expressed after the pachytene stage of meiosis [59], it is possible that ZFP143 is crucial for spermatogenic processes by regulating the transcription of genes during pachytene/diplotene substage, an idea that should be tested experimentally since our analysis indicates that ZFP143 may target genes strongly associated with genes in these substages. Reinforcing the validity of our approach, our regulatory network also involved MYBL1 (also known as A-MYB). Our results support previous findings that a subset of late pachynema/diplonema-expressed genes, many involved with the spermatogenic and spermiogenic processes, are associated with MYBL1 [60, 61]. MYBL1 regulates transcription of cell cycle-related genes. Germ cells with a homozygous mutation in the *Mybl1* gene exhibit defects in meiotic chromosome synapsis [60]. Moreover, our results suggest that MYBL1 also is in a network associated with the transcription of genes encoding proteins required for piRNA biogenesis, including *Tdrd1*, *Tdrd6* and *Tdrd7*, consistent with previous reports [62]. Going beyond

Ball et al. BMC Genomics (2016) 17:628

Page 13 of 17

our core regulatory network, we also identified several other TFs, whose target genes include the Tdrd family and Piwi genes, potentially involved in piRNA processing: ATF3, ELF1, ELK3, ELK4, FLI1, NFYA, NFYB, NRF1, PBX3, RFX2, RFX7, SP1, YY1, ZBTB33, ZFP143 and ZFP42. This analysis not only revealed a core network for transcriptional regulation of meiotic progression (Fig. 5 and Additional file 2: Figures S4 and S5) but also suggested that a significant proportion of the genes expressed in the meiotic transcriptome may be controlled by a concise entourage of transcription factors.

Conclusions

This study has untangled in part the complexity and parallel process of spermatogenesis and meiosis by focusing on associating gene expression with highly specific cytological signatures defining meiotic prophase substages. This unique and powerful approach to deconvolving transcriptomes of complex cell populations is applicable for discovery of transcriptional signals in other such complex cell populations or heterogeneous tissues.

Methods

Experimental design and mice

All C57BL/6J mice used for this study were obtained from The Jackson Laboratory (Bar Harbor, USA). All animal procedures were in accordance with the National Institute of Health guide and U.S. Department of Agriculture standards for animal care and use and were approved by the Animal Care and Use Committee at The Jackson Laboratory (Protocol #05004). Mice were euthanized at 8, 10, 12, 14, 16 and 18 days post partum (dpp) to follow the leading edge of meiotic progression during the first wave of spermatogenesis. For each time point, 5 biological replicates were sampled and germ cells were isolated from the pooled two testes of each mouse. A portion of germ cell sample was used for cytological analysis and the rest of cells were used for RNA-seq analysis. Both cytological and RNA-seq analyses were performed on all 30 samples (Fig. 1a).

Cytological methods

Isolation of mixed testicular germ cells

The procedure was as previously described with some modifications [26]. Briefly, seminiferous tubules were transferred into 20 ml DMEM (Gibco, Life Technologies, Carlsbad, CA, USA) containing 0.5 mg of Liberase TL Research Grade (05401020001, Roche, Basel, Switzerland) and incubated for 20 min at 32 °C. To remove interstitial cells, tubules were washed three times with the same media. In the final wash media, the tubules were pipetted several times to form fragments, which were digested with 0.5 mg of Liberase and 10 μg of DNase in 20 ml DMEM for 13 min at 32 °C in shaking water bath. The isolated

cells were further digested by pipetting for 3 min, and germ cells were isolated by filtering through Nitex mesh (53-70 μm pore size). The crude germ cells were washed three times by centrifugation for 7 min at 500 g using 10 ml of the media containing 10 μg of DNase. The cells were resuspended in 1 ml of ice-cold PBS, and cell concentration determined. 1.25×10^5 cells (about 10 % of total) were used for cytological scoring, with the remainder used for RNA-seq (see below).

Isolation of enriched populations of adult pachytene germ cells

Each enriched population (4 biological replicates) of pachytene/diplotene spermatocytes was obtained from the testes of six 9-week-old mice by sedimentation at unit gravity [3]. Mixed germ-cell suspensions were prepared as described above, and after the three 0.5 % BSA/KRB washes, cells were separated by cellular sedimentation at unit gravity in a 2–4 % BSA gradient generated over 2.5 h in a STA-PUT apparatus (ProScience Inc., GlassShop, Toronto, ON, Canada). Following the sedimentation process, 10 ml fractions were collected and examined using light microscopy and differential interference contrast Nomarski optics. Cells were identified based on morphological criteria and size [3]. Fractions containing pachytene/diplotene spermatocytes of average purity ~90 % were pooled. For every cell separation, and for each population of cells collected, an aliquot of cells was snap-frozen for subsequent RNA extraction as described below.

Chromatin spread preparation

Germ-cell suspensions prepared as described above were fixed in 2 % PFA containing 0.03 % SDS and mixed with an equal volume of 0.04 % Photo-Flo (Kodak, Rochester, NY, USA). The cell suspension was applied to wells of 12-well Shandon slides, and incubated in a humid chamber for 1 h at RT. After fixation, the cells were briefly air-dried, and subjected to further fixation: 2 % PFA with SDS for 3 min and 2 % PFA without SDS for 3 min. The slides were then washed three times with 0.04 % Photo-Flo. Air-dried slides were stored at -20 °C for further use.

Immunostaining of spread chromatin

Spread chromatin preparations were incubated with 10 % ADB blocking solution (ADB: PBS containing 2 % BSA and 0.05 % Triton-X 100) for 10 min, the same blocking solution with SDS for 10 min, and the blocking solution without SDS. Immunolabeling was performed with rat polyclonal anti-SYCP3 (1:1000 dilution, Handel lab), mouse monoclonal anti-phosphorylated histone H2AX (1:200 dilution; 05-636, Millipore, Billerica, MA, USA), rabbit polyclonal anti-STRA8 (1:1000 dilution; ab49405, Abcam, Cambridge, England) and guinea pig polyclonal

Ball *et al. BMC Genomics* (2016) 17:628

Page 14 of 17

anti-H1t antibodies (1:500 dilution; Handel lab). Subsequently, secondary antibodies conjugated with Alexa 647, 594 or 488 (Molecular Probes, Invitrogen, Carlsbad, CA, USA) were used at 1:500 dilution. Nuclei were stained with DAPI (0.5 μg/mL) for 10 min, and the slides were mounted with glycerol. Images were observed using a Zeiss AxioImager.Z2 epifluorescence microscope equipped with a Zeiss AxioCam MRm CCD camera (Carl Zeiss, Jena, Germany).

RNA methods
Isolation of RNA and sequencing library preparation
Isolated germ-cell samples were resuspended in QIAzol Lysis Reagent according to the manufacturer's instructions, and total RNAs were purified from homogenized cells using Qiagen RNeasy Mini Kit (74104). The quality of the isolated RNA was assessed using an Agilent 2100 Bioanalyzer instrument (Agilent Technologies, Santa Clara, CA, USA) and RNA 6000 Nano LabChip assay (5067-1511, Agilent Technologies).

The mRNA sequencing libraries were prepared using the Illumina TruSeq methodology. mRNAs were purified from total RNA using biotin tagged poly dT oligonucleotides and streptavidin coated magnetic beads. The mRNAs were then fragmented and double stranded cDNA was generated by random priming. The library was then analyzed for quality using an Agilent 2100 Bioanalyzer instrument (Agilent Technologies) and DNA 1000 LabChip assay.

RNA sequencing
Short 100 bp paired-end reads were generated and sequenced using an Illumina® HiSeq (Illumina, San Diego, CA, USA). Sequenced reads were filtered to keep reads for which 70 % of the base pair quality score was > 20, and the 3′ end was trimmed if the base pair quality score was < 20. Two technical replicates for each paired-end were run in different lanes and then merged.

RNA extraction and quantitative real-time quantitative RT-PCR
For real-time RT-PCR, total RNA was isolated from isolated germ cells or enriched germ cells (see above) using the RNeasy Mini Kit (Qiagen, Hilden, Germany), and 1 μg RNA was reverse transcribed using QuantiTect Reverse Transcription Kit (Qiagen) according to the manufacture's instruction. The real-time RT-PCR was performed by the Applied Biosystems 7500 Real-Time PCR system (Foster City, CA. USA) using the QuntiTect SYBR Green RT-PCR kit (Qiagen). Transcript levels were normalized to the levels of *Actb* by the standard curve method [63], and are presented as the mean normalized expression in 10 μg RNA. Data are represented as mean ± estimated standard deviation. Gene-specific primers are listed in Additional file 1: Table S10.

Computational methods
Alignment and expression
All RNA-seq samples were aligned with Bowtie 1.0.0 [64] and expression levels were estimated by RSEM 1.2.8 [65]. A Bowtie index was prepared for alignment to a combined (mm10) transcriptome of Ensembl Genome Reference Consortium, build 38, release 75 [66], NONCODE v4 lncRNA [25], and piRNA precursor transcripts [17]. The 214 piRNA precursors were obtained from Dr. Christian Roy. Both the NONCODE lncRNA and piRNA precursors were converted to mm10 coordinates using liftOver [67]. For this study, we used log2(TPM + 1) as the expression level, where TPM is transcripts per million, defined by RSEM [65]. A gene was deemed expressed if TPM ≥ 3 for at least one of the 28 samples.

Principal component analysis
To test the concordance of the expression and cytological data, independent Principal Component Analyses (PCA) were performed on each dataset using prcomp(x, scale = TRUE) in the rgl package [68] in R [69]. To produce Fig. 1d, the first and second principal components for both datasets were scaled to have the same range.

Permutation-based Maximum Covariance Analysis (PMCA)
We developed a novel permutation-based maximum covariance analysis (PMCA) that not only overcomes the spurious pattern identification liability of traditional maximum covariance analysis but also does not require any parametric assumptions about the data. Instead, we implemented a permutation procedure that assures the patterns are valid within a given false positive rate (FPR). To begin, let

$$X_{6\times28} \ \& \ Y_{20368\times28} \tag{0.1}$$

be the cytological and gene expression data, respectively. Then mean center each row, where $\tilde{X}, \tilde{Y}$ are mean centered (Eq. 1.2.)

$$\tilde{x}_{is} = x_{is} - \frac{1}{28}\sum_{s=1}^{28} x_{is}, \ \tilde{y}_{ks} = y_{ks} - \frac{1}{28}\sum_{s=1}^{28} y_{ks} \tag{0.2}$$

$$i = 1, 2, ..., 6, \ s = 1, 2, ..., 28, \ k = 1, 2, ..., 20368$$

We compute the covariance matrix and the SVD of the covariance matrix in Eq. 0.3.

$$C_{6\times20368} = \frac{1}{28}\tilde{X}\tilde{Y}^T = U\Sigma V^T \tag{0.3}$$

Because we are interested in mapping the genes of Y onto substages of X we consider $P_{x(6\times28)} = U^T\tilde{X}$, the

Ball *et al. BMC Genomics* (2016) 17:628

Page 15 of 17

principal components of the covariance matrix that correspond to the substages, and calculate the homogeneous and heterogeneous regressions:

$$Z_{x(6\times6)} = XP^T_x, \ Z_{y(20368\times6)} = YP^T_x \quad (0.4)$$

To allow for direct comparison, each row of Z_x, Z_y is divided by its respective root mean square, Eq. 0.5.

$$Z_{x(ij)} = z_{x(ij)} / \sqrt{\sum_{j=1}^{6} z^2_{x(ij)} / 5} \quad (0.5)$$

$$Z_{y(kj)} = z_{y(kj)} / \sqrt{\sum_{j=1}^{6} z^2_{y(kj)} / 5}$$

For each substage cyto-pattern (the row of Z_x corresponding to the substage), we find the genes that have a similar gene expression pattern across the columns of Z_y. Through computation of the SVD, we lose a degree of freedom so the maximum number of patterns is 5; there are 6 substages. For each substage cyto-pattern, we call a gene pattern similar if it is within a certain window of the substage's cyto-pattern.

To determine the optimal window width, we devised a permutation method that iterates through varying window widths and chooses the optimal width based on the estimated false positive rate (FPR). We stipulated that the estimated FPR be less that 0.05 by the third component ($j = 3$). Because the gene lists get finer, and more specific, as we progress through the components, the estimated FPR for cyto-patterns 4 and 5 are less that the specified 0.05. For the substage-specific gene lists described in this paper, the estimated FPR < 0.005. A detailed explanation of the PMCA optimal width selection is provided in Additional file 3.

Bioinformatic analysis
Gene Ontology (GO) analysis
GO enrichment analysis was performed using GOrilla, Gene Ontology enRIchment anaLysis and visuaLizAtion tool [30] with ranked gene lists. Gene lists were ranked for each substage based on a score that measures how closely each gene pattern follows the substage cytopattern. GO terms was established by the GO Consortium [70] and used to group genes according to their biological or molecular functions. A total of 13,363 of the 15,025 genes expressed in our time series have at least one annotation in GO.

Transcription factor analyses
TFs for substage-concordant and negatively concordant genes and the TF target genes were identified using iRegulon, Version 1.3 [35] in Cytoscape, version 3.1.0 [71]

with the substage-concordant and negatively concordant gene lists.

Additional files

Additional file 1: This file contains a mini-website of Tables S1–S10. The same mini-website is available at http://carterdev.jax.org/dtx/a2/index.html. Interactive expression plots. **Table S1.** Number and proportion of isolated cells for cytological analysis and RNA-seq. **Table S2.** Gene lists and gene expression values for each of the substages, separated by worksheets. An additional worksheet provides results for X-linked genes. Abbreviations for each substage are as follows: Sp'gonia for spermatogonia, PL for preleptotene, EL for early leptotene, LL + Z for late leptotene and zygotene, LL + Z + EP for those genes found in late leptotene, zygotene, and early pachytene, EP for early pachytene, EP + LP + D for early pachytene, late pachytene, and diplotene, and LP + D for late pachytene and diplotene. Sheet names prefixed with "Anti-"correspond to genes that are negatively concordant with the substage, (e.g., Anti-PL corresponds to genes that are negatively concordant with preleptotene. Genes are ranked by how closely the expression pattern follows the substage pattern (rank = 1 is best). Gene ids and Gene names for piRNA precursors and NONCODE lncRNAs have prefix "pi-" and "NON", respectively. Expression is given in log2(TPM + 1). **Table S3.** GO analysis for substage-negatively concordant genes. Abbreviations for each substage are as follows: Sp'gonia for spermatogonia, EL for early leptotene, LL-Z for late leptotene and zygotene, EP for early pachytene, and LP-D for late pachytene and diplotene. **Table S4.** GO analysis for substage-concordant genes. Abbreviations for each substage are as follows: Sp'gonia for spermatogonia, EL for early leptotene, LL-Z for late leptotene and zygotene, EP for early pachytene, and LP-D for late pachytene and diplotene. **Table S5.** Analysis of genes annotated to meiosis. **Table S6.** TFs for substage-concordant genes. The column names are explained as follows: "NES" is short for Normalized Enrichment Score in iRegulon, "ngenes" is the number of substage-concordant genes associated with the TF, "name" used in the arc-diagram (* indicates a family of genes, e.g., Rfx* for Rfx1, Rfx2, Rfx3, Rfx4). Bolded TFs are highly expressed in the testis and those highlighted in red are associated with male reproduction. **Table S7.** TFs for substage-negatively concordant genes. The column names are explained as follows: "NES" is short for Normalized Enrichment Score in iRegulon, "ngenes" is the number of substage negatively-concordant genes associated with the TF, "name" used in the arc-diagram (* indicates a family of genes, e.g., Rfx* for Rfx1, Rfx2, Rfx3, Rfx4). **Table S8.** Comparison of substage-concordant gene lists with derived clusters in Margolin, et al. [14]. **Table S9.** Comparison of substage-concordant gene lists with sets derived from FACS-sorted cells [5, 6]. **Table S10.** Primers for qRT-PCR. (ZIP 6513 kb)

Additional file 2: This file contains a mini-website of Figures S1–S6 and a link to interactive expression plots. The same mini-website is available at http://carterdev.jax.org/dtx/a1/index.html. **Figure S1.** Expression of substage-concordant genes. (A–H) Heat maps show gene expression of substage-concordant genes at each time point. Gene expression is shown as average log2(TPM + 1) of time point replicates. **Figure S2.** Expression of substage-negatively concordant genes. (A–H) Heat maps show gene expression of substage-negatively concordant genes at each time point. Gene expression is shown as average log2(TPM + 1) of time point replicates. **Figure S3.** Validation of RNA-seq expression pattern by qRT-PCR. Box plots (top) show gene expression detected by RNA-seq at 10 dpp and 16 dpp. Bar graphs (bottom) show gene expression detected by qRT-PCR using isolated germ cells from pooled testes from 3 mice at 10 dpp and 16 dpp. Gene expression for RNA-seq is shown as log2(TPM + 1). Gene expression for qRT-PCR is shown as fold increase relative to *Actb* expression. **Figure S4.** TF arc diagram illustrating the most significant TFs across substages for the concordant gene lists. Node color represents the substage. Node size is related to significance (larger = more significant but all are highly significant with a iRegulon NES > = 4). Width of arc corresponds to how many TFs are shared between nodes (wider = more shared TFs). A node is connected to another node if a node's TFs are a subset of the other node's TFs. Color of the arc (degree) is related to how many connections the node has. Degree equals the number of connections. The name of each node is an abbreviation, where an asterisk indicates multiple members of the TF family are included in the node (e.g., Rfx* for

Ball *et al. BMC Genomics* (2016) 17:628

Page 16 of 17

Rfx1, Rfx2, Rfx3, Rfx4) and when a node name is followed by + integer, as in "Mef2* + 1", it indicates that there are TFs in the Mef2 family plus one other TF. All TFs associated with each node are listed in Additional file 1: Table S6. The number in parenthesis next to the node name indicates the number of substage-concordant genes associated with the TF cluster. **Figure S5.** TF arc diagram illustrating the most significant TFs across substages for the negatively concordant gene lists. Node color represents the substage. Node size is related to significance (larger = more significant but all are highly significant with a iRegulon NES > = 4). Width of arc corresponds to how many TFs are shared between nodes (wider = more shared TFs). A node is connected to another node if a node's TFs are a subset of the other node's TFs. Color of the arc (degree) is related to how many connections the node has. Degree equals the number of connections. The name of each node is an abbreviation, where an asterisk indicates multiple members of the TF family are included in the node (e.g., Rfx* for Rfx1, Rfx2, Rfx3, Rfx4) and when a node name is followed by + integer, as in "Mef2* + 1", it indicates that there are TFs in the Mef2 family plus one other TF. All TFs associated with each node are listed in Additional file 1: Table S7. The number in parenthesis next to the node name indicatea the number of substage-negatively-concordant genes associated with the TF cluster. **Figure S6.** Expression of TF and its target genes for each substage. The difference of mean gene expression at 8 dpp of the TF and its target genes at each time point. To illustrate the overall pattern, a smoothed line was fit to the substage-specific gene expression. Color of lines represents the substage of target genes. Gene expression is shown as average log2(TPM + 1) across time point replicates. (ZIP 13261 kb)

Additional file 3: Details of permutation-based maximum covariance analysis (PMCA). (PDF 150 kb)

Availability of data and materials

Transcriptome data are available in Gene Expression Omnibus under accession number GSE72833. All other data are available as Additional Files as detailed below.

Authors' contributions

The project was designed by GWC, MAH and MH with YF and RLB; the research was conducted by YF and RLB with contributions from FS, JH and MH. YF, RLB, GWC and MAH analyzed the data and wrote the manuscript. All authors read and approved the final manuscript.

Competing interests

The authors declare that they have no competing interests.

Author details

[1]The Jackson Laboratory, Bar Harbor, ME, USA. [2]Department of Computer Science, Trinity University, San Antonio, TX, USA.

References

1. Hogarth CA, Arnold S, Kent T, Mitchell D, Isoherranen N, Griswold MD. Processive pulses of retinoic acid propel asynchronous and continuous murine sperm production. Biol Reprod. 2015;92(2):37.
2. Romrell LJ, Bellve AR, Fawcett DW. Separation of mouse spermatogenic cells by sedimentation velocity. A morphological characterization. Dev Biol. 1976;49(1):119–31.
3. Bellve AR. Purification, culture, and fractionation of spermatogenic cells. Methods Enzymol. 1993;225:84–113.
4. Bellve AR, Cavicchia JC, Millette CF, O'Brien DA, Bhatnagar YM, Dym M. Spermatogenic cells of the prepuberal mouse. Isolation and morphological characterization. J Cell Biol. 1977;74(1):68–85.
5. da Cruz I, Rodriguez-Casuriaga R, Santinaque FF, Farias J, Curti G, Capoano CA, Folle GA, Benavente R, Sotelo-Silveira JR, Geisinger A. Transcriptome analysis of highly purified mouse spermatogenic cell populations: gene expression signatures switch from meiotic-to postmeiotic-related processes at pachytene stage. BMC Genomics. 2016;17(1):294.
6. Fallahi M, Getun IV, Wu ZK, Bois PRJ. A global expression switch marks pachytene initiation during mouse male meiosis. Genes. 2010;1(3):469–83.
7. Gaysinskaya V, Soh IY, van der Heijden GW, Bortvin A. Optimized flow cytometry isolation of murine spermatocytes. Cytometry A. 2014;85(6):556–65.
8. Getun IV, Torres B, Bois PR. Flow cytometry purification of mouse meiotic cells. J Vis Exp. 2011;(50):2602.
9. Fujiwara Y. Differential gene expression revealed by transcriptomic analyses of male germ cells. J Anim Genet. 2014;42(2):91–9.
10. Chalmel F, Rolland AD, Niederhauser-Wiederkehr C, Chung SS, Demougin P, Gattiker A, Moore J, Patard JJ, Wolgemuth DJ, Jegou B, et al. The conserved transcriptome in human and rodent male gametogenesis. Proc Natl Acad Sci U S A. 2007;104(20):8346–51.
11. Namekawa SH, Park PJ, Zhang LF, Shima JE, McCarrey JR, Griswold MD, Lee JT. Postmeiotic sex chromatin in the male germline of mice. Curr Biol. 2006;16(7):660–7.
12. Shima JE, McLean DJ, McCarrey JR, Griswold MD. The murine testicular transcriptome: characterizing gene expression in the testis during the progression of spermatogenesis. Biol Reprod. 2004;71(1):319–30.
13. Kleene KC. A possible meiotic function of the peculiar patterns of gene expression in mammalian spermatogenic cells. Mech Dev. 2001;106(1-2):3–23.
14. Schultz N, Hamra FK, Garbers DL. A multitude of genes expressed solely in meiotic or postmeiotic spermatogenic cells offers a myriad of contraceptive targets. Proc Natl Acad Sci U S A. 2003;100(21):12201–6.
15. Chalmel F, Lardenois A, Evrard B, Rolland AD, Sallou O, Dumargne MC, Coiffec I, Collin O, Primig M, Jegou B. High-resolution profiling of novel transcribed regions during rat spermatogenesis. Biol Reprod. 2014;91(1):5.
16. Laiho A, Kotaja N, Gyenesei A, Sironen A. Transcriptome profiling of the murine testis during the first wave of spermatogenesis. PLoS One. 2013;8(4): e61558.
17. Li XZ, Roy CK, Dong X, Bolcun-Filas E, Wang J, Han BW, Xu J, Moore MJ, Schimenti JC, Weng Z, et al. An ancient transcription factor initiates the burst of piRNA production during early meiosis in mouse testes. Mol Cell. 2013;50(1):67–81.
18. Margolin G, Khil PP, Kim J, Bellani MA, Camerini-Otero RD. Integrated transcriptome analysis of mouse spermatogenesis. BMC Genomics. 2014;15:39.
19. Soumillon M, Necsulea A, Weier M, Brawand D, Zhang X, Gu H, Barthes P, Kokkinaki M, Nef S, Gnirke A, et al. Cellular source and mechanisms of high transcriptome complexity in the mammalian testis. Cell Rep. 2013; 3(6):2179–90.
20. Anderson EL, Baltus AE, Roepers-Gajadien HL, Hassold TJ, de Rooij DG, van Pelt AM, Page DC. Stra8 and its inducer, retinoic acid, regulate meiotic initiation in both spermatogenesis and oogenesis in mice. Proc Natl Acad Sci U S A. 2008;105(39):14976–80.
21. Yuan L, Liu JG, Zhao J, Brundell E, Daneholt B, Hoog C. The murine SCP3 gene is required for synaptonemal complex assembly, chromosome synapsis, and male fertility. Mol Cell. 2000;5(1):73–83.
22. Inselman A, Eaker S, Handel MA. Temporal expression of cell cycle-related proteins during spermatogenesis: establishing a timeline for onset of the meiotic divisions. Cytogenet Genome Res. 2003;103(3-4):277–84.
23. Rogakou EP, Pilch DR, Orr AH, Ivanova VS, Bonner WM. DNA double-stranded breaks induce histone H2AX phosphorylation on serine 139. J Biol Chem. 1998;273(10):5858–68.
24. Cobb J, Cargile B, Handel MA. Acquisition of competence to condense metaphase I chromosomes during spermatogenesis. Dev Biol. 1999;205(1):49–64.
25. Xie C, Yuan J, Li H, Li M, Zhao G, Bu D, Zhu W, Wu W, Chen R, Zhao Y. NONCODEv4: exploring the world of long non-coding RNA genes. Nucleic Acids Res. 2014;42(Database issue):D98–103.
26. La Salle S, Sun F, Handel MA. Isolation and short-term culture of mouse spermatocytes for analysis of meiosis. Methods Mol Biol. 2009;558:279–97.
27. Handel MA. The XY body: a specialized meiotic chromatin domain. Exp Cell Res. 2004;296(1):57–63.

Ball *et al. BMC Genomics* (2016) 17:628

Page 17 of 17

28. Turner JM. Meiotic sex chromosome inactivation. Development. 2007;
134(10):1823–31.

29. Ashburner M, Ball CA, Blake JA, Botstein D, Butler H, Cherry JM, Davis AP,
Dolinski K, Dwight SS, Eppig JT, et al. Gene ontology: tool for the unification
of biology. The Gene Ontology Consortium. Nat Genet. 2000;25(1):25–9.

30. Eden E, Navon R, Steinfeld I, Lipson D, Yakhini Z. GOrilla: a tool for discovery
and visualization of enriched GO terms in ranked gene lists. BMC
Bioinformatics. 2009;10:48.

31. Iguchi N, Tobias JW, Hecht NB. Expression profiling reveals meiotic male
germ cell mRNAs that are translationally up- and down-regulated. Proc Natl
Acad Sci U S A. 2006;103(20):7712–7.

32. Monesi V. Ribonucleic acid synthesis during mitosis and meiosis in the
mouse testis. J Cell Biol. 1964;22:521–32.

33. Smith BE, Braun RE. Germ cell migration across Sertoli cell tight junctions.
Science. 2012;338(6108):798–802.

34. Watanabe T, Lin H. Posttranscriptional regulation of gene expression by Piwi
proteins and piRNAs. Mol Cell. 2014;56(1):18–27.

35. Janky R, Verfaillie A, Imrichova H, Van de Sande B, Standaert L, Christiaens V,
Hulselmans G, Herten K, Naval Sanchez M, Potier D, et al. iRegulon: from a
gene list to a gene regulatory network using large motif and track
collections. PLoS Comput Biol. 2014;10(7):e1003731.

36. Smith JJ, Ramsey SA, Marelli M, Marzolf B, Hwang D, Saleem RA, Rachubinski
RA, Aitchison JD. Transcriptional responses to fatty acid are coordinated by
combinatorial control. Mol Syst Biol. 2007;3:115.

37. Bruckner S, Kohler T, Braus GH, Heise B, Bolte M, Mosch HU. Differential
regulation of Tec1 by Fus3 and Kss1 confers signaling specificity in yeast
development. Curr Genet. 2004;46(6):331–42.

38. Lahdesmaki H, Shmulevich L, Dunmire V, Yli-Harja O, Zhang W. In silico
microdissection of microarray data from heterogeneous cell populations.
BMC Bioinformatics. 2005;6:54.

39. Lu P, Nakorchevskiy A, Marcotte EM. Expression deconvolution: a
reinterpretation of DNA microarray data reveals dynamic changes in cell
populations. Proc Natl Acad Sci U S A. 2003;100(18):10370–5.

40. Shen-Orr SS, Tibshirani R, Khatri P, Bodian DL, Staedtler F, Perry NM, Hastie T,
Sarwal MM, Davis MM, Butte AJ. Cell type-specific gene expression
differences in complex tissues. Nat Methods. 2010;7(4):287–9.

41. Prohaska J. A technique for analyzing the linear relationships between two
meteorological fields. Mon Weather Rev. 1976;104(11):1345–53.

42. Bretherton CS, Smith C, Wallace JM. An intercomparison of methods for
finding coupled patterns in climate data. J Clim. 1992;5(6):541–60.

43. Wallace JM, Smith C, Bretherton CS. Singular value decomposition of
wintertime sea-surface-temperature and 500 mb height anomalies. J Clim.
1992;5(6):561–76.

44. Tan CS, Salim A, Ploner A, Lehtio J, Chia KS, Pawitan Y. Correlating gene and
protein expression data using Correlated Factor Analysis. BMC
Bioinformatics. 2009;10:272.

45. Cherry S. Singular value decomposition and canonical correlation analysis.
J Clim. 1996;9(9):2003–9.

46. Cherry S. Some comments on singular value decomposition analysis. J Clim.
1997;10(7):1759–61.

47. Salim A, Pawitan Y, Bond K. Modelling association between two irregularly
observed spatiotemporal processes by using maximum covariance analysis.
Appl Statist. 2005;54(3):555–73.

48. Handel MA, Schimenti JC. Genetics of mammalian meiosis: regulation,
dynamics and impact on fertility. Nat Rev Genet. 2010;11(2):124–36.

49. La Salle S, Palmer K, O'Brien M, Schimenti JC, Eppig J, Handel MA. Spata22,
a novel vertebrate-specific gene, is required for meiotic progress in mouse
germ cells. Biol Reprod. 2012;86(2):45.

50. Edelmann W, Cohen PE, Kneitz B, Winand N, Lia M, Heyer J, Kolodner R,
Pollard JW, Kucherlapati R. Mammalian MutS homologue 5 is required for
chromosome pairing in meiosis. Nat Genet. 1999;21(1):123–7.

51. Kneitz B, Cohen PE, Avdievich E, Zhu LY, Kane MF, Hou H, Kolodner RD,
Kucherlapati R, Pollard JW, Edelmann W. MutS homolog 4 localization to
meiotic chromosomes is required for chromosome pairing during meiosis
in male and female mice. Genes Dev. 2000;14(9):1085–97.

52. Yuan J, Chen J. FIGNL1-containing protein complex is required for efficient
homologous recombination repair. Proc Natl Acad Sci U S A. 2013;110(26):
10640–5.

53. Lalancette C, Miller D, Li Y, Krawetz SA. Paternal contributions: new
functional insights for spermatozoal RNA. J Cell Biochem. 2008;104(5):
1570–9.

54. Halbig KM, Lekven AC, Kunkel GR. The transcriptional activator ZNF143 is
essential for normal development in zebrafish. BMC Mol Biol. 2012;13:3.

55. Chen X, Fang F, Liou YC, Ng HH. Zfp143 regulates Nanog through
modulation of Oct4 binding. Stem Cells. 2008;26(11):2759–67.

56. Chia NY, Chan YS, Feng B, Lu X, Orlov YL, Moreau D, Kumar P, Yang L, Jiang J,
Lau MS, et al. A genome-wide RNAi screen reveals determinants of human
embryonic stem cell identity. Nature. 2010;468(7321):316–20.

57. Myslinski E, Krol A, Carbon P. ZNF76 and ZNF143 are two human homologs
of the transcriptional activator Staf. J Biol Chem. 1998;273(34):21998–2006.

58. Bailey SD, Zhang X, Desai K, Aid M, Corradin O, Cowper-Sal Lari R,
Akhtar-Zaidi B, Scacheri PC, Haibe-Kains B, Lupien M. ZNF143 provides
sequence specificity to secure chromatin interactions at gene
promoters. Nat Commun. 2015;2:6186.

59. Ishiguro K, Kim J, Fujiyama-Nakamura S, Kato S, Watanabe Y. A new meiosis-
specific cohesin complex implicated in the cohesin code for homologous
pairing. EMBO Rep. 2011;12(3):267–75.

60. Bolcun-Filas E, Bannister LA, Barash A, Schimenti KJ, Hartford SA, Eppig JJ,
Handel MA, Shen L, Schimenti JC. A-MYB (MYBL1) transcription factor is a
master regulator of male meiosis. Development. 2011;138(15):3319–30.

61. Toscani A, Mettus RV, Coupland R, Simpkins H, Litvin J, Orth J, Hatton KS,
Reddy EP. Arrest of spermatogenesis and defective breast development in
mice lacking A-myb. Nature. 1997;386(6626):713–7.

62. Chuma S, Nakano T. piRNA and spermatogenesis in mice. Philos Trans R Soc
Lond B Biol Sci. 2013;368(1609):20110338.

63. Bustin SA. Absolute quantification of mRNA using real-time reverse
transcription polymerase chain reaction assays. J Mol Endocrinol. 2000;
25(2):169–93.

64. Langmead B, Trapnell C, Pop M, Salzberg SL. Ultrafast and memory-efficient
alignment of short DNA sequences to the human genome. Genome Biol.
2009;10(3):R25.

65. Li B, Dewey CN. RSEM: accurate transcript quantification from RNA-Seq data
with or without a reference genome. BMC Bioinformatics. 2011;12:323.

66. Flicek P, Amode MR, Barrell D, Beal K, Billis K, Brent S, Carvalho-Silva D,
Clapham P, Coates G, Fitzgerald S, et al. Ensembl 2014. Nucleic Acids Res.
2014;42(Database issue):D749–755.

67. Fujita PA, Rhead B, Zweig AS, Hinrichs AS, Karolchik D, Cline MS, Goldman M,
Barber GP, Clawson H, Coelho A, et al. The UCSC Genome Browser database:
update 2011. Nucleic Acids Res. 2011;39(Database issue):D876–882.

68. Adler D, Murdoch D, Nenadic O, Urbanek S, Chen M, Gebhardt A, Bolker B,
Csardi G, Strzelecki A, Senger A. rgl: 3D visualization device system
(OpenGL). 2014.

69. R Core Team. R: A Language and Environment for Statistical Computing. In.
Vienna, Austria: R Foundation for Statistical Computing; 2014.

70. Harris MA, Clark J, Ireland A, Lomax J, Ashburner M, Foulger R, Eilbeck K,
Lewis S, Marshall B, Mungall C, et al. The Gene Ontology (GO) database and
informatics resource. Nucleic Acids Res. 2004;32(Database issue):D258–261.

71. Shannon P, Markiel A, Ozier O, Baliga NS, Wang JT, Ramage D, Amin N,
Schwikowski B, Ideker T. Cytoscape: a software environment for integrated
models of biomolecular interaction networks. Genome Res. 2003;13(11):
2498–504.

DEVELOPMENTAL BIOLOGY

Generation of ovarian follicles from mouse pluripotent stem cells

Takashi Yoshino, Takahiro Suzuki, Go Nagamatsu, Haruka Yabukami, Mika Ikegaya, Mami Kishima, Haruka Kita, Takuya Imamura, Kinichi Nakashima, Ryuichi Nishinakamura, Makoto Tachibana, Miki Inoue, Yuichi Shima, Ken-ichirou Morohashi, Katsuhiko Hayashi*

INTRODUCTION: Germ cells develop in a specific environment in the reproductive organs. Throughout oogenesis, oocytes are encapsulated by somatic cells in follicle structures that provide numerous signals and components essential for key events in oocyte development, such as meiosis and growth. The interaction between the oocyte and the somatic follicular cells is regulated in a stage-dependent manner. Recently, in vitro gametogenesis, reconstitution of germ cell development in culture using pluripotent stem cells, has been developed in mammalian species, including mice and humans. In mice, functional oocytes can be produced from pluripotent stem cell–derived primordial germ cell–like cells (PGCLCs) by reaggregation with embryonic ovarian somatic cells at embryonic day 12.5. Therefore, in vitro gametogenesis is expected to be an innovative means of producing a robust number of oocytes in culture. This should be particularly useful for application to humans and endangered animals. However, the in vitro reconstitution of germ cell development is highly dependent on the somatic cell environment provided by embryonic ovarian tissue, which is difficult to obtain from mammalian species. Here, we provide a model system that reconstitutes the ovarian somatic cell environment using mouse pluripotent stem cells.

RATIONALE: During mouse development, the embryonic ovaries originate from the nascent mesoderm, followed by the intermediate mesoderm and coelomic epithelium at the genital ridge region. For the formation of embryonic ovarian somatic cells from mouse pluripotent stem cells, appropriate signals need to be provided in culture to mimic those embryonic events. Using mouse embryonic stem cells (mESCs) harboring reporter constructs that monitor the expression of key genes for each step, we set out to explore culture conditions for the recreation of the differentiation process. Faithful gene expression and functionality should be conferred in induced embryonic ovarian somatic cells under the appropriate conditions. The functionality of the induced cells should be verified by the ability to support the generation of functional oocytes capable of fertilization and subsequent development.

RESULTS: Based on reporter gene expression, we determined a series of culture conditions that recreate the differentiation process from pluripotent cells to gonadal somatic cells in a stepwise manner. Under these conditions, mESCs differentiated into fetal ovarian somatic cell–like cells (FOSLCs) expressing *Nr5a1*, a representative marker gene of gonadal soma-

tic cells, through the nascent mesoderm, intermediate mesoderm, and coelomic epithelium states. FOSLCs exhibited a transcriptional profile and cellular composition similar to those in embryonic ovarian somatic cells at embryonic day 12.5. When FOSLCs were aggregated with PGCLCs derived from mESCs, the PGCLCs entered meiosis, and subsequent oocyte growth accompanied the development of FOSLC-derived follicles in culture. PGCLC-derived oocytes developing in the FOSLC-derived follicles were capable of fertilization and developed to live offspring. These results demonstrate the reconstitution of functional follicle structures that are fully capable of supporting oocyte production.

CONCLUSION: Our results demonstrate that functional gonadal somatic cells can be induced from mESCs through a faithful differentiation process in culture. The generated material may serve as a useful source to replace embryonic ovarian tissue for in vitro gametogenesis. Furthermore, this system contributes to a better understanding of gonadal somatic cell differentiation and the interactions between oocytes and follicular somatic cells. Because it does not require embryonic gonads, the methodology opens the possibility for application in other mammalian species with fewer ethical and technical concerns. This system will accelerate our understanding of gonadal development and provide an alternative source of gametes for research and reproduction. ∎

READ THE FULL ARTICLE AT
https://doi.org/10.1126/science.abe0237
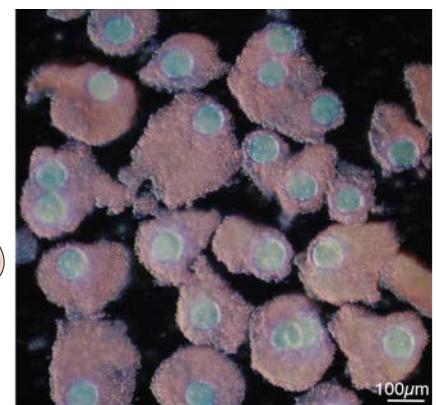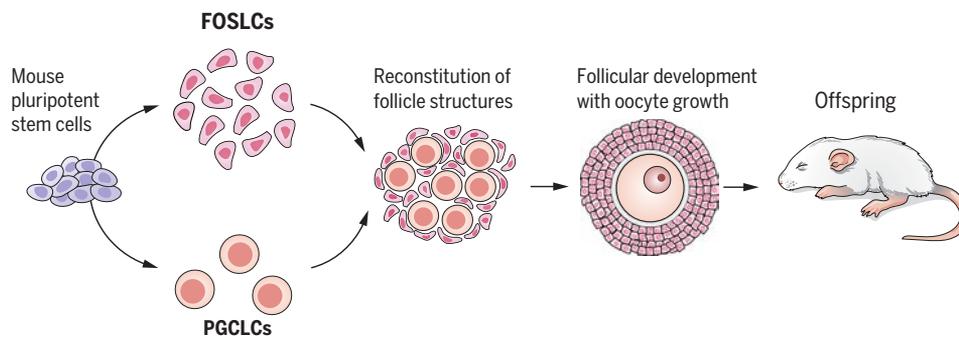
Reconstitution of follicle structures, including oocytes, entirely from mouse pluripotent stem cells. Illustrations on the left show a schematic overview of reconstitution of both FOSLCs and PGCLCs from mESCs. Oocytes in the reconstituted environment gave rise to offspring after fertilization. The right image represents fully grown cumulus-oocyte complexes derived from FOSLCs (red) and PGCLCs (blue).

RESEARCH ARTICLE

DEVELOPMENTAL BIOLOGY

Generation of ovarian follicles from mouse pluripotent stem cells

Takashi Yoshino[1], Takahiro Suzuki[2,3], Go Nagamatsu[1], Haruka Yabukami[2], Mika Ikegaya[2], Mami Kishima[2], Haruka Kita[1], Takuya Imamura[1,4], Kinichi Nakashima[1], Ryuichi Nishinakamura[5], Makoto Tachibana[6], Miki Inoue[7], Yuichi Shima[7,8,9], Ken-ichirou Morohashi[7,8], Katsuhiko Hayashi[1]*

Oocytes mature in a specialized fluid-filled sac, the ovarian follicle, which provides signals needed for meiosis and germ cell growth. Methods have been developed to generate functional oocytes from pluripotent stem cell–derived primordial germ cell–like cells (PGCLCs) when placed in culture with embryonic ovarian somatic cells. In this study, we developed culture conditions to recreate the stepwise differentiation process from pluripotent cells to fetal ovarian somatic cell–like cells (FOSLCs). When FOSLCs were aggregated with PGCLCs derived from mouse embryonic stem cells, the PGCLCs entered meiosis to generate functional oocytes capable of fertilization and development to live offspring. Generating functional mouse oocytes in a reconstituted ovarian environment provides a method for in vitro oocyte production and follicle generation for a better understanding of mammalian reproduction.

In mammalian species, oocytes are grown in the ovarian follicles for a long period of time to acquire competence of fertilization. In mice, the interaction of oocytes with surrounding somatic cells commences at embryonic day (E) 10, when the primordial germ cells (PGCs) migrate into the two genital ridges. Somatic cells in the genital ridge provide signal(s) for the proliferation of PGCs while proliferating themselves to form a pair of gonads. Upon sex determination at around E12, female gonadal somatic cells start to differentiate into granulosa cells and interstitial cells, which eventually form ovarian follicle structures (1). After puberty, primary oocytes begin to grow to mature oocytes, and this process is tightly associated with the development of ovarian follicles that provide the support required for oocyte growth and maturation.

Reconstitution in vitro of the entire process of follicular development would enable a better understanding of oocyte development and robust production of oocytes in culture. Recently, we developed a culture system that produces functional oocytes from mouse pluripotent stem cell–derived PGC-like cells (PGCLCs) by reaggregation with female gonadal somatic cells isolated from E12.5 mouse embryos (2). This system is expected to provide a means of producing a robust number of oocytes in culture and should be particularly useful for application to humans and endangered animals. To enable in vitro generation of mouse follicular development, it is also necessary to develop a culture system that allows the induction of functional female gonadal somatic cells from mouse pluripotent stem cells. By combining in vitro oocyte and somatic gonadal cells, it might then be possible to generate a functional ovarian follicle for fertilization and embryonic growth.

ESCs differentiate into gonadal somatic cells under defined conditions

During mouse development, the pluripotent epiblast undergoes multiple steps to form the embryonic gonads (fig. S1A). During gastrulation, the pluripotent epiblast undergoes epithelial-to-mesenchyme transition along the primitive streak, followed by bilateral ingress underneath the epiblast layer (Fig. 1A). The distance from the primitive streak is important for cell fate determination during mesoderm development; that is, along with the mediolateral axis, the notochord, the paraxial mesoderm (PM), the intermediate mesoderm (IMM; which includes somatic precursors of the gonads), and the lateral plate mesoderm

(LPM) are formed. As a step toward in vitro reconstitution of the somatic gonad, we determined a culture condition that efficiently induces the IMM from mouse embryonic stem cells (ESCs) by focusing on T and *platelet-derived growth factor receptor-α* (*Pdgfra*) expression: T is expressed in the nascent mesoderm at the primitive streak and then eventually restricted in the notochord, whereas *Pdgfra* is expressed in a lateral part of the nascent mesoderm that eventually differentiates into the PM, IMM, or LPM (3, 4) (Fig. 1A). For evaluation of the culture conditions, female ESCs harboring $T^{\text{nEGFP-CreERT2/+}}$ [T–green fluorescent protein (T-GFP)] (5) (fig. S1B) were first differentiated into epiblast-like cells (EpiLCs) (6) and then cultured in a U-bottomed plate with various combinations of BMP4 and a WNT agonist, CHIR99021 (CHIR) (Fig. 1B). T-GFP expression was observed in cell aggregations cultured in the presence of BMP4 or CHIR at 2 days of culture (D2) but disappeared at D4 (fig. S2A). Endogenous T protein was also detected in T-GFP–positive cells (fig. S2B). Fluorescence-activated cell sorting (FACS) analysis showed that in the presence of BMP4 or CHIR, most of the cells expressed both T-GFP and PDGFRA at D2, and then expressed only PDGFRA at D4 (Fig. 1C and fig. S2C), indicating that the nascent mesoderm–like cells were lateralized during the culture period.

Under these conditions, we monitored the expression of *Osr1* and *Foxf1*, which are representative marker genes for IMM and LPM, respectively (7, 8) (Fig. 1D and fig. S1, A and B), by using *Foxf1*-tdTomato/*Osr1*-GFP reporter ESCs (fig. S3A). *Foxf1*-tdTomato was induced by BMP4 in a dose-dependent manner (Fig. 1E and fig. S3, B and C), consistent with evidence that BMP4 lateralizes the mesoderm in vivo (9). *Osr1*-GFP was induced at a high concentration of CHIR with BMP4, but the effect was attenuated by an increased concentration of BMP4 (Fig. 1E and fig. S3, B and C), suggesting a mutually exclusive function of BMP and WNT signaling on the determination of LPM and IMM. Supporting this observation, quantitative polymerase chain reaction (Q-PCR) analysis of the marker gene expression showed that a high concentration of CHIR promoted the expression of the IMM genes but prevented that of the LPM genes (fig. S3D). Under these conditions, the expression of the PM markers *Uncx4* and *Tbx2* remained at a very low level. Based on the enrichment of the *Osr1*-positive/*Foxf1*–negative cell population and transcripts of the IMM marker genes, we fixed the concentrations of BMP4 and CHIR at 1 ng/ml and 14 μM, respectively, for the subsequent culture experiments.
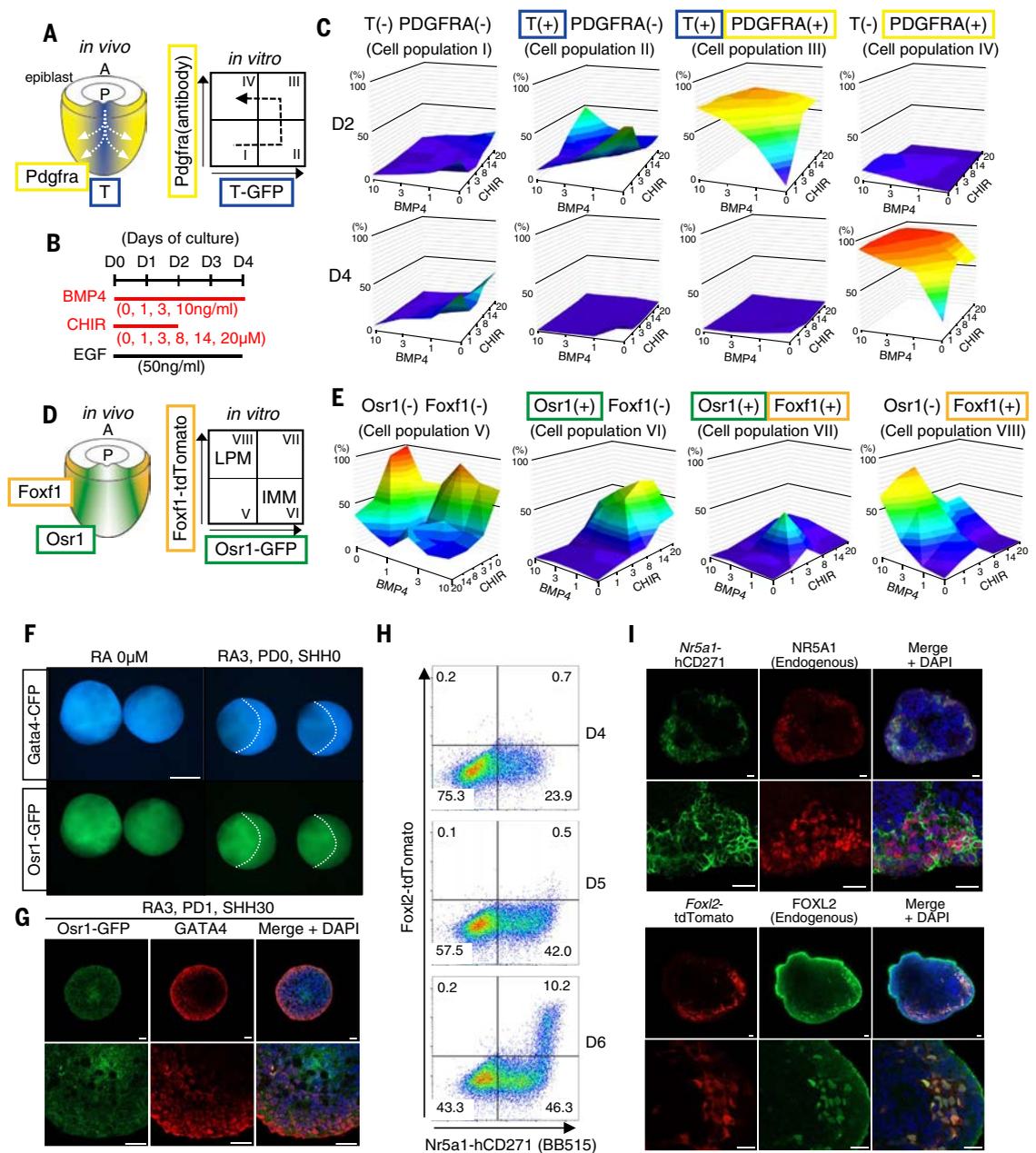
It is known that the mesoderm after gastrulation is anteriorized by retinoic acid (RA) and in contrast posteriorized by fibroblast growth factor (FGF) and Wnt signaling (10–12). In

[1]Department of Stem Cell Biology and Medicine, Graduate School of Medical Sciences, Kyushu University, Higashi-ku, Fukuoka 812-8582, Japan. [2]Laboratory for Cellular Function Conversion Technology, RIKEN Center for Integrative Medical Sciences, Yokohama, Kanagawa 230-0045, Japan. [3]Functional Genomics, Graduate School of Medical Life Science, Yokohama City University, Yokohama, Kanagawa, 230-0045, Japan. [4]RNA Biology and Epigenomics Team/ LMCP, Program of Biomedical Science, Graduate School of Integrated Sciences for Life, Hiroshima University, Higashi-Hiroshima City, Hiroshima 739-8511, Japan. [5]Department of Kidney Development, Institute of Molecular Embryology and Genetics, Kumamoto University, Chuo-ku, Kumamoto 860-0811, Japan. [6]Laboratory of Epigenome Dynamics, Graduate School of Frontier Biosciences, Osaka University, Suita, Osaka 565-0871, Japan. [7]Department of Molecular Biology, Graduate School of Medical Sciences, Kyushu University, Higashi-ku, Fukuoka City 812-8582, Japan. [8]Department of Systems Life Sciences, Graduate School of Systems Life Sciences, Kyushu University, Higashi-ku, Fukuoka City 812-8582, Japan. [9]Department of Anatomy, Kawasaki Medical School, Kurashiki City, 701-0192 Okayama Prefecture, Japan.
*Corresponding author. Email: hayashik@hgs.med.kyushu-u.ac.jp

Fig. 1. Sequential differentiation to the gonadal somatic cell precursor. (**A**) Marker genes for monitoring nascent mesoderm differentiation. The left diagram shows embryonic regions expressing *T* (blue) and *Pdgfra* (yellow) in the mesoderm. White arrows indicate the direction of the spreading mesoderm. The right diagram shows an expected sequence of nascent mesodermal differentiation in the FACS analysis. A, anterior; P, posterior. (**B**) Culture conditions tested for nascent mesoderm differentiation. D0 corresponds to EpiLCs. (**C**) Summary of FACS analysis of *T*-GFP and PDGFRA. Graphs show the percentage of each cell population differentiated under various concentrations of BMP4 and CHIR at D2 and D4. The Roman numerals in the parentheses correspond to the cell population shown in (A). The mean percentage in biologically triplicate experiments is shown. (**D**) Marker genes for monitoring intermediate mesoderm differentiation. The diagrams show embryonic regions expressing *Osr1* (green) and *Foxf1* (orange) (left) and an expected FACS pattern representing IMM and LPM (right). (**E**) Summary of the FACS analysis of *Osr1*-GFP and *Foxf1*-tdTomato. Graphs show the percentage of each cell population differentiated under the conditions shown in (B). The mean percentage in biologically triplicate experiments is shown. (**F**) Distinct distribution of the *Gata4*-CFP–positive cell population. The images show cell aggregations at 4 days in the culture with or without 3 μM RA (RA3). Note that the cultures with RA show mutually exclusive distribution between *Gata4*-CFP–positive and *Osr1*-GFP–positive cells, the border lines of which are indicated by white lines. Scale bars, 200 μm. (**G**) Expression of *Osr1*-GFP and endogenous GATA4 protein. Shown are the results of immunostaining of *Osr1*-GFP and GATA4 protein and merged images with 4′,6-diamidino-2-phenylindole (DAPI; blue) in a section of the *Osr1*-GFP ESC aggregate at 4 days in culture with RA3, 1 μM PD (PD1), and 30 ng/ml SHH (SHH30). Scale bars, 20 μm. (**H**) Differentiation of *Nr5a1*-hCD271–positive cells. Shown are the FACS profiles of Nr271F2T ESCs cultured for the number of days indicated. The numbers in the plot represent the percentages of each cell population. (**I**) Expression of NR5A1 and FOXL2 in the aggregates. Shown are immunofluorescence images of the reporter and endogenous protein indicated and merged images with DAPI (blue) in a section of the Nr271F2T ESC aggregate cultured at D6. Scale bars, 20 μm.

addition, Sonic hedgehog (SHH) is involved in specification of the ventromedial coelomic epithelium in chick embryos (*13*). Therefore, for induction of the anterior ventral IMM, which should contain the precursors of the genital ridge, we tested the effect of RA, the FGF inhibitor PD0325901 (PD), and SHH by adding each of these reagents at D2 (fig. S4A). To monitor differentiation into the precursors of the genital ridge, we inserted the *enhanced cyan fluorescent protein* (*ECFP*) gene into the locus of *Gata4*, the earliest functional marker gene for the genital ridge formation (*14*), in female *Osr1*-GFP ESCs, thereby producing *Osr1*-GFP/*Gata4*-CFP ESCs (fig. S4B). The addition of RA slightly up-regulated *Gata4*-CFP and down-regulated *Osr1*-GFP, whereas PD or SHH had no obvious impact on their

expression (fig. S4C). Q-PCR reinforced the slight up-regulation of *Gata4*, *Lhx9*, and *Wt1*, functional marker genes for gonadal somatic cell precursors (*14–16*), in response to RA (fig. S4D). Mutually exclusive distributions of *Gata4*-CFP–positive cells and *Osr1*-GFP–positive cells were observed in the presence of RA (Fig. 1F and fig. S4E). This pattern was confirmed with endogenous GATA4 protein in the *Osr1*-GFP ESC aggregates (Fig. 1G). This exclusive pattern is consistent with that in gonadal somatic cell precursors in vivo (fig. S4F). Despite the subtle effects or lack of effect of PD and SHH on *Gata4*, *Lhx9*, or *Wt1* expression, the addition of these factors resulted in an increased number of *Gata4*-CFP–positive/*Osr1*-GFP–low cells (fig. S4G). Based on these marker gene expressions and on the number of *Gata4*-CFP–positive/*Osr1*-GFP–low cells produced, we fixed the concentrations of RA, PD, and SHH at 3 μM, 1 μM and 30 ng/ml, respectively, for the subsequent culture experiments.

Nr5a1 is expressed in all cell lineages in the genital ridge (*1*, *17*), and its expression is coordinated by various transcription factors that are essential for gonadal development, such as GATA4 (*14*), EMX2 (*18*), WT1 (*15*, *16*), and LHX9 (*15*), therefore indicating that *Nr5a1* is the most stringent marker for differentiation into gonadal somatic cells. To monitor *Nr5a1* expression, we derived female ESCs from *Nr5a1*-hCD271 bacterial artificial chromosome transgenic mice (*19*) (fig. S1B), in which human *CD271* gene is driven by the *Nr5a1* promoter. Using *Nr5a1*-hCD271 ESCs, we inserted the *tdTomato* gene into the *Foxl2* locus, a marker gene for granulosa cells (*20*), thereby producing *Nr5a1*-hCD271/*Foxl2*-tdTomato (Nr271F2T) ESCs (fig. S5A). When Nr271F2T ESCs were cultured under the conditions described above, *Nr5a1*-hCD271 was detectable in a group of cells at D4 (Fig. 1H). As the culture progressed in the medium containing BMP4 (20 ng/ml) and a low dose of FGF9 (2 ng/ml), the percentage of *Nr5a1*-hCD271–positive cells increased. From D6 onward, *Foxl2*-tdTomato–positive cells appeared (Fig. 1H and fig. S5B). Immunofluorescence analysis confirmed endogenous NR5A1 and FOXL2 expression in the cells expressing the reporter genes (Fig. 1I). In mouse development, the expression of *Foxl2* has been shown to be detectable in the female gonad from E12.5 (*21*, *22*). Given that EpiLCs correspond to E5.75 epiblasts (*6*), the fact that a total of 6 days after EpiLC differentiation was required for the differentiation of *Foxl2*-tdTomato–positive cells was largely consistent with the time course of development in vivo.

ESC derivatives share similar properties with gonadal somatic cells in vivo

To analyze the cell populations induced, we applied single-cell RNA-sequencing analysis of *Nr5a1*-hCD271–positive cells sorted by magnetic-activated cell sorting (MACS) (fig. S6A). Comparison of the expression profiles of *Nr5a1*-hCD271–positive cells at D6 with those of cells in the gonads from E10.5 to E14.5 embryos revealed a similar pattern of cell clusters between E11.5 and E14.5 (Fig. 2A). The numbers of clusters 0, 1, 2, 4, and 5 were comparable both in vitro and in vivo, whereas other clusters were fewer in vitro. Based on the expression of marker genes defined by a previous transcriptome study (*1*), it appears that clusters 0, 1, 2, 4, and 5 include granulosa cell, stromal cell, or early progenitor cell populations, and clusters 3, 6, 7, and 8, which are few in vitro, correspond to germ cell, endothelial cell, erythrocyte, and megakaryocyte populations, respectively (Fig. 2B and fig. S6B). The differentiation of germ cell–like cells was confirmed by evidence that cells expressing *Blimp1*-mVenus (BV), *stella*-CFP (SC), and POU5F1 were sparsely induced under these conditions (fig. S6C). These germ cell–like cells, as well as endothelial cells, erythrocytes, and megakaryocytes, could be induced by BMP4 and WNT signals that promote the differentiation of PGCs and *Flk1*-positive common progenitors of hematopoietic and endothelial cells from ESCs (*6*, *23*). Because *Nr5a1* expression was undetectable in clusters 3, 6, 7, and 8 (fig. S6D), these minor populations might have been the result of insufficient removal by MACS.

To analyze the gonadal somatic cells that directly contribute to the follicle structure, we compared single-cell profiles between *Nr5a1*-hCD271–positive cells at D6 and E12.5 gonadal somatic cells (fig. S6E) because FOXL2 expression was first detectable at those stages in vitro and in vivo, respectively (Fig. 1H) (*22*). After excluding the germ cell, endothelial cell, and hematopoietic cell populations (fig. S6F), the remaining populations could be reclassified into six clusters, S0 to S5 (Fig. 2C). Cells expressing the granulosa cell marker genes were enriched in clusters S2 and S4, and cells expressing the stromal cell marker genes were enriched mainly in cluster S3 and partially in cluster S0 (fig. S6G). The expressions of some stromal cell marker genes, such as *Wnt5a* and *Tcf21*, were detectable in cells belonging to clusters S1 and S5. In clusters S1 and S5, the expressions of early progenitor marker genes (*1*) such as *Sox11*, *Ecm1*, and *Nr2f1* were detectable, indicating that these clusters contain early progenitors. The close similarity in gene expression between the cluster S0/S3 expressing stromal markers and the cluster S1/S5 expressing early progenitor markers was consistent with the fact that early progenitors and stromal cell progenitors share a similar gene expression profile (*1*). *Nr5a1* was widely expressed and enriched in clusters S2 and S4 (fig. S6G), consistent with the evidence that *Foxl2*-tdTomato–positive cells appeared from

the *Nr5a1*-hCD271–highly positive cell population (Fig. 1H). Conversely, *Nr5a1* was not detectable in some cells. The heterogeneous level of endogenous NR5A1 protein expression (Fig. 1I) indicates that the expression of *Nr5a1* was highly heterogeneous at the transcript and protein levels. Because of the substantial contribution of the cell cycle state to the gene expression profile (*24*, *25*), we estimated the cell cycle stage in each cell population. This analysis suggested that cluster S5 was actively proliferative and portions of clusters S0 and S3 were also proliferative (Fig. 2D). By contrast, most cells in clusters S2 and S4 were in G_1, consistent with previous findings that cells expressing *Foxl2* arrested their cell cycle through p27 and CDKN1B (*22*, *26*). Genes involved in epithelial cell function and ovarian epithelial cancer, such as *Krt19*, *Upk3b*, and *Itm2a*, were expressed in clusters S1 and S5 (fig. S6H), suggesting that these clusters could include the surface epithelium of the fetal ovary, known to be the source of granulosa cells (*26*). Based on these observations, we designated clusters S2 and S4 as granulosa cells; clusters S0 and S3 as stromal cell progenitors and stromal cells, respectively; and clusters S1 and S5 as early progenitors (Fig. 2C). The percentage of granulosa cells was smaller in the cell population differentiated in vitro than that in vivo (Fig. 2E). This may have been caused by a delay in granulosa cell differentiation in culture (see below). Comparison of the gene expression in each cluster between the in vivo and in vitro differentiations showed that they were highly similar ($R > 0.96$) (Fig. 2F and fig. S6I). Based on the similar pattern of cell clusters and of gene expression within each cluster, we concluded that the *Nr5a1*-hCD271–positive cell population was similar to the E12.5 gonadal somatic cell population. We thereafter named the *Nr5a1*-hCD271–positive cells fetal ovarian somatic cell–like cells (FOSLCs).

FOSLCs support oocyte development

To evaluate function, FOSLCs were reaggregated with PGCLCs harboring BV and SC reporter genes. Considering that PGCLCs correspond to E9.5 PGCs (*6*), we sorted FOSLCs at D5 by MACS, which yielded 7640 ± 1670 (±SE, $n = 10$ replicates) FOSLCs on average from one aggregation. Because the exact ratio of PGCs to gonadal somatic cells in the nascent genital ridge is difficult to define, following the ratio (5 to 18%) in the E12.5 gonads (*27*), 5000 PGCLCs harboring the BV and SC reporter genes were reaggregated with 75,000 or 100,000 FOSLCs and then cultured under in vitro differentiation culture (IVDi) conditions (*2*). Many oocytes were formed in the reaggregates (Fig. 3A), which were thereafter called reconstituted rOvarioids (rOvarioids) to distinguish them from the ovarioids containing E12.5 gonadal somatic cells. This oocyte formation relied on FOSLCs or gonadal somatic cells because
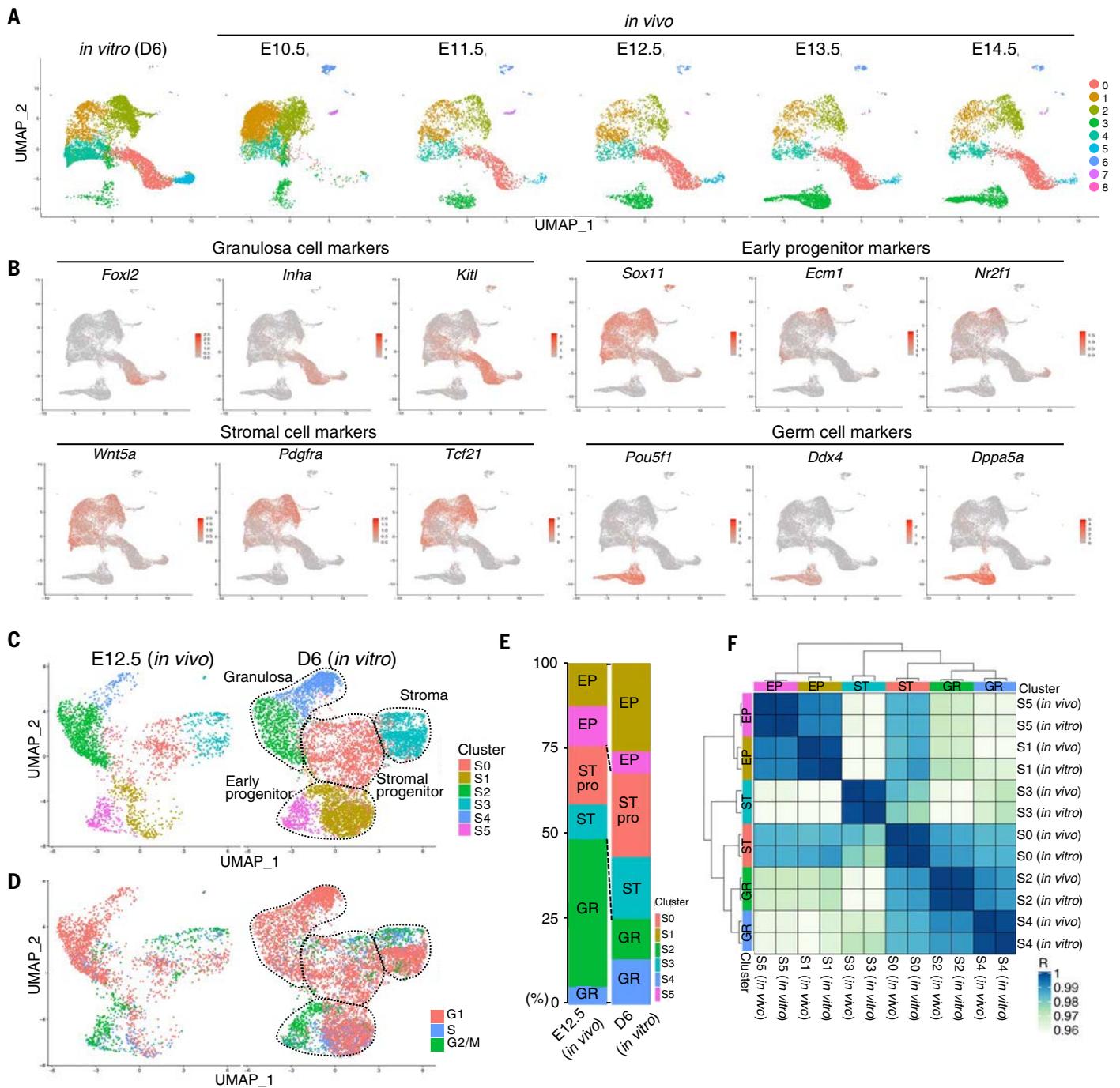
Fig. 2. Comparison of gene expression profiles between gonadal somatic cells in vivo and in vitro. (**A**) Two-dimensional uniform manifold approximation and projection (UMAP) plot of single cells. Shown are the results of UMAP analysis of MACS-sorted Nr5a1-hCD271–positive cells at D6 and female gonadal somatic cells at the embryonic day indicated. The E10.5 sample includes the dorsal mesenchymal tissues around the gonad. Cells are clustered by a graph-based clustering. (**B**) Expression of marker genes for granulosa cells, stromal cells, early progenitors, and germ cells. Cell positions are compiled from the UMAP plots in (A). (**C**) Comparison of follicular cell precursors in vitro and in vivo.

Shown are the results of UMAP analysis of somatic cells contributing to the follicle structure among E12.5 female gonadal somatic cells and MACS-sorted Nr5a1-hCD271–positive cells. Cells are clustered by a graph-based clustering. Dotted lines designate the cell type in each cluster. (**D**) Cell cycle phase analysis of single cells. The cell cycle phase was calculated using canonical cell cycle markers (35). (**E**) Proportion of each cell type in E12.5 female gonads and Nr5a1-hCD271–positive cells. The percentage of each cell type was calculated by the UMAP plot in (C). (**F**) Correlation matrix heat map for all clusters in vivo and in vitro. The clusters were ordered based on the hierarchical clustering.

PGCLCs alone in culture were degraded by D14 (fig. S7A). PGCLCs in the reaggregates expressed SC and BV at D2, down-regulated these genes at D7, and regained only SC expression after D14. This sequence of reporter gene expression in rOvarioids was indistinguishable from that in the ovarioids containing E12.5 gonadal somatic cells (Fig. 3A). The number of oocytes in rOvarioids with 75,000 FOSLCs was reduced to 56.9%, on average, of the number in ovarioids with 75,000 gonadal somatic cells derived from E12.5 ICR embryos, whereas
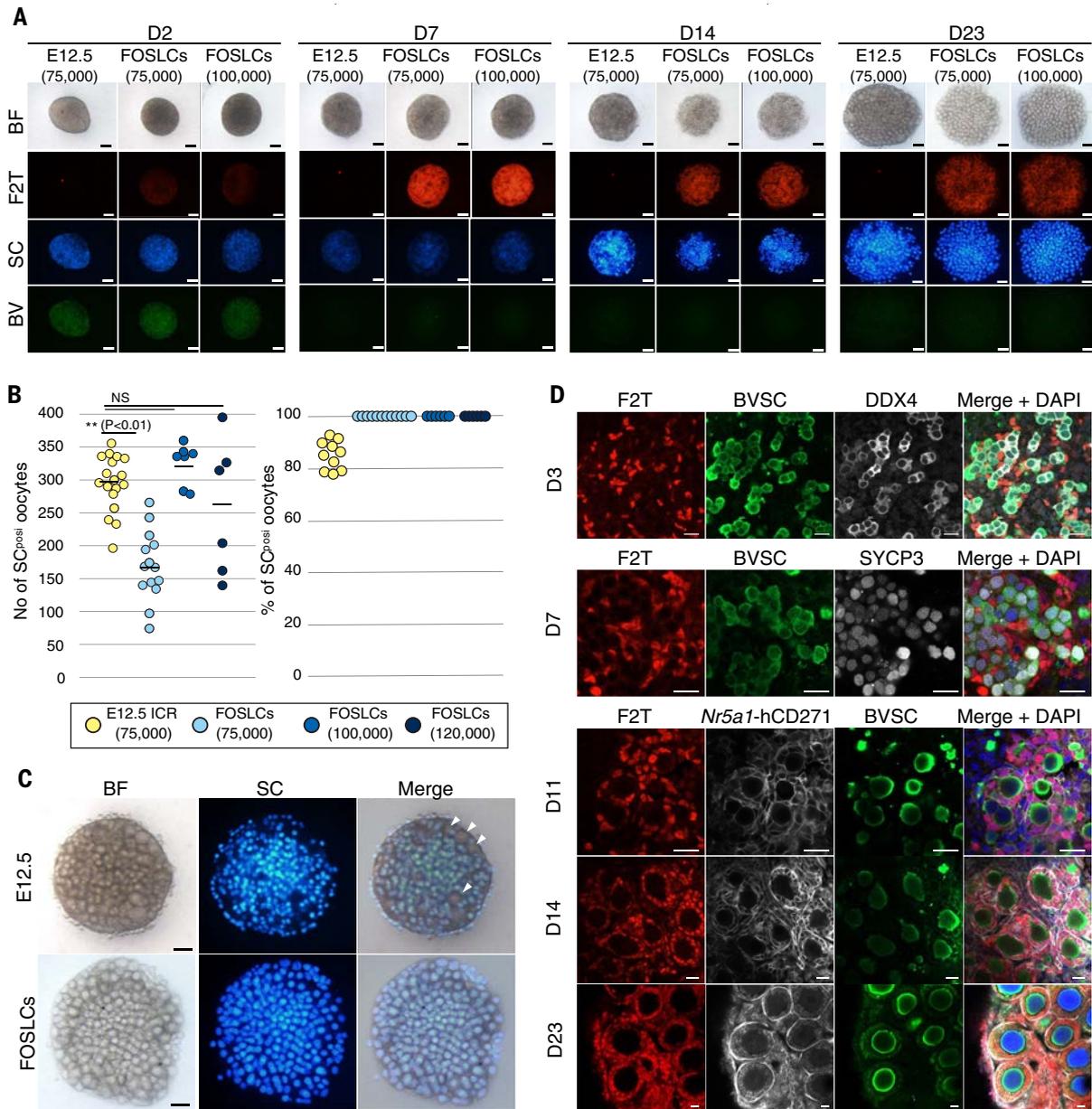
Fig. 3. Oogenesis in the culture system using FOSLCs. (**A**) IVDi culture using FOSLCs. Images show PGCLCs reaggregated with E12.5 gonadal somatic cells or FOSLCs cultured for the number of days indicated. The numbers in parentheses are the numbers of E12.5 gonadal somatic cells or FOSLCs cells used. BF, bright field. Scale bars, 200 μm. (**B**) Summary of oocytes yielded in IVDi culture. Shown are the number of oocytes (left) and the percentage of SC-positive oocytes (right) in the ovarioid or the rOvarioid at day 23 of culture. The numbers of oocytes were determined by counting SC-positive cells in the image. The values were obtained from at least three biologically independent experiments. The bars in the graph indicate the mean value. *P* values relative to the control were determined using Student's *t* test. (**C**) Complete elimination of endogenous oocytes in an rOvarioid. BF and fluorescence images show an ovarioid using 75,000 E12.5 gonadal somatic cells and an rOvarioid using 100,000 FOSLCs. SC-negative oocytes were observed in the ovarioid (arrowheads). Scale bars, 200 μm. (**D**) Immunofluorescence analysis of oocyte development in the rOvarioid. Shown are immunofluorescence images of the antigens indicated and merged images with DAPI (blue). Scale bars, 20 μm.

it became comparable in rOvarioids with 100,000 FOSLCs (Fig. 3B). The productivity was not improved in rOvarioids with 120,000 FOSLCs. This inferior potential of FOSLCs to become embryonic gonadal somatic cells was largely reproducible under the same genetic background; the number of oocytes in rOvarioids with FOSLCs derived from C57BL/6J ESCs was reduced to 67.4% of that in ovarioids with E12.5 C57BL/6J gonadal somatic cells (fig. S7, B and C). All oocytes in the rOvarioids were SC positive, in contrast to ovarioids, which contained SC-negative oocytes derived from residual PGCs mingled in the E12.5 gonadal somatic cells despite depletion by antibodies specific for PGCs (Fig. 3, B and C). This result demonstrated that the rOvarioid completely eliminated contamination of residual oocytes, which is important to ensure the origin of oocytes. In addition, the uniform SC expression also rules out the possibility that cells expressing germ cell markers found in the FOSLCs contribute to oocytes in the rOvarioid.

We next verified the differentiation process in rOvarioids using immunofluorescence analyses. At D3, *Foxl2*-tdTomato–positive cells started to surround PGCLCs that appeared to

proliferate to form germ cell cysts with expression of DDX4, a later germ cell marker (Fig. 3D and fig. S8, A and B). At D7, PGCLCs entered meiosis, thereby differentiating oocytes, with typical alignments of the SYCP3 protein. Individual follicle structures with *Foxl2*-tdTomato–positive cells were formed by D11. At this stage, oocytes degrading in the rOvarioids were frequently observed (fig. S8C), consistent with our previous report that oocyte loss accompanied with apoptosis was observed in ovarioids at D11 (*28*). As the culture progressed, *Foxl2*-tdTomato–positive granulosa-like cells became stratified and *Nr5a1*-hCD271 expression was more prominent in the cells surrounding the follicle structure than in *Foxl2*-tdTomato–positive granulosa-like cells (Fig. 3D and fig. S8B). This is consistent with evidence in vivo that NR5A1 becomes prominent in theca and stromal cells but is downregulated in granulosa cells during follicle development (*29*, *30*). At D23, the formation of secondary follicle structures composed of SC-positive oocytes with a multilayer of *Foxl2*-tdTomato–positive granulosa-like cells and the far surrounding *Nr5a1*-hCD271–positive theca-like cells was observed.

To investigate changes in the competence of FOSLCs during differentiation, PGCLCs were reaggregated with FOSLCs at day 4, 5, 6, 7, or 8 of culture. FACS analysis during the differentiation period showed an increase in the percentage of *Foxl2*-tdTomato–positive cells after D6 (fig. S9A). The analysis also showed that the *Nr5a1*-hCD271–positive/PDGFRA–negative cells, which was the major population at D5, differentiated into either *Nr5a1*-hCD271–highly positive/PDGFRA-negative cells or *Nr5a1*-hCD271–positive/PDGFRA-positive cells, which, based on the marker gene expression (fig. S6G), are granulosa and stromal cells, respectively. When aggregated with PGCLCs, FOSLCs at D5 and D6 showed a high potential for supporting oogenesis (fig. S9B), suggesting that FOSLCs interact with PGCLCs in a timely fashion. Based on marker gene expression, FOSLCs at D6 can be divided into three subpopulations: *Foxl2*-tdTomato–positive (F2T⁺) cells, *Foxl2*-tdTomato–negative and PDGFRA-positive (F2T-P⁺) cells, and *Foxl2*-tdTomato–negative and PDGFRA-negative (F2T-P⁻) cells (fig. S10A). Genes for granulosa cells were enriched, as expected, in the F2T⁺ cell population (fig. S10B). Although the F2T-P⁺ and F2T-P⁻ cell populations could not be clearly distinguished, genes for stromal–stromal progenitor cells were slightly enriched in the F2T-P⁺ cell population. When aggregated with PGCLCs, F2T-P⁺ and F2T-P⁻ cells restored *Foxl2*-tdTomato expression by D7 and formed a number of follicle structures, whereas the F2T⁺ cell population formed a significantly smaller number of follicle structures (fig. S10, C and D). These results indicate that the F2T-P⁺ and F2T-P⁻ populations contain cells that still have

the plasticity to differentiate into granulosa cells and the capability to form follicle structures. This plasticity is consistent with the observation that the granulosa cell population continuously increased after D6 (fig. S9A). Given that the percentage of granulosa cells was smaller in the cell population differentiated in vitro at D6 than in that in vivo (Fig. 2E), the differentiation of granulosa cells may be delayed in the culture system because of an unknown condition that was not fully recapitulated in culture.

Oocytes acquire developmental competence in the culture system using FOSLCs

Developmental competence of FOSLCs was further validated by in vitro growth culture (IVG), in which secondary follicles grow up to a stage equivalent to pre-ovulatory follicles (*2*). In the IVG culture, FOSLC-derived granulosa cells proliferated and formed cumulus-oocyte complexes (COCs) by D12 with the formation of transzonal projections (TZPs), which are essential for juxtacrine interaction to support oocyte growth (*31*) (Fig. 4, A and B). Under in vitro maturation culture (IVM) conditions (*2*), FOSLC-derived cumulus cells were expanded, as is typically observed in maturation of cumulus cells (Fig. 4C). These cumulus cells were readily dispersed by treatment with hyaluronidase, and 28.4% (33/116) of the isolated oocytes proceeded to the MII stage with extrusion of the first polar body (Fig. 4D and table S1). This developmental rate to the MII stage in rOvarioids was comparable to that derived from reaggregates using E12.5 gonadal somatic cells in our previous report (*2*) (28.9%, 923/3198; $P = 0.994$ by Pearson's chi-square test).

We then used mature COCs from rOvarioids for in vitro fertilization (IVF) using wild-type sperm from ICR mice. In IVF followed by in vitro culture, oocytes were fertilized, and 30.2% (301/996) of oocytes used in the IVF became two-cell embryos (Fig. 4D and table S2). Then, 25.8% (24/93) of the two-cell embryos developed to blastocysts (Fig. 4D and table S3). This developmental rate from two-cell embryos to blastocysts was comparable to that observed in embryos derived from reaggregates using E12.5 gonadal somatic cells in our previous report (*2*) (31.8%, 44/138; $P = 0.397$ by Pearson's chi-square test). When the two-cell embryos were transferred into pseudopregnant females, 5.2% (11/212) of the embryos gave rise to offspring and all of them developed to adult mice (Fig. 4, E and F, and table S4). This developmental rate to offspring was comparable to that derived from reaggregates using E12.5 gonadal somatic cells in our previous report (*2*) (3.5%, 11/316; $P = 0.459$ by Pearson's chi-square test). All offspring had dark eyes and some of them had the *BV* or *SC* reporter gene (Fig. 4, F and G), consistent with the fact that the ESCs used were derived from the F₁ blastocyst (129X1/Svj × C57Bl/6J) and

were heterozygous for the reporter genes. Two independent pairs of these mice produced 10 and 14 pups by their intercrosses (Fig. 4H), and 17 out of 21 pups tested had the *BV* and/or *SC* reporter genes (Fig. 4I), demonstrating their fertility in both males and females. These results demonstrated that mouse oocytes produced in the ovarian environment entirely reconstituted by pluripotent stem cells acquired the competence for fertilization followed by development to term.

Applicability of FOSLCs

In our system, purification of FOSLCs is greatly dependent on the *Nr5a1*-reporter construct. This requirement may compromise the applicability of this system because of the time-consuming and laborious processes needed for the production of the reporter cell line. Therefore, we tried to provide an rOvarioid system without the need for a reporter gene. The main reason for requiring a reporter system was the appearance of massively proliferative cells, which severely disturbed oogenesis, in reaggregations without purification of FOSLCs (fig. S11A). Because such proliferative cells were observed in the aggregates containing undifferentiated cells (*32*, *33*), they were likely to lie in the *Nr5a1*-hCD271–negative cell population. Indeed, the proliferative cells almost exclusively appeared in aggregates with *Nr5a1*-hCD271–negative cells (fig. S11B). Therefore, we tried to remove the source of the proliferative cells by using antibodies against endogenous SSEA1 and CD31 because pluripotent stem cells express SSEA1 and CD31 (*34*), and these markers were indeed expressed in a small subset of *Nr5a1*-hCD271–negative cells (fig. S11C). rOvarioids with the cell fraction in the flow-through after the depletion with SSEA1 and CD31 antibodies yielded a number of follicle structures without a proliferative cell clump (fig. S11, D and E). These results demonstrate that the depletion method eliminates the origin of proliferative cells, and therefore a reporter construct is dispensable for the rOvarioid system, which would help to expand the applicability of this system to production of oocytes from pluripotent stem cells without embryonic tissues.

Outlook

Here, we have established a culture system that reconstitutes functional ovarian follicles, including oocytes, from pluripotent stem cells. This system provides several insights for enhancing our understanding and reconstitution of oogenesis. First, this culture system would be an efficient tool for understanding the molecular mechanisms underlying the differentiation of gonadal somatic cells. Second, it enables us to address the interaction between PGCs and/or oocytes and gonadal somatic cells. Because this system can separately

Fig. 4. Full-term development of embryos derived from rOvarioids. (**A**) IVG culture using FOSLCs. Shown are BF and fluorescence images of reconstituted follicles cultured for the number of days indicated after isolation of individual follicles. Abbreviations are as shown in Fig. 3A. Scale bars, 100 μm. (**B**) Formation of TZPs. Shown are fluorescence images of a COC stained with phalloidin and the antibodies indicated. TZPs were formed between the granulosa cells and the oocyte (arrowheads). Scale bars, 10 μm. (**C**) IVM culture using FOSLCs. Shown are BF and fluorescence images of COCs before or after IVM. Note that cumulus cells after IVM were expanded. Scale bars, 100 μm. (**D**) MII oocytes and preimplantation embryos derived from rOvarioids. Scale bars, 100 μm. (**E**) Newborn pups derived from rOvarioids. Shown are pups with placentae obtained by transferring two-cell embryos. (**F**) Adult mice from the newborn pups 4 weeks after birth. (**G**) Detection of reporter genes in the mice derived from rOvarioids. Shown are gel electrophoresis of PCR products to detect BV or SC in the genome. (**H**) Fertility of the adult mice obtained. Shown are pups derived from the intercrossing of the adult mice derived from rOvarioids. (**I**) Detection of reporter genes in the pups derived from two pairs of the adult mice. Shown are the results of gel electrophoresis of PCR products to detect BV or SC in the genome.
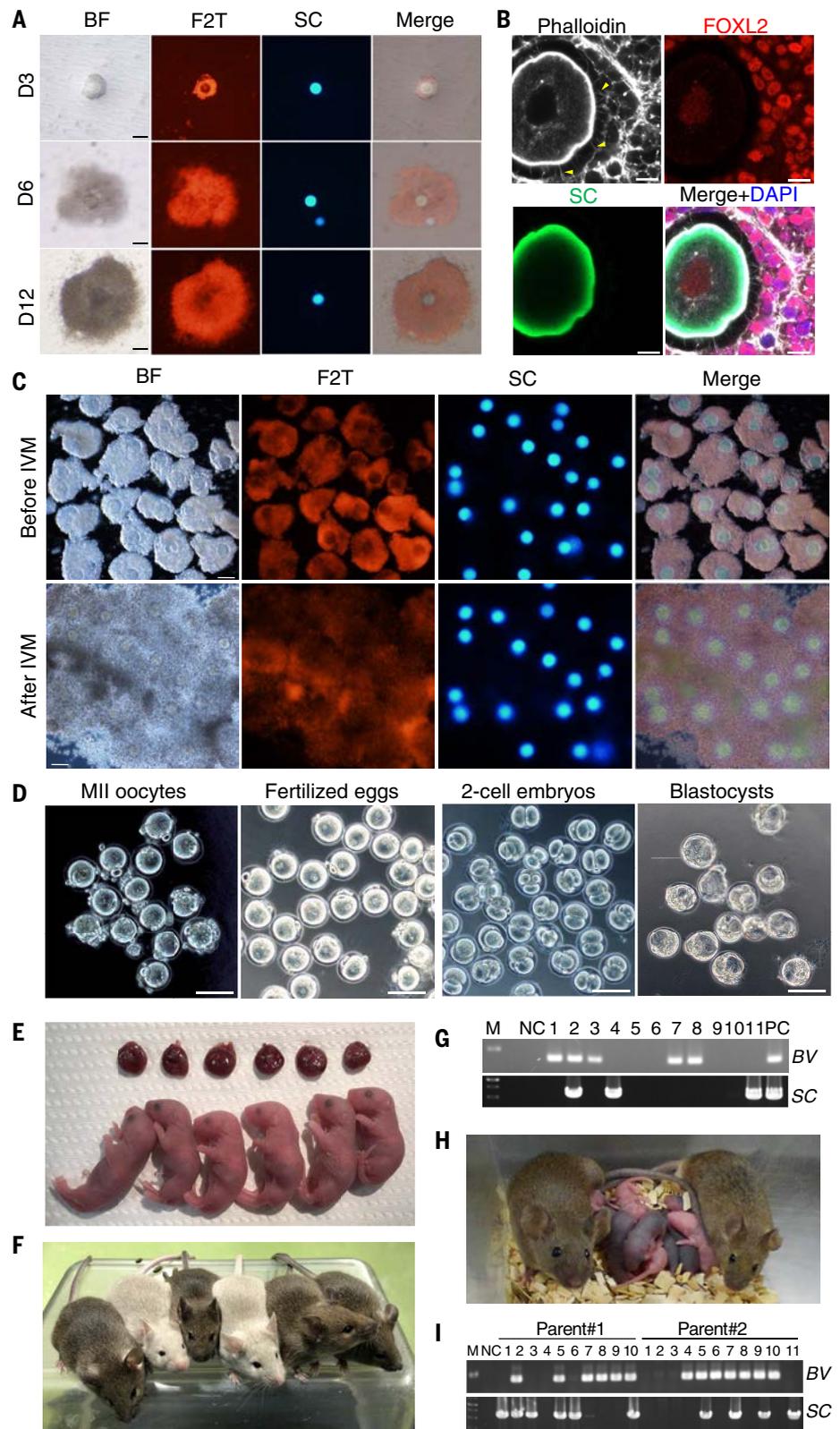
produce FOSLCs and PGCLCs, which are equivalent to nascent gonadal somatic cells and premigratory PGCs (*6*), respectively, it becomes possible to investigate the first and subsequent interactions between these cell types. Last, this culture system opens the possibility of applying in vitro gametogenesis to other mammalian species. The scarcity of embryonic gonadal somatic cells is an obstacle to the application of in vitro gametogenesis to mammalian species other than mice. FOSLCs could be an optimal substitute for embryonic tissue because

they have full potency to support oogenesis. For these reasons, this system will be a useful tool for solving key issues in reproductive biology and regenerative medicine.

Methods summary

For FOSLC induction, *Nr5A1*-hCD271 reporter ESCs were differentiated into EpiLCs with activin A and basic FGF. The EpiLCs were cultured in a low-cell-binding, U-bottomed, 96-well plate with 14 μM CHIR99021, 1 ng/ml BMP4, and 50 ng/ml epidermal growth factor (EGF) for 2 days; then with 3 μM RA, 30 ng/ml Shh, 1 μM PD0325901, 50 ng/ml EGF, and 1 ng/ml BMP4 for another 2 days; and then with 20 ng/ml BMP4 and 2 ng/ml FGF9 for another 1 or 2 days. *Nr5A1*-hCD271–positive FOSLCs were purified by MACS using anti-hCD271 antibody conjugated with microbeads and an MS column. For the production of MII oocytes in rOvarioids, FOSLCs were reaggregated with PGCLCs in a low-cell-binding, U-bottomed, 96-well plate. The rOvarioids were placed on Transwell-COL membranes and then cultured under IVDi conditions for 21 days. Individual follicles were isolated from the rOvarioids and then cultured under IVG conditions for 12 days. Cumulus-oocyte complexes were collected by a fine glass capillary and then cultured under IVM conditions for 16 hours. MII oocytes obtained after IVM culture were subjected to IVF.

REFERENCES AND NOTES

1. I. Stévant et al., Dissecting cell lineage specification and sex fate determination in gonadal somatic cells using single-cell transcriptomics. Cell Rep. 26, 3272–3283.e3 (2019). doi: 10.1016/j.celrep.2019.02.069; pmid: 30893600
2. O. Hikabe et al., Reconstitution in vitro of the entire cycle of the mouse female germ line. Nature 539, 299–303 (2016). doi: 10.1038/nature20104; pmid: 27750280
3. D. G. Wilkinson, S. Bhatt, B. G. Herrmann, Expression pattern of the mouse T gene and its role in mesoderm formation. Nature 343, 657–659 (1990). doi: 10.1038/343657a0; pmid: 1689462
4. H. Kataoka et al., Expressions of PDGF receptor alpha, c-Kit and Flk1 genes clustering in mouse chromosome 5 define distinct subsets of nascent mesodermal cells. Dev. Growth Differ. 39, 729–740 (1997). doi: 10.1046/j.1440-169X.1997.t01-5-00009.x; pmid: 9493833
5. Y. Imuta, H. Kiyonari, C. W. Jang, R. R. Behringer, H. Sasaki, Generation of knock-in mice that express nuclear enhanced green fluorescent protein and tamoxifen-inducible Cre recombinase in the notochord from Foxa2 and T loci. Genesis 51, 210–218 (2013). doi: 10.1002/dvg.22376; pmid: 23359409
6. K. Hayashi, H. Ohta, K. Kurimoto, S. Aramaki, M. Saitou, Reconstitution of the mouse germ cell specification pathway in culture by pluripotent stem cells. Cell 146, 519–532 (2011). doi: 10.1016/j.cell.2011.06.052; pmid: 21820164
7. M. Mahlapuu, M. Ormestad, S. Enerbäck, P. Carlsson, The forkhead transcription factor Foxf1 is required for differentiation of extra-embryonic and lateral plate mesoderm. Development 128, 155–166 (2001). doi: 10.1242/dev.128.2.155; pmid: 11124112
8. J. W. Mugford, P. Sipilä, J. A. McMahon, A. P. McMahon, Osr1 expression demarcates a multi-potent population of intermediate mesoderm that undergoes progressive restriction to an Osr1-dependent nephron progenitor compartment within the mammalian kidney. Dev. Biol. 324, 88–98 (2008). doi: 10.1016/j.ydbio.2008.09.010; pmid: 18835385
9. A. Rojas et al., Gata4 expression in lateral mesoderm is downstream of BMP4 and is activated directly by Forkhead and GATA transcription factors through a distal enhancer element. Development 132, 3405–3417 (2005). doi: 10.1242/dev.01913; pmid: 15987774
10. S. Takada et al., Wnt-3a regulates somite and tailbud formation in the mouse embryo. Genes Dev. 8, 174–189 (1994). doi: 10.1101/gad.8.2.174; pmid: 8299937
11. T. P. Yamaguchi, K. Harpal, M. Henkemeyer, J. Rossant, fgfr-1 is required for embryonic growth and mesodermal patterning during mouse gastrulation. Genes Dev. 8, 3032–3044 (1994). doi: 10.1101/gad.8.24.3032; pmid: 8001822
12. A. Iulianella, B. Beckett, M. Petkovich, D. Lohnes, A molecular basis for retinoic acid-induced axial truncation. Dev. Biol. 205, 33–48 (1999). doi: 10.1006/dbio.1998.9110; pmid: 9882496
13. T. Yoshino, H. Murai, D. Saito, Hedgehog-BMP signalling establishes dorsoventral patterning in lateral plate mesoderm to trigger gonadogenesis in chicken embryos. Nat. Commun. 7, 12561 (2016). doi: 10.1038/ncomms12561; pmid: 27558761
14. Y. C. Hu, L. M. Okumura, D. C. Page, Gata4 is required for formation of the genital ridge in mice. PLOS Genet. 9, e1003629 (2013). doi: 10.1371/journal.pgen.1003629; pmid: 23874227
15. D. Wilhelm, C. Englert, The Wilms tumor suppressor WT1 regulates early gonad development by activation of Sf1. Genes Dev. 16, 1839–1851 (2002). doi: 10.1101/gad.220102; pmid: 12130543
16. M. Chen et al., Wt1 directs the lineage specification of sertoli and granulosa cells by repressing Sf1 expression. Development 144, 44–53 (2017). pmid: 27888191
17. X. Luo, Y. Ikeda, K. L. Parker, A cell-specific nuclear receptor is essential for adrenal and gonadal development and sexual differentiation. Cell 77, 481–490 (1994). doi: 10.1016/0092-8674(94)90211-9; pmid: 8187173
18. M. Kusaka et al., Abnormal epithelial cell polarity and ectopic epidermal growth factor receptor (EGFR) expression induced in Emx2 KO embryonic gonads. Endocrinology 151, 5893–5904 (2010). doi: 10.1210/en.2010-0915; pmid: 20962046
19. S. Kuroki et al., Epigenetic regulation of mouse sex determination by the histone demethylase Jmjd1a. Science 341, 1106–1109 (2013). doi: 10.1126/science.1239864; pmid: 24009392
20. D. Schmidt et al., The murine winged-helix transcription factor Foxl2 is required for granulosa cell differentiation and ovary maintenance. Development 131, 933–942 (2004). doi: 10.1242/dev.00969; pmid: 14736745
21. A. Auguste et al., Loss of R-spondin1 and Foxl2 amplifies female-to-male sex reversal in XX mice. Sex Dev. 5, 304–317 (2011). doi: 10.1159/000334517; pmid: 22116255
22. S. E. Gustin et al., WNT/β-catenin and p27/FOXL2 differentially regulate supporting cell proliferation in the developing ovary. Dev. Biol. 412, 250–260 (2016). doi: 10.1016/j.ydbio.2016.02.024; pmid: 26939755
23. M. C. Nostro, X. Cheng, G. M. Keller, P. Gadue, Wnt, activin, and BMP signaling regulate distinct stages in the developmental pathway from embryonic stem cells to blood. Cell Stem Cell 2, 60–71 (2008). doi: 10.1016/j.stem.2007.10.011; pmid: 18371422
24. Y. Sasagawa et al., Quartz-Seq: A highly reproducible and sensitive single-cell RNA sequencing method, reveals non-genetic gene-expression heterogeneity. Genome Biol. 14, R31 (2013). doi: 10.1186/gb-2013-14-4-r31; pmid: 23594475
25. F. Buettner et al., Computational analysis of cell-to-cell heterogeneity in single-cell RNA-sequencing data reveals hidden subpopulations of cells. Nat. Biotechnol. 33, 155–160 (2015). doi: 10.1038/nbt.3102; pmid: 25599176
26. L. Mork et al., Temporal differences in granulosa cell specification in the ovary reflect distinct follicle fates in mice. Biol. Reprod. 86, 37 (2012). doi: 10.1095/biolreprod.111.095208; pmid: 21976597
27. Y. Morita-Fujimura, Y. Tokitake, Y. Matsui, Heterogeneity of mouse primordial germ cells reflecting the distinct status of their differentiation, proliferation and apoptosis can be classified by the expression of cell surface proteins integrin α6
and c-Kit. Dev. Growth Differ. 51, 567–583 (2009). doi: 10.1111/j.1440-169X.2009.01119.x; pmid: 21314674
28. N. Hamada et al., Germ cell-intrinsic effects of sex chromosomes on early oocyte differentiation in mice. PLOS Genet. 16, e1008676 (2020). doi: 10.1371/journal.pgen.1008676; pmid: 32214314
29. K. Takasawa et al., FOXL2 transcriptionally represses Sf1 expression by antagonizing WT1 during ovarian development in mice. FASEB J. 28, 2020–2028 (2014). doi: 10.1096/fj.13-246108; pmid: 24451388
30. K. Miyabayashi et al., Heterogeneity of ovarian theca and interstitial gland cells in mice. PLOS ONE 10, e0128352 (2015). doi: 10.1371/journal.pone.0128352; pmid: 26039146
31. R. Li, D. F. Albertini, The road to maturation: Somatic cell interaction and self-organization of the mammalian oocyte. Nat. Rev. Mol. Cell Biol. 14, 141–152 (2013). doi: 10.1038/nrm3531; pmid: 23429793
32. K. Hayashi, O. Hikabe, Y. Obata, Y. Hirao, Reconstitution of mouse oogenesis in a dish from pluripotent stem cells. Nat. Protoc. 12, 1733–1744 (2017). doi: 10.1038/nprot.2017.070; pmid: 28796232
33. N. Hamazaki et al., Reconstitution of the oocyte transcriptional network with transcription factors. Nature 589, 264–269 (2021). doi: 10.1038/s41586-020-3027-9; pmid: 33328630
34. T. Furusawa, K. Ohkoshi, C. Honda, S. Takahashi, T. Tokunaga, Embryonic stem cells expressing both platelet endothelial cell adhesion molecule-1 and stage-specific embryonic antigen-1 differentiate predominantly into epiblast cells in a chimeric embryo. Biol. Reprod. 70, 1452–1457 (2004). doi: 10.1095/biolreprod.103.024190; pmid: 14736812
35. M. S. Kowalczyk et al., Single-cell RNA-seq reveals changes in cell cycle and differentiation programs upon aging of hematopoietic stem cells. Genome Res. 25, 1860–1872 (2015). doi: 10.1101/gr.192237.115; pmid: 26430063
36. Data for: T. Yoshino et al., Generation of ovarian follicles from mouse pluripotent stem cells. Zenodo (2021); https://doi.org/10.5281/zenodo.4775540.

SUPPLEMENTARY MATERIALS

science.sciencemag.org/content/373/6552/eabe0237/suppl/DC1
Materials and Methods
Figs. S1 to S11
Tables S1 to S6
References (37–43)
MDAR Reproducibility Checklist

View/request a protocol for this paper from *Bio-protocol*.

Science

Generation of ovarian follicles from mouse pluripotent stem cells

Takashi YoshinoTakahiro SuzukiGo NagamatsuHaruka YabukamiMika IkegayaMami KishimaHaruka KitaTakuya ImamuraKinichi NakashimaRyuichi NishinakamuraMakoto TachibanaMiki InoueYuichi ShimaKen-ichirou MorohashiKatsuhiko Hayashi

Reconstituting the ovarian follicle

Recent advances have enabled the generation of oocytes from pluripotent stem cells in vitro. However, these cells require a somatic environment to develop fully as reproductive cells. Yoshino *et al.* applied what is known about differentiation processes in vivo to determine a culture condition to differentiate embryonic stem cells into gonadal somatic cell–like cells (see the Perspective by Yang and Ng). When the embryonic stem cell–generated ovarian gonadal tissue was combined with early primordial germ cells or in vitro–derived primordial germ cell–like cells, germ cells developed into viable oocytes within the reconstituted follicles that could be fertilized and result in viable offspring. This system enables an alternative method for mouse gamete production and advances our understanding of mammalian reproduction and development.

Science, abe0237, this issue p. eabe0237; see also abj8347, p. 282

View the article online
https://www.science.org/doi/10.1126/science.abe0237
Permissions
https://www.science.org/help/reprints-and-permissions

Use of think article is subject to the Terms of service

The Dynamic Transcriptional Cell Atlas of Testis Development during Human Puberty

Jingtao Guo,[1,2] Xichen Nie,[1] Maria Giebler,[3] Hana Mlcochova,[3] Yueqi Wang,[4] Edward J. Grow,[1] DonorConnect,[5] Robin Kim,[6] Melissa Tharmalingam,[7,8] Gabriele Matilionyte,[7,8] Cecilia Lindskog,[9] Douglas T. Carrell,[2] Rod T. Mitchell,[7,8] Anne Goriely,[3,10] James M. Hotaling,[2,10] and Bradley R. Cairns[1,10,11,*]

[1]Howard Hughes Medical Institute, Department of Oncological Sciences and Huntsman Cancer Institute, University of Utah School of Medicine, Salt Lake City, UT 84112, USA
[2]The Andrology Laboratory, Department of Surgery (Andrology/Urology), Center for Reconstructive Urology and Men's Health, University of Utah Health Sciences Center, Salt Lake City, UT 84112, USA
[3]Radcliffe Department of Medicine, MRC Weatherall Institute of Molecular Medicine, University of Oxford, Oxford OX39DS, UK
[4]Department of Computer Science, Columbia University, New York, NY 10027, USA
[5]DonorConnect, Murray, UT 84107, USA
[6]Section of Transplantation, Department of Surgery, University of Utah School of Medicine, Salt Lake City, UT 84132, USA
[7]MRC Centre for Reproductive Health, The Queen's Medical Research Institute, The University of Edinburgh, Edinburgh EH16 4TJ, UK
[8]Royal Hospital for Children and Young People, Edinburgh EH91LF, UK
[9]Department of Immunology, Genetics and Pathology, Science for Life Laboratory, Uppsala University, Uppsala 751 85, Sweden
[10]Senior author
[11]Lead Contact
*Correspondence: brad.cairns@hci.utah.edu
https://doi.org/10.1016/j.stem.2019.12.005

SUMMARY

The human testis undergoes dramatic developmental and structural changes during puberty, including proliferation and maturation of somatic niche cells, and the onset of spermatogenesis. To characterize this understudied process, we profiled and analyzed single-cell transcriptomes of ~10,000 testicular cells from four boys spanning puberty and compared them to those of infants and adults. During puberty, undifferentiated spermatogonia sequentially expand and differentiate prior to the initiation of gametogenesis. Notably, we identify a common pre-pubertal progenitor for Leydig and myoid cells and delineate candidate factors controlling pubertal differentiation. Furthermore, pre-pubertal Sertoli cells exhibit two distinct transcriptional states differing in metabolic profiles before converging to an alternative single mature population during puberty. Roles for testosterone in Sertoli cell maturation, antimicrobial peptide secretion, and spermatogonial differentiation are further highlighted through single-cell analysis of testosterone-suppressed transfemale testes. Taken together, our transcriptional atlas of the developing human testis provides multiple insights into developmental changes and key factors accompanying male puberty.

INTRODUCTION

Human male puberty involves major changes in testis physiology, a large increase in testicular volume, and complex hormonal and molecular modulation, to accomplish both somatic cell proliferation/maturation and the initiation of spermatogenesis (Koskenniemi et al., 2017; Sharpe et al., 2003). Puberty is initiated by re-activation of the hypothalamo-pituitary-gonadal axis following a period of relative quiescence during childhood (Plant, 2015). This hormonal control requires hypothalamic gonadotrophin-releasing hormone (GnRH) stimulating the release of gonadotrophins, luteinizing hormone (LH), and follicle stimulating hormone (FSH). LH is responsible for stimulating Leydig cells to produce testosterone (T), while FSH stimulates Sertoli cells to support spermatogenesis (Herbison, 2016; Plant, 2015).

To date, our understanding of puberty derives mostly from physiological approaches in humans and primates complemented by extensive molecular and genetic approaches in rodents, which includes the use of sophisticated lineage-tracing and transgenic technologies. However, fundamental differences exist between human and rodent with respect to hormonal control of puberty and onset of spermatogenesis (Tharmalingam et al., 2018). In mice, type B spermatogonia begin to develop at day 8 (d8) resulting in a synchronous "first wave" of spermatogenesis (Bellvé et al., 1977), during which pro-spermatogonia undergo differentiation and synchronously generate both self-renewing and differentiating spermatogonia (Kluin and de Rooij, 1981; Yoshida et al., 2006). This results in the first round of murine sperm production at around d35 (Vergouwen et al., 1993). Subsequently, self-renewing spermatogonia, residing in the niche, commence differentiation and produce successive and continuous waves of gametogenesis from 2–3 weeks after birth (Kanatsu-Shinohara and Shinohara, 2013). However, humans lack the equivalent of this first wave of spermatogenesis and instead are believed to maintain spermatogonia in an undifferentiated (though largely uncharacterized) state prior to the initiation of puberty (Paniagua and Nistal, 1984).
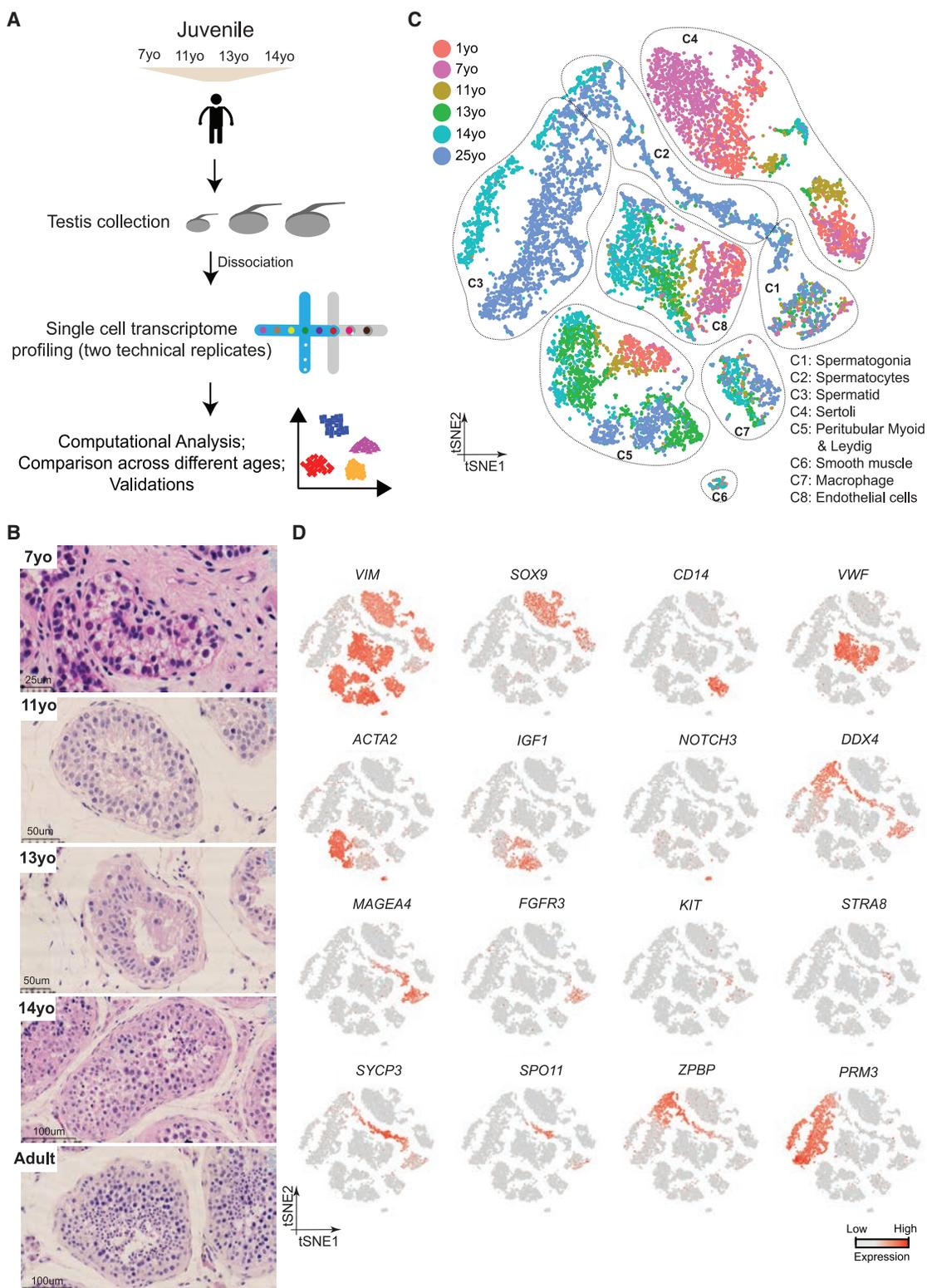
Figure 1. Single-Cell Transcriptome Profiling of the Human Juvenile Testis

(A) Schematic illustration of the experimental workflow.

(B) H&E (hematoxylin and eosin) staining of the different juvenile testes analyzed in this study illustrates the typical macroscopic testicular changes in morphology observed during puberty.

In humans, puberty typically begins between 10 and 13 years after birth. However, low levels of incomplete spermatogenesis is observed in portions of the testis in juveniles prior to puberty, though mature sperm are usually not present prior to age 10–11, and meiotic cells typically undergo apoptosis during peri-pubertal phases (Chemes, 2001) (note: we define "juvenile" as the developmental period after the infant stage but prior to full adult sexual maturity [typically ages from 1–14]). Morphologically, the pre-pubertal testis resembles that of the early postnatal mouse, with undifferentiated spermatogonia embedded in small "cords" of Sertoli cells, that lack a defined tubular lamina or lumen. During puberty, formation of the basal lamina and lumen creates structured seminiferous tubules (Paniagua and Nistal, 1984), which involves the coordinated development of myoid cells (contributing to the formation of the basal lamina), Leydig cells (responsible for hormonal signaling), and Sertoli cells with multiple functions within the tubule—and which together define the main niche components. However, our understanding of this crucial developmental period is limited, and much remains to be characterized at the molecular and genome-wide level, including the mechanisms that maintain human spermatogonial stem cells (SSCs) in a slowly self-renewing and undifferentiated state during childhood and the processes responsible for initiation and progression to spermatogenesis at puberty.

Single-cell RNA sequencing (scRNA-seq) approaches provide unique and powerful tools to examine human testis development, enabling the simultaneous examination of thousands of individual cells, faithfully representing the constituents of entire organs, without the need for prior sorting or enrichment procedures (Birnbaum, 2018; Guo et al., 2018; Hermann et al., 2018; Sohni et al., 2019; Wang et al., 2018). The lack of spatial information obtained from this approach can be alleviated by using orthogonal validation approaches such as co-localization of specific proteins in fixed tissues (Guo et al., 2018). Here, we profiled ~10,000 single-cell transcriptomes from whole-testes of four juvenile males (7, 11, 13, and 14 years old) and compared these data to our previously published infant (1 year old) and adult (25 years old) datasets (Guo et al., 2018). Our study uncovers dramatic changes in germline stem cells and heretofore unappreciated, complex modulations of the somatic niche revealing candidate factors and pathways that regulate somatic cell development during puberty. Certain changes in the niche, such as T production, are accompanied by changes in germ cell states—indicating communication between the germline and niche. To explore the role of T on germline and niche development and function, we analyzed the transcriptome of testes from T-suppressed adult transfemales (that retained spermatogonia), which revealed roles for T in promoting and/or supporting testis development during puberty. Taken together, our datasets and comparative analyses provide multiple insights into the development of SSCs and their niche during puberty in humans, while also providing a valuable data resource

(https://humantestisatlas.shinyapps.io/humantestisatlas1/) for the research community.

RESULTS

Single-Cell Transcriptomes of Human Juvenile Testes

We collected whole-testes through a rapid autopsy program from 4 juvenile donors aged 7, 11, 13, and 14 years (Figure 1A), with Johnsen scores (Johnsen, 1970) at 3, 4, 4, and 7, respectively. Consistent with prior observations (Paniagua and Nistal, 1984), our histological examination revealed major changes in morphology and composition along this timeline (Figure 1B): in the 7-year-old sample, small testis cords lacking an apparent lamina or lumen were observed, forming structures reminiscent of those seen in fetal/early postnatal mouse testes. A tubular structure became progressively apparent in the 11-year-old sample, while a clear defined lamina and lumen were observed across the tubules of the 13- and 14-year-old samples (Figure 1B). To characterize the molecular features accompanying this developmental progression, we isolated single cells from these testicular tissues and performed scRNA-seq using the 10x Genomics platform. For each donor, two separate technical replicates were performed, resulting in eight datasets. From a total of ~10,000 cells, 7,675 passed standard quality-control (QC) dataset filters and were retained for downstream analysis (see STAR Methods for details). We obtained ~200K reads/cell, which enabled the analysis of ~1,500–2,000 genes/cell (Figure S1A). The sequencing saturation rate was ~85%, and technical replicates were highly similar (r > 0.95) (Figures S1A and S1B).

To describe pubertal development and to enable comparison to other time points, we combined the juvenile datasets with our previously published adult and infant datasets, yielding a total of 13,797 single cells (after QC filtering). We first performed t-distributed stochastic neighbor embedding (tSNE) analysis on the combined datasets using the Seurat package (Butler et al., 2018; Figure 1C), which yielded eight major clusters that were subsequently annotated using known gene markers (Figure 1D; Figures S1D and S1E). Clusters 1–3 are germ cells, with C1 representing spermatogonia ($UTF1^+$, $FGFR3^+$), C2 consisting of spermatocytes ($SYCP3^+$), and C3 identifying post-meiotic spermatids ($PRM3^+$). Clusters 4–8 correspond to a heterogenous mixture of Sertoli cells (C4; $SOX9^+$), Leydig and myoid-like cells (C5; $IGF1^+$ and/or $ACTA2^+$), smooth muscle (C6; $NOTCH3^+$), macrophages (C7: $CD14^+$), and endothelial cells (C8; VWF^+), respectively (see Figures S1D and S1E for additional markers).

Distinct Phases of Spermatogonial Proliferation and Differentiation during Human Puberty

We examined changes in germ cell composition during puberty by analyzing the germ cells, following specific reclustering of initial clusters 1–3 (Figure 2A). Expression patterns of key

---

(C) tSNE and clustering analysis of single-cell transcriptome data from juvenile human testes (n = 7,680), combined with previous datasets of infant and adult scRNA-seq (Guo et al., 2018). Each dot represents a single cell and is colored according to its donor of origin. tSNE, t-distributed stochastic neighbor embedding.
(D) Expression patterns of selected markers projected on the tSNE plot (Figure 1C). For each cell cluster, one cell marker is shown in the main figure accompanied by a gallery of further markers in Figures S1D and S1E. The two top rows show somatic/niche cell markers; representative germ cell markers are shown in the two bottom rows.
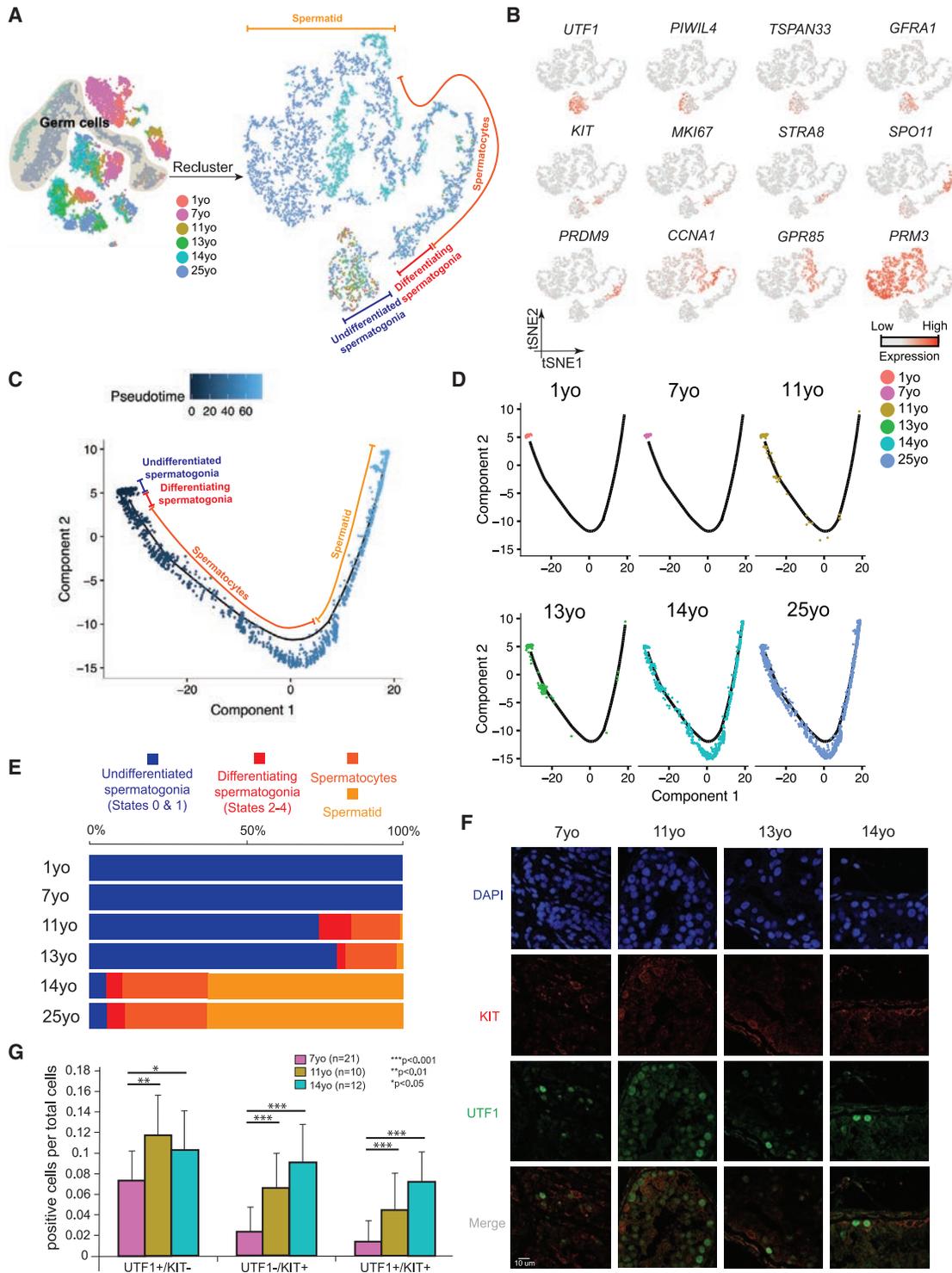See also Figure S1 and Table S1.

Figure 2. Distinct Phases of Spermatogonial Proliferation and Differentiation during Human Puberty

(A) Focused analysis (tSNE and clustering) of the germ cells (clusters C1, C2, and C3 from Figure 1C) reveals developmental progression of spermatogenesis during puberty. Cells are colored based on the ages/donors of origin.

(B) Expression patterns of known spermatogenic markers projected onto the tSNE plot from Figure 2A.

(C) Pseudotime trajectory (Monocle analysis) of the germ cells. Cells are colored based according to the predicted pseudotime.

(D) Deconvolution of the Monocle pseudotime plot according to ages/donors of origin.

(E) Relative proportion of the single cells at different spermatogenic stages in the samples analyzed.

(legend continued on next page)

markers and comparisons to prior work enable assignment of germ cells into four broad developmental stages: slowly self-renewing and undifferentiated spermatogonia (referred to as States 0–1 in [Guo et al., 2017, 2018]) marked by *UTF1*$^+$ and largely *MKI67*$^-$, differentiating spermatogonia (States 2–4) marked by *KIT*$^+$ and largely *MKI67*$^+$ (note: State 4 is preparing to enter meiosis and lacks *MKI67*), spermatocytes (from *STRA8*$^+$ to *GPR85*$^+$), and spermatids (*PRM3*$^+$) (Figures 2A and 2B). An orthogonal pseudotime analysis using the Monocle package (Qiu et al., 2017) further supports this pseudotime trajectory (Figures 2C and 2D; Figures S2A and S2B). Germ cells were then parsed out to examine their relative composition at different phases of puberty (Figures 2D and 2E). Interestingly, germ cells from both the 1- and 7-year-old samples consisted of only undifferentiated spermatogonia (corresponding to States 0–1) (Figures 2A, 2D, and 2E) that expressed *UTF1* and other early germline stem cell markers (Figure 2B; Figures S2A and S2B). In the 11-year-old sample, while a high proportion of cells were still States 0–1 spermatogonia, differentiating spermatogonia and meiotic cells also began to emerge (Figures 2D and 2E). Notably, in the infant and 7-year-old samples, spermatogonia were relatively rare (~3%–4% of total testicular cells), whereas in the 11-year-old and older samples, the relative proportion of spermatogonia increased considerably to represent ~10%–15% of total testicular cells (Figure S1C), consistent with a spermatogonial amplification and proliferative phase prior to a differentiation phase. The 13-year-old sample largely resembled the 11-year-old sample (likely reflecting the known age differences in puberty onset) though post-meiotic cells increased in proportion, indicating a more robust commitment to meiosis. Last, germ cell composition in the 14-year-old sample resembled the adult, indicating nearly full spermatogenesis (Figure 2E).

Next, we performed immunofluorescence (IF) to confirm our scRNA-seq findings (Figures 2F and 2G; Figures S2C and S2D). First, we observed UTF1$^+$ undifferentiated spermatogonia (State 0–1) at all ages analyzed. In contrast, proliferative and differentiating spermatogonia (States 2–3) display strong increases in multiple proliferative markers (e.g., cyclins, CDKs, *TOP2A*, MKI67, KIT [Figure S2E]) and MKI67$^+$ spermatogonia become apparent only from 11 years old onward, and significant levels of the meiotic marker SYCP3 were found only at/after 14 years old (Figure S2C). Co-staining for UTF1 and KIT confirmed the gradual and steady increase in KIT$^+$ spermatogonia during juvenile development (Figures 2F and 2G), indicative of progressive commitment to spermatogonial differentiation. Taken together, our transcriptomic and protein data combined with prior immunohistochemistry (IHC) studies (Paniagua and Nistal, 1984) point to three separate phases between infancy and puberty: (1) a phase where undifferentiated spermatogonia are quiescent or slowly self-renew, (2) a transient period of spermatogonial proliferation (mitosis) with limited and incomplete spermatogonial differentiation, occurring early in puberty, which gradually transitions to (3) the establishment of steady and balanced spermatogonial self-renewal and differentiation, alongside commitment to full gametogenesis.

Gene Expression Dynamics during Sertoli Cell Maturation

We next explored Sertoli cell development during puberty. As previewed above, in the pre-pubertal samples (7 years old), staining of UTF1 and SOX9 revealed cord-like structures consisting of intermingled spermatogonia and Sertoli cells (Figure 3A). On initiation of puberty (e.g., 11- and 13-year-old samples), Sertoli cells and spermatogonia align at the basement membrane of the tubules and a lumen begins to form—a pattern that developed further in the 14-year-old sample (Figure 3A). To characterize this morphological re-organization, we parsed out and examined the Sertoli cell populations (cluster 4 in Figure 1C). Here, we note that mature Sertoli cells are typically larger than the preferred size for capture in the 10x Genomics system, likely explaining the low proportion of Sertoli cells at older ages. Hence, although we obtained sufficient cell numbers to define Sertoli cell transcriptional signatures, this caveat prevents quantitation of changes in total Sertoli cell numbers during development. Our clustering analysis defined two large Sertoli clusters flanking two smaller clusters (Figures 3B and 3C). Notably, cell-cycle analysis (see STAR Methods) reveals that the large right cluster (Figures 3B and 3C) contains cells from all juvenile samples and displays a G1 phase-bias, while the left cluster is mainly composed of cells from the younger samples (1–7 years old) at different cell-cycle phases. Interestingly, Monocle pseudotime analysis also partitioned the 1- and 7-year-old Sertoli cells into two distinct states, termed Immature #1 and #2 (Figures 3D and 3E). Remarkably, these two states merge into one path that lead to mature Sertoli cells, which start emerging in samples from 11 years old onward (Figures 3D and 3E).

We observed multiple features of Immature #1 and mature Sertoli cells that distinguish them from Immature #2 cells, including high AR (Androgen Receptor) target gene expression (defined by a set of ~70 known AR-dependent genes) (Bolton et al., 2007), high mitochondrial transcription, and lower expression of ribosomal protein genes (Figure 3F). Gene Ontology (GO) analysis revealed enrichment for terms such as nucleus and transcription in Immature #1 (Figure S3H). IF co-staining for AR and SOX9 confirms this sequence of events, by showing gradual AR upregulation and co-localization in Sertoli cells as puberty proceeds (Figure 3H). Immature #2 cells have the converse properties of Immature #1 described above and are enriched in GO terms for translation and ribosome function (Figure S3H). They exhibit higher transcription of ribosomal protein genes, mitochondrial ATPases (e.g., *ATP5E*), and mitochondrial membrane proteins (e.g., *TOMM7*) and contain a higher fraction of cells in the G1 phase of the cell cycle (Figures 3F and S3E). Taken together, these two immature Sertoli cell states differ markedly in their metabolic/mitochondrial, translational, and cell-cycle properties (as indicated by transcriptional signatures).

(F) Protein co-immunofluorescence for two spermatogonial cell markers: UTF1 (States 0–1) and KIT (States 2–4) in the 4 analyzed samples. See Figure S2D for a wider field of view.

(G) Quantification of UTF1$^+$ and/or KIT$^+$ spermatogonia at different ages. The data shown are means ± SD of independent tubules. The p value was calculated via Student's t test.

See also Figure S2.
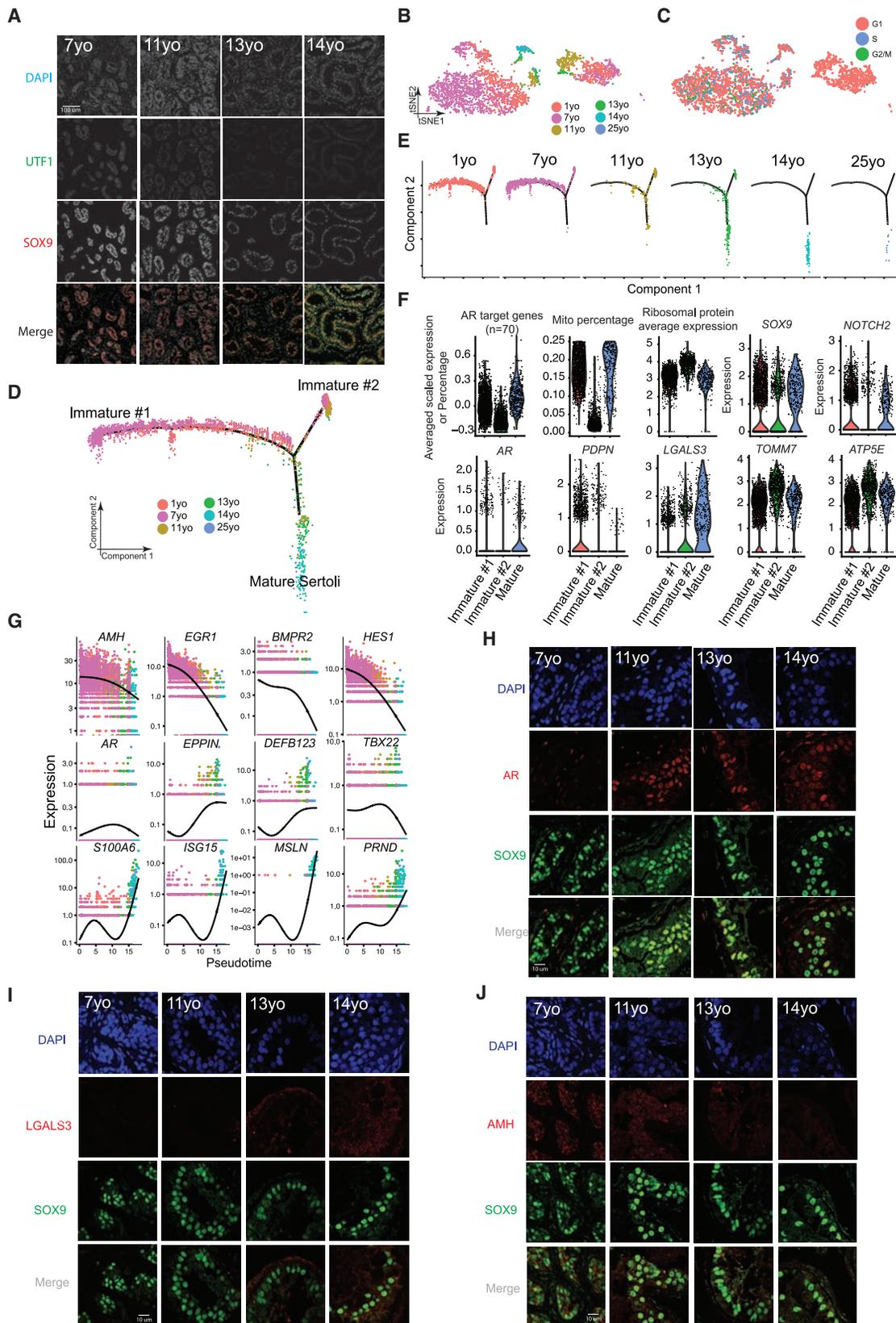
(legend on next page)

Analysis of Sertoli maturation via pseudotime and differential gene expression revealed dynamic expression of ~1,000 genes (Figure S3F) that differ between the immature and mature stages. As expected, genes associated with cytoskeleton, cell morphogenesis, and extracellular matrix were upregulated during Sertoli maturation (Griswold, 2018; Figure S3F). Genes encoding antimicrobial innate immunity peptides (including the defensin class of peptides) and immunity-related genes (e.g., *ISG15*) were also upregulated during puberty (Figures 3F, 3G, and S3G), supporting a role for Sertoli cells in protecting the testis from infection (Com et al., 2003), especially after sexual maturation. To confirm this, we performed IF/IHC staining and observed downregulation of the immature Sertoli marker AMH during puberty (Figures 3J and S3I), and upregulation of the immune peptides LGALS3 and S100A6 in Sertoli cells in the 14-year-old sample (Figures 3I and S3J). Interestingly, immunostaining of an Immature #1 marker, PDPN (Figure 3F), showed spatial separation in the 11-year-old testis (Figure S3D), suggesting that the maturation of Sertoli cells in different tubules is asynchronous and proceeds gradually. Taken together, our data describe complex developmental progression in Sertoli cell states late in puberty that involve morphogenesis, metabolism, and innate immunity.

A Common Progenitor for Leydig and Peritubular Myoid Cells

Interestingly, the clustering analysis had initially placed Leydig and myoid cells together into a single large cluster (C5; Figure 1C), prompting further exploration. Reclustering of C5 revealed that cells from the 11-year-old and younger samples largely overlapped and shared the expression of known markers of fetal Leydig and myoid precursors in the mouse (e.g., *MAFB* and *NR4A1*; Figures 4A and 4B; DeFalco et al., 2011; Wen et al., 2016), as well as heterogeneous co-expression of markers typically associated with both mature Leydig and myoid cells (e.g., *DLK1* and *ACTA2*, respectively) (Guo et al., 2018). However, in samples from 13 years old to adult, we observed a clear separation of Leydig (marked by *DLK1* and *IGF1*) and myoid cells (marked by *ACTA2* and *MYH11*). In keeping, Monocle pseudotime analysis revealed that cells from pre-puberty (1–7 years old) tightly cluster together, and the trajectory bifurcates into two clusters as puberty proceeds (Figures 4C and 4D; Figures S4C and S4D). Thus, both modes of computational analysis suggest a common expression program defining a bipotential progenitor for Leydig and myoid cells prior to puberty.

We next identified lineage-specific genes and programs, yielding ~1,000 differentially expressed genes (Figure 4E). Early precursors expressed particular genes associated with transcription (e.g., *MAFB* and *NR4A1*); as cells progress toward the myoid lineage, cytoskeleton- and cell adhesion-related genes become expressed, consistent with myoid cells forming their distinctive peritubular structure (Maekawa et al., 1996). In contrast, cells progressing along the Leydig lineage express genes involved in secretion, consistent with the known steroidogenic function of these cells (Chen et al., 2009). IF stainings revealed that ACTA2 and MYH11 signals were low or absent in the tubule lamina in the 7- and 11-year-old samples, which display a layered ring structure around the tubules from 13 years old and onward (Figures 4F and 4G). Likewise, protein expression of CYP11A1, a marker for Leydig cell steroidogenesis, progressively appears as puberty proceeds (Figure 4H).

Orthogonal Validation using Additional Juvenile Testis Samples

To further validate our results, we performed IHC on five additional infant-juvenile samples (1, 2, 4, 11, and 14 years old) (Figures S4E and S4F). In keeping with the results above, we observed progressive upregulation of AR expression during puberty, concomitant with gradual AMH downregulation as Sertoli cells mature (Figure S4E). Furthermore, in these independent samples the expression of CYP11A1 was evident only in the 14-year-old sample, indicating complete maturation of adult Leydig cells. Likewise, the myoid marker, ACTA2, displays clear laminar expression only later in puberty (14 years old, Figure S4F). These stainings provide additional confirmation for the generality of our genomics findings and validation of the 4 analyzed testis samples.
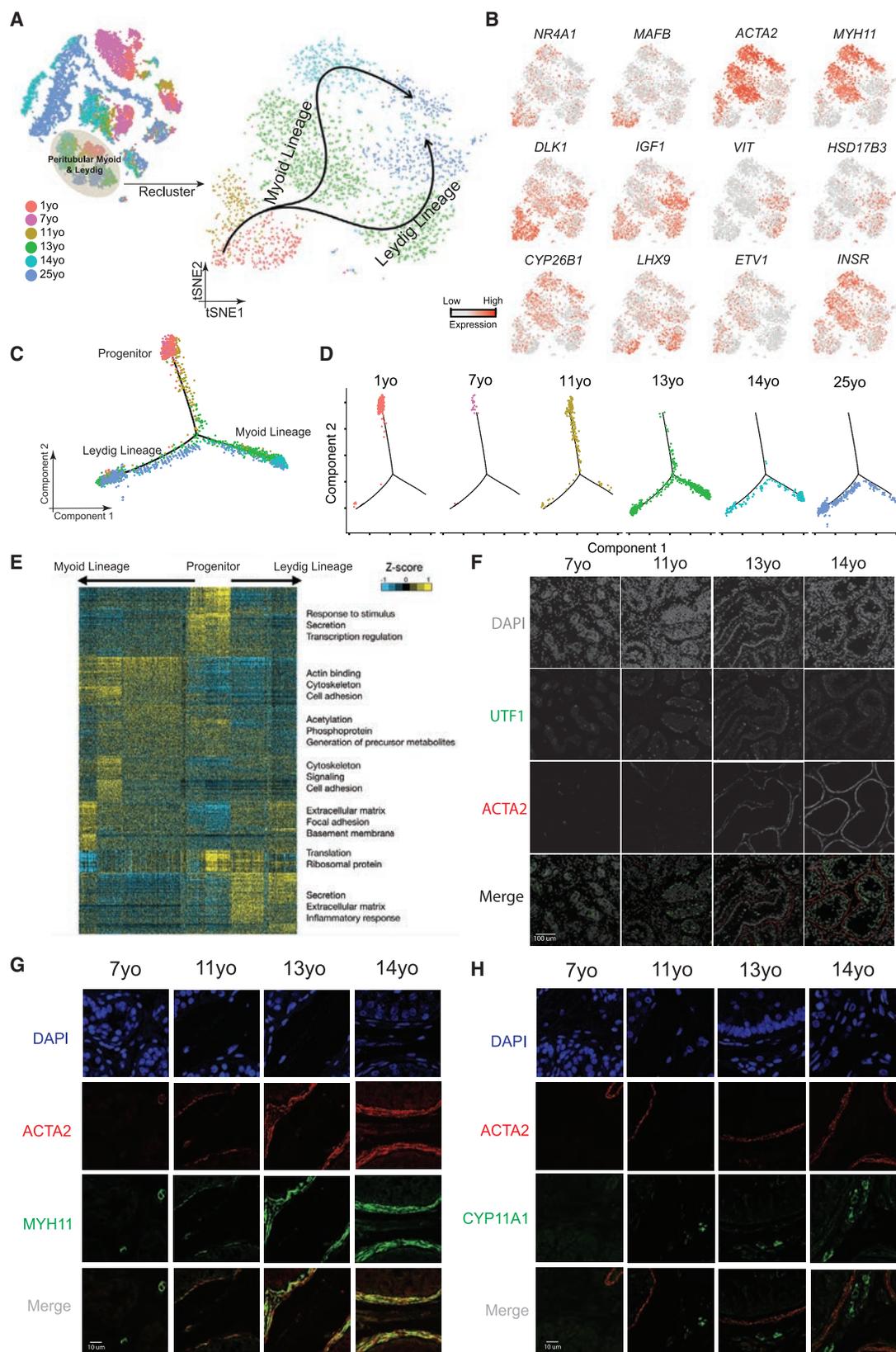
Signaling Pathways Regulating Testis Development during Puberty

To explore germ cell-niche and niche-niche interactions during puberty, we examined signaling factor relationships (Figure S5). We observed dynamic and cell-type-specific expression of genes encoding ligands, inhibitors, receptors, and gene targets from multiple signaling pathways, including retinoic acid (RA), activin/inhibin, NOTCH, GDNF, FGF, and WNT (Figures S5B–S5H). This genome-wide view confirmed known relationships, previously documented in either humans or mice, while other observations provide useful cues regarding temporal and molecular relationships during puberty. For example, as *STRA8*

Figure 3. Identification of Two Sertoli States in the Pre-pubertal Testis

(A) Immunolocalization of germ cells and Sertoli cells in the analyzed samples (7–14 years old) illustrated by co- staining with UTF1 and SOX9.

(B) Focused analysis (tSNE and reclustering) of Sertoli cells (cluster C4 from Figure 1C), with cells colored by ages/donors.

(C) Focused analysis (tSNE and reclustering) of Sertoli cells, with cells colored according to their cell-cycle phase (G1/S/G2).

(D) Pseudotime trajectory (via Monocle) of Sertoli cells revealed two distinct early (immature) cellular states that progressively converge along the pseudotime.

(E) Deconvolution of the Monocle pseudotime plot according to ages/donors of origin.

(F) Selected key genes/programs showing differential expression in the distinct Sertoli states.

(G) Expression patterns of representative dynamic genes during Sertoli cell maturation, as predicted by pseudotime.

(H) Immunofluorescent co-staining for SOX9 and AR at different ages (7–14 years old) shows an increase in AR expression during juvenile development.

(I) Immunofluorescent co-staining for SOX9 and LGALS3 at different ages (7–14 years old) supports the progressive maturation of the Sertoli cells shown by pseudotime trajectory.

(J) Immunofluorescent co-staining for SOX9 and AMH at different ages (7–14 years old) supports the gradual maturation of Sertoli cells over time shown by pseudotime trajectory.

See also Figures S3–S5 and Table S2.

A

B
NR4A1 *MAFB* *ACTA2* *MYH11*
DLK1 *IGF1* *VIT* *HSD17B3*
CYP26B1 *LHX9* *ETV1* *INSR*

Low High
Expression

C
Progenitor
Leydig Lineage
Myoid Lineage
Component 2
Component 1

D
1yo 7yo 11yo 13yo 14yo 25yo
Component 2
Component 1

E
Myoid Lineage Progenitor Leydig Lineage
Z-score
-1 0 1

Response to stimulus
Secretion
Transcription regulation

Actin binding
Cytoskeleton
Cell adhesion

Acetylation
Phosphoprotein
Generation of precursor metabolites

Cytoskeleton
Signaling
Cell adhesion

Extracellular matrix
Focal adhesion
Basement membrane

Translation
Ribosomal protein

Secretion
Extracellular matrix
Inflammatory response

F
7yo 11yo 13yo 14yo
DAPI
UTF1
ACTA2
Merge
100 um

G
7yo 11yo 13yo 14yo
DAPI
ACTA2
MYH11
Merge
10 um

H
7yo 11yo 13yo 14yo
DAPI
ACTA2
CYP11A1
Merge
10 um

(legend on next page)

expression was absent from the 7- to 11-year-old samples (Figure S5B), RA is unlikely to be involved in the transition from undifferentiated to differentiating spermatogonia during human puberty, in contrast with findings in pre-pubertal mice (Velte et al., 2019). Furthermore, our data support Activin and BMP pathways as candidate key players during puberty: we observe that Sertoli cells downregulate *INHA* as they mature, while Leydig cells express high levels of *INHBA* after puberty, leading to increased Activin and lower Inhibin activity after puberty (Figure S5C). IHC staining confirmed that INHA protein is downregulated as puberty proceeds (Figure S5D). Interestingly, activin receptors (*ACVR1B*, *BMPR1B*, and *ACVR2B*) are expressed in spermatogonia, whereas key inhibitors of Activin signaling (*FST*, *BAMBI*, and *NOG*) are specifically expressed in the undifferentiated spermatogonia (States 0 and 1). Thus, the Activin pathway appears selectively inhibited in slowly self-renewing and undifferentiated spermatogonia but is active in proliferating and differentiating spermatogonia, warranting further exploration for functional roles during spermatogonial differentiation.

Single-Cell Profiling of Testes from T-Suppressed Transfemales

Although previous data and our current analysis suggest a key role for AR and T in promoting testis development (both spermatogonia and niche cells) during puberty (Herbison, 2016; Koskenniemi et al., 2017), the molecular details involved are poorly characterized. Hence, to better define the functional role of T in the adult testis, we examined the expression profiles of testes from two adult transfemales who had been subjected to long-term reduction in T. One testis (Tf1) was from a T-suppressed 50-year-old transfemale, treated with spironolactone (a T antagonist) and estradiol for 19 months before testis removal during gender confirmation surgery. The other (Tf2) was obtained from a 26-year-old transfemale, treated with spironolactone and estradiol for 16 months before testis removal during gender confirmation surgery. In both cases, histological examination revealed major differences between the adult untreated and T-suppressed testes: macroscopically, the tubular architecture was disrupted and germ cell development was greatly impaired in the T-suppressed testes (Figure 5A). Here, scRNA-seq on isolated single cells from both T-suppressed testes was performed. For Tf1, our two technical replicates were highly similar (Figure S6A), yielding 2,161 single cells (after QC filtering). For Tf2, a single replicate yielding more than twice the cell numbers of

Tf1 was analyzed. For both Tf1 and Tf2, tSNE and clustering analysis revealed the presence of the major testicular cell types as defined by clustering and annotation with key marker genes (Figures 5B and 5C). However, we noted that the relative proportion of cell types varied considerably in the two samples (Figure S6B). Thus, a larger study that examines and controls parameters (e.g., patient ages, treatment lengths, etc.) will be required to explain all differences. Nevertheless, our analyses reveal a set of consistent findings between the transfemale samples and replicates. For example, we observed a much lower proportion (in Tf1) or absence (in Tf2) of differentiating spermatogonia (e.g., *KIT*+), spermatocytes or spermatids, whereas in both transfemale samples spermatogonia expressing undifferentiated markers (e.g., *UTF1*+) were clearly present (Figures 5B–5E; Figure 6C; Figure S6B) and appeared relatively enriched in proportion when compared to untreated samples. In keeping with our scRNA-seq results, UTF1 protein expression was observed in both the T-suppressed and the untreated testes, while MKI67 and SYCP3 signals were both significantly reduced in the T-suppressed spermatogonia (Figure 5D). Interestingly, staining for the Sertoli cell marker SOX9 revealed a distorted localization pattern in the T-suppressed testes (Figure 5E), prompting further studies to better understand how T suppression affects Sertoli cells.

T Promotes Germ Cell and Sertoli Cell Development *In Vivo*

To better understand the impact of T suppression on testicular cell development, we combined the scRNA-seq results from the two T-suppressed transfemales and those from all the 6 untreated males (from infancy through puberty into adulthood) and performed analysis (Figures 6A and 6B). Interestingly, spermatogonia derived from Tf1 and Tf2 cluster together with untreated spermatogonia (Figure 6B), suggesting that they do not transition to a new state but rather reside in state(s) present in untreated males. In keeping, examination of key markers that define spermatogonia states from the T-suppressed to the untreated testes revealed a higher proportion of undifferentiated spermatogonia (States 0 and 1) in the T-suppressed testes (Figure 6C). Further tSNE and clustering analysis of only spermatogonia demonstrated cells clustering based on "state" rather than "donor of origin" (Figures 6D and 6E). Results from two analyses further suggest that the undifferentiated spermatogonia from T-suppressed testes partition into State 0 and State 1 cells. First, we observed a clear separation of State 0 and State 1 cell

---

Figure 4. A Common Progenitor for Leydig and Peritubular Myoid Cells

(A) Focused analysis (tSNE and clustering) of the Leydig and peritubular myoid cells (cluster C5 from Figure 1C), with cells colored according to ages/donors of origin. The predicted developmental lineages are represented by the arrows.

(B) Expression patterns of key representative markers projected onto the tSNE plot from Figure 4A.

(C) Pseudotime trajectory (via Monocle) of the C5 cluster predicts a common early pre-pubertal progenitor state and two distinct developmental trajectories for the Leydig and myoid lineages during puberty.

(D) Deconvolution of the Monocle pseudotime plot according to the ages/donors of origin.

(E) K-means clustering of genes exhibiting differential expression (n = 1,005) along the Leydig and myoid cell lineages. Each row represents a gene, and each column represents a single cell, with columns/cells placed in pseudotime order defined in Figure 4C. Differential gene expression levels utilize a Z score as defined by the color key; associated GO terms (using DAVID v6.7) are given on the right of the corresponding gene clusters.

(F) Protein co-immunofluorescence for UTF1 and the peritubular myoid cell marker ACTA2 in the analyzed samples (7–14 years old) revealed that the myoid lineage (ACTA2+) is progressively specified during puberty.

(G) Protein co-immunofluorescence for two known myoid cell markers, ACTA2 and MYH11, at different ages (7–14 years old).

(H) Immunofluorescent co-staining for ACTA2 and CYP11A1 (Leydig cell marker) shows the progressive expression of them during juvenile development.

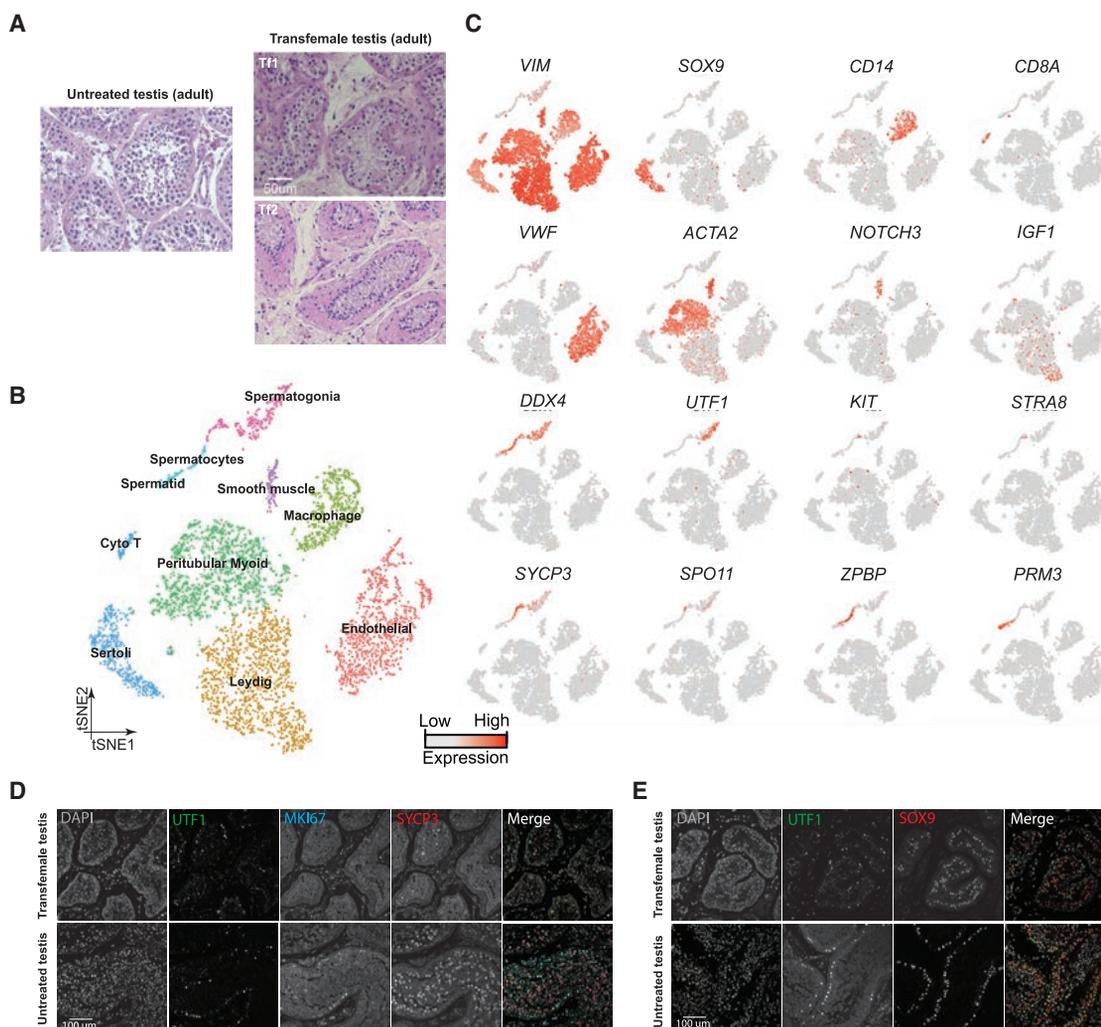See also Figures S4 and S5 and Table S3.

Figure 5. Single-Cell Transcriptome Profiling of Testes from T-Suppressed Transfemales

(A) H&E staining of the adult untreated (25 years old) and T-suppressed (Tf1 and Tf2) testicular sections.

(B) tSNE and clustering analysis of single-cell transcriptome data from two transfemale testes (n = 5,179).

(C) Expression patterns of selected markers projected on the tSNE plot. Top two rows are somatic/niche cell markers; bottom two rows are representative germ cell markers.

(D) Examination of germ cell compositions in T-suppressed (Tf1 as an example) and untreated (25 years old) testis by protein immunostaining of three germ cell markers.

(E) Immunolocalization of germ cells and Sertoli cells in T-suppressed (Tf1 as an example) and untreated (25 years old) testis by staining for UTF1 and SOX9.

See also Figure S6 and Table S4.

clusters (Figures 6D and 6E); second, State 0 or 1 cells from either the untreated or T-suppressed testes expressed similar levels of State 0 or 1 specific markers (Figure 6F, based on a 100 gene classifier). Together, these results suggest that T has limited impact on transcriptional profiles of State 0–1 spermatogonia, though its suppression impairs progression to differentiation.

Additionally, we performed a combined analysis of Sertoli cells, and found that Sertoli cells from the two T-suppressed testes resembled more the 11- to 13-year-old samples than the 14-year-old or adult samples (Figure 6G). This is further supported by the upregulation of early Sertoli markers (including *AMH* and *HES1*), and downregulation of later Sertoli markers, including immune-related genes (*S100A6*, *ISG15*) (Figure S6E).

Thus, T suppression in adults could lead to a partial reversal of Sertoli cell developmental state, mimicking aspects of the pubertal stage.

DISCUSSION

Puberty in human males involves major changes in testis weight and physiology, including development of niche cells to establish the seminiferous tubule, spermatogonial differentiation, and modulation of hormonal signaling—culminating in the establishment of steady spermatogenesis (Koskenniemi et al., 2017; Sharpe et al., 2003). To better understand this complex process at the molecular and genome-wide level, we generated the first overview of the pubertal transcriptional cell atlas at single-cell
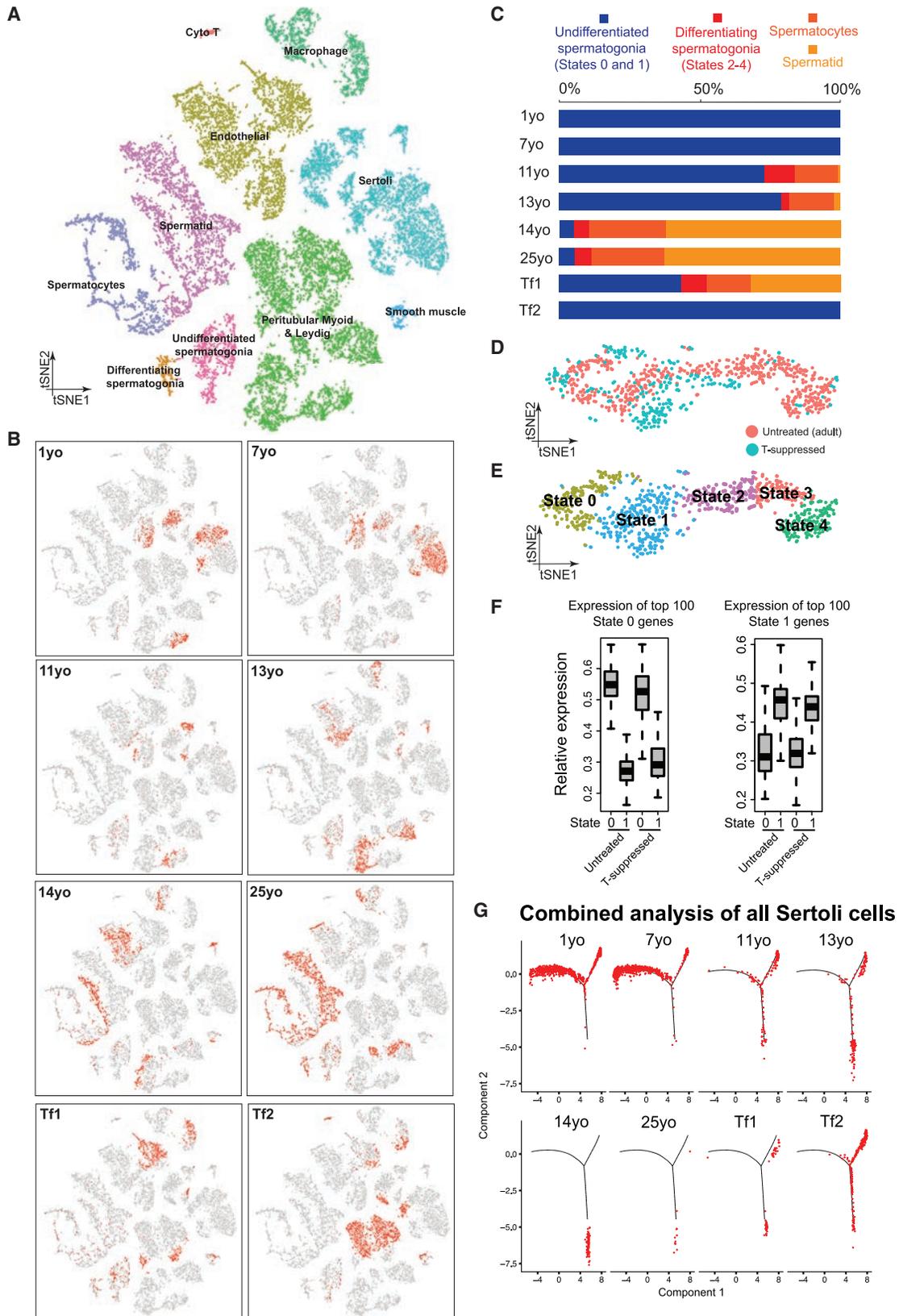
(legend on next page)

level, providing a foundational data resource coupled to multiple modes of analyses. To further facilitate data access and visualization, we have designed a website allowing browsing and query of expression patterns of genes of interest (https://humantestisatlas.shinyapps.io/humantestisatlas1/).

Regarding germ cell development, our prior dataset from adult human testes identified five cellular spermatogonial states (States 0–4) and provided evidence that States 0 and 1 correspond to the undifferentiated reserve germ cells (Guo et al., 2018). Notably, we observe a large increase (from 3% in the 7-year-old sample to ~13% in the 11-year-old sample [Figure S1C]) in the proportion of spermatogonia (relative to the total testicular cells profiled). A similar increase has been previously documented in IHC studies examining the relative numbers of type A spermatogonia (Berensztein et al., 2002; Paniagua and Nistal, 1984)—which together suggest a proliferative phase involving expansion of States 0–1 spermatogonia concomitant with seminiferous tubule reorganization and development. Of note, our scRNA-seq and protein validation do not support a simple molecular basis to account for the two histologically distinct population of A_{dark} and A_{pale} spermatogonia noted previously via histology (Clermont, 1966). Our results are consistent with recent work (Jan et al., 2017), which did not identify significant transcriptional differences within laser-capture microdissected A_{dark} and A_{pale} spermatogonia, suggesting that additional proteomic and functional work is needed to understand possible differences. Notably, tubule morphogenesis (with a defined basal lamina and lumen) coincided with the first emergence of differentiated spermatogonia (States 2–4), without completion of gametogenesis, as very few spermatids were observed. Thus, a phase of spermatogonial expansion (involving States 0-1) and initial differentiation (involving States 2–4) precedes the ability to complete spermatogenesis. Furthermore, our results from juveniles and the transfemale testes strongly suggest that States 0 and 1 are indeed reserve (undifferentiated, quiescent, or slow-cycling) spermatogonia that persist from infancy to adulthood even in the absence/suppression of T. For example, in the T-suppressed testes, while spermatogenesis is severely impaired, we observed a population of spermatogonia with the same transcriptional profile as the State 0–1 population identified in untreated adult testes (Guo et al., 2018). This likely accounts for the ability of spermatogonia in some transfemales to resume gametogenesis when T suppression is halted (Kohn et al., 2017; Schneider et al., 2017).

Interestingly, whereas AR knockout or T-suppressed rodents display a germ cell developmental block only at/after meiosis (Walker, 2011; Yeh et al., 2002), our data correlate T upregulation with the emergence of differentiating spermatogonia, as well as a role in spermiogenesis. Notably, in macaque monkeys, treatment with GnRH inhibitor for 2 weeks reduced T and impaired development beyond the undifferentiated/self-renewing (A_{dark}) spermatogonia but did not change the proportion of A_{dark} spermatogonia (O'Donnell et al., 2001; Weinbauer et al., 1998)—suggesting that both in macaques and humans spermatogonial differentiation may require T. Whether this effect is mediated by Sertoli cells, which harbor the receptor for T (AR), and/or if T directly regulate spermatogonia through an AR-independent pathway, remains unknown. Finally, despite our observations of the role of T, our pathway analyses suggest that additional ligands (e.g., Activin, NOTCH, etc.) may control human spermatogonial differentiation.

Our work reinforces prior work that the physiology of the postnatal testis is markedly different in mice versus humans. Pre-pubertal males display small testis cords lacking an apparent lamina or lumen, structures resembling those in fetal/early postnatal mouse testes, which in peri-pubertal stages progressively acquire a more tubular structure. Regarding the location of spermatogonia in these cords and nascent tubules, consistent with prior work (Paniagua and Nistal, 1984), we observe spermatogonia at both the basement membrane and within the cord/tubule in pre-pubertal samples (Figure S2F), which in peri-pubertal and subsequent stages become fully aligned with the basement membrane. Therefore, our data and analysis—together with prior work by others—suggest that the development and physiology of human spermatogonia from 1 year old through pre-puberty is very different in humans versus mice.

Regarding somatic cell development, our study reveals several insights. First, both spermatogonia and niche cell transcriptional profiles showed very little change between the 1- and 7-year-old samples—and then changed dramatically. For example, we observed (by transcriptional criteria) two distinct populations of Sertoli cells at infant-juvenile stages that differ in metabolic, mitochondrial, and cell-cycle properties—but lack major changes in transcription and chromatin factors—indicating that these states may not represent different developmental states but rather alternative physiological states. Surprisingly, these states appear to converge into a single maturing Sertoli population during puberty. Here, the expression of PDPN in the 11-year-old testis in only a subset of tubules

Figure 6. Testosterone Promotes Sertoli and Germ Cell Development *In Vivo*

(A) tSNE and clustering analysis of combined single-cell transcriptome data from T-suppressed (Tf1 and Tf2) and untreated (from infancy through puberty to adult) testis, with cells colored based on their identities. See Figure S6D for the markers used to assign the cell identities.

(B) Partitioning the combined tSNE analysis in Figure 6A based on the ages/donors of origin, with cells from each donor highlighted in red separately in different boxes.

(C) Relative proportion of cells at different spermatogenic stages in untreated testes (different ages) or T-suppressed testes.

(D and E) Comparison of spermatogonia from untreated adult (5 States as defined in Guo et al., 2018) and T-suppressed testes via tSNE analysis, with cells colored according to their T treatment (D) or spermatogonial states (E).

(F) Expression levels of spermatogonial State 0 genes (left) or State 1 genes (right) in untreated or T suppressed. Neither State 0, nor State 1 cells from untreated and T-suppressed testes showed statistically significant differences in gene expression via Wilcoxon test (p value = 0.528 [left] and 0.065 [right]).

(G) Comparison of Sertoli cells profile in all samples from T-suppressed (Tf1 and Tf2) and untreated (from infancy through puberty to adult) testes using focused pseudotime analysis (via Monocle).

See also Figure S6.

suggests that Sertoli maturation as an asynchronous and gradual process. Future studies should focus on investigating the physiological, metabolic, and functional differences between Sertoli states, as well as the roles of the immune peptides and their regulation by T. Finally, our data suggest that anti-bacterial/viral peptides may be important for protection from infection associated with sexual activity after puberty.

Importantly, we identified a common precursor for Leydig and myoid cells in humans that expresses (at low and heterogeneous levels) markers normally associated with both mature Leydig and myoid cells. We also identified certain factors known in mouse to reside in fetal somatic precursors (e.g., *MAFB*) but did not observe *NESTIN* (a known marker of Leydig precursors in the fetal mouse) during the human stages we examined (data not shown) (Kumar and DeFalco, 2018). These human Leydig/myoid precursors persist from infancy until peri-puberty and then diverge and mature as the seminiferous tubules develop. Thus, our results reveal major differences between mice and humans regarding the markers for somatic cell development and the timing of their appearance—with Leydig and myoid lineages being specified during fetal stages in mice (Svingen and Koopman, 2013) but only at pre-/peri-pubertal stages in humans. We note that T-suppressed Leydig and myoid cells displayed altered transcriptomes that were not simply developmentally regressed patterns, prompting further investigation on the effect of T on the maintenance of Leydig and myoid cell functions. Moreover, the developmental timeline differences between humans and mice may account for differences in the composition of peritubular myoid cells (multi-layered in humans versus mono-layered in mice)—differences that could be further explored in non-human primate models.

Regarding limitations, our current study profiled and analyzed four testis samples spanning human puberty. Given that age differences in puberty onset exist in humans, and that puberty is a progressive process, future studies with additional samples may reveal additional details regarding developmental processes and transitions. Likewise, given the differences observed between the two transfemales profiled here, additional studies are needed to understand the origins of the variation observed. Furthermore, our analyses and interpretations focus primarily on transcriptional data supported by initial protein validation studies, and post-transcriptional mechanisms exist that will complement and refine our understanding of the molecular strategies and the complex interplay between the different cellular components of the juvenile testis.

The human testis is one of the few organs that defines most of its cell types, physiology, and function after birth. Our work provides major advances in defining the strategy and timing of human testis development. During pre-pubertal stages, the testis maintains a pool of undifferentiated and largely quiescent germline stem cells within an immature niche. During early puberty, maturation of the niche occurs first, involving the differentiation of a common progenitor to form mature Leydig and peritubular myoid cells, which contribute to defining the lamina-luminal architecture of the seminiferous tubule to promote signaling pathways—in conjunction with hormonal induction from the hypothalamic-pituitary-gonadal axis. Likewise, Sertoli cell populations develop and change their localization, and their transcriptional, metabolic, and signaling profiles. Proliferation of

undifferentiated spermatogonia then commences to progressively populate the elongating tubules, followed by spermatogonial differentiation and the generation of the first meiotic cells, culminating in the steady generation of spermatids and mature sperm. Our data further strengthen the notion that establishment of spermatogenesis requires a complex interplay between multiple signaling pathways. These results should provide the foundation for building hypothesis-driven research that can be explored in primate models and will support improvement of *in vitro* cultures of human seminiferous tubules and spermatogonial maturation, to ultimately help guide therapeutic options for male infertility.

STAR★METHODS

Detailed methods are provided in the online version of this paper and include the following:

- KEY RESOURCES TABLE
- LEAD CONTACT AND MATERIALS AVAILABILITY
- EXPERIMENTAL MODEL AND SUBJECT DETAILS
  - Human Testicular Tissues
- METHOD DETAILS
  - Sample Storage by Cryopreservation
  - Sample Fixation for Immunostainings
  - Human Testis Sample Preparation for Single Cell RNA Sequencing
  - Single Cell RNA-seq Performance, Library Preparation and Sequencing
  - Processing of Single Cell RNA-seq Data
  - Immunostaining of Testicular Tissues
  - Immunohistochemistry staining
  - H&E staining
  - Cell counting
- QUANTIFICATION AND STATISTICAL ANALYSIS
- DATA AND CODE AVAILABILITY

SUPPLEMENTAL INFORMATION

Supplemental Information can be found online at https://doi.org/10.1016/j.stem.2019.12.005.

AUTHOR CONTRIBUTIONS

DECLARATION OF INTERESTS

REFERENCES

Bellvé, A.R., Cavicchia, J.C., Millette, C.F., O'Brien, D.A., Bhatnagar, Y.M., and Dym, M. (1977). Spermatogenic cells of the prepuberal mouse. Isolation and morphological characterization. J. Cell Biol. *74*, 68–85.

Berenszstein, E.B., Sciara, M.I., Rivarola, M.A., and Belgorosky, A. (2002). Apoptosis and proliferation of human testicular somatic and germ cells during prepuberty: high rate of testicular growth in newborns mediated by decreased apoptosis. J. Clin. Endocrinol. Metab. *87*, 5113–5118.

Birnbaum, K.D. (2018). Power in Numbers: Single-Cell RNA-Seq Strategies to Dissect Complex Tissues. Annu. Rev. Genet. *52*, 203–221.

Bolton, E.C., So, A.Y., Chaivorapol, C., Haqq, C.M., Li, H., and Yamamoto, K.R. (2007). Cell- and gene-specific regulation of primary target genes by the androgen receptor. Genes Dev. *21*, 2005–2017.

Butler, A., Hoffman, P., Smibert, P., Papalexi, E., and Satija, R. (2018). Integrating single-cell transcriptomic data across different conditions, technologies, and species. Nat. Biotechnol. *36*, 411–420.

Chemes, H.E. (2001). Infancy is not a quiescent period of testicular development. Int. J. Androl. *24*, 2–7.

Chen, H., Ge, R.-S., and Zirkin, B.R. (2009). Leydig cells: From stem cells to aging. Mol. Cell. Endocrinol. *306*, 9–16.

Clermont, Y. (1966). Spermatogenesis in man. A study of the spermatogonial population. Fertil. Steril. *17*, 705–721.

Com, E., Bourgeon, F., Evrard, B., Ganz, T., Colleu, D., Jégou, B., and Pineau, C. (2003). Expression of antimicrobial defensins in the male reproductive tract of rats, mice, and humans. Biol. Reprod. *68*, 95–104.

DeFalco, T., Takahashi, S., and Capel, B. (2011). Two distinct origins for Leydig cell progenitors in the fetal testis. Dev. Biol. *352*, 14–26.

Griswold, M.D. (2018). 50 years of spermatogenesis: Sertoli cells and their interactions with germ cells. Biol. Reprod. *99*, 87–100.

Guo, J., Grow, E.J., Yi, C., Mlcochova, H., Maher, G.J., Lindskog, C., Murphy, P.J., Wike, C.L., Carrell, D.T., Goriely, A., et al. (2017). Chromatin and Single-Cell RNA-Seq Profiling Reveal Dynamic Signaling and Metabolic Transitions during Human Spermatogonial Stem Cell Development. Cell Stem Cell *21*, 533–546.e6.

Guo, J., Grow, E.J., Mlcochova, H., Maher, G.J., Lindskog, C., Nie, X., Guo, Y., Takei, Y., Yun, J., Cai, L., et al. (2018). The adult human testis transcriptional cell atlas. Cell Res. *28*, 1141–1157.

Herbison, A.E. (2016). Control of puberty onset and fertility by gonadotropin-releasing hormone neurons. Nat. Rev. Endocrinol. *12*, 452–466.

Hermann, B.P., Cheng, K., Singh, A., Roa-De La Cruz, L., Mutoji, K.N., Chen, I.-C., Gildersleeve, H., Lehle, J.D., Mayo, M., Westernströer, B., et al. (2018). The Mammalian Spermatogenesis Single-Cell Transcriptome, from Spermatogonial Stem Cells to Spermatids. Cell Rep. *25*, 1650–1667.

Huang, W., Sherman, B.T., and Lempicki, R.A. (2009). Systematic and integrative analysis of large gene lists using DAVID bioinformatics resources. Nat. Protoc. *4*, 44–57.

Jan, S.Z., Vormer, T.L., Jongejan, A., Röling, M.D., Silber, S.J., de Rooij, D.G., Hamer, G., Repping, S., and van Pelt, A.M.M. (2017). Unraveling transcriptome dynamics in human spermatogenesis. Development *144*, 3659–3673.

Johnsen, S.G. (1970). Testicular biopsy score count–a method for registration of spermatogenesis in human testes: normal values and results in 335 hypogonadal males. Hormones *1*, 2–25.

Kanatsu-Shinohara, M., and Shinohara, T. (2013). Spermatogonial stem cell self-renewal and development. Annu. Rev. Cell Dev. Biol. *29*, 163–187.

Kluin, P.M., and de Rooij, D.G. (1981). A comparison between the morphology and cell kinetics of gonocytes and adult type undifferentiated spermatogonia in the mouse. Int. J. Androl. *4*, 475–493.

Kohn, T.P., Louis, M.R., Pickett, S.M., Lindgren, M.C., Kohn, J.R., Pastuszak, A.W., and Lipshultz, L.I. (2017). Age and duration of testosterone therapy predict time to return of sperm count after human chorionic gonadotropin therapy. Fertil. Steril. *107*, 351–357.e1.

Koskenniemi, J.J., Virtanen, H.E., and Toppari, J. (2017). Testicular growth and development in puberty. Curr. Opin. Endocrinol. Diabetes Obes. *24*, 215–224.

Kumar, D.L., and DeFalco, T. (2018). A perivascular niche for multipotent progenitors in the fetal testis. Nat. Commun. *9*, 4519.

Lindskog, C. (2016). The Human Protein Atlas—an important resource for basic and clinical research. Expert Rev. Proteomics *13*, 627–629.

Lun, A.T.L., McCarthy, D.J., and Marioni, J.C. (2016). A step-by-step workflow for low-level analysis of single-cell RNA-seq data with Bioconductor. F1000Res. *5*, 2122.

Maekawa, M., Kamimura, K., and Nagano, T. (1996). Peritubular myoid cells in the testis: their structure and function. Arch. Histol. Cytol. *59*, 1–13.

O'Donnell, L., Narula, A., Balourdos, G., Gu, Y.Q., Wreford, N.G., Robertson, D.M., Bremner, W.J., and McLachlan, R.I. (2001). Impairment of spermatogonial development and spermiation after testosterone-induced gonadotropin suppression in adult monkeys (Macaca fascicularis). J. Clin. Endocrinol. Metab. *86*, 1814–1822.

Paniagua, R., and Nistal, M. (1984). Morphological and histometric study of human spermatogonia from birth to the onset of puberty. J. Anat. *139*, 535–552.

Plant, T.M. (2015). Neuroendocrine control of the onset of puberty. Front. Neuroendocrinol. *38*, 73–88.

Qiu, X., Mao, Q., Tang, Y., Wang, L., Chawla, R., Pliner, H.A., and Trapnell, C. (2017). Reversed graph embedding resolves complex single-cell trajectories. Nat. Methods *14*, 979–982.

Schneider, F., Kliesch, S., Schlatt, S., and Neuhaus, N. (2017). Andrology of male-to-female transsexuals: influence of cross-sex hormone therapy on testicular function. Andrology *5*, 873–880.

Sharpe, R.M., McKinnell, C., Kivlin, C., and Fisher, J.S. (2003). Proliferation and functional maturation of Sertoli cells, and their relevance to disorders of testis function in adulthood. Reproduction *125*, 769–784.

Sohni, A., Tan, K., Song, H.-W., Burow, D., de Rooij, D.G., Laurent, L., Hsieh, T.-C., Rabah, R., Hammoud, S.S., Vicini, E., and Wilkinson, M.F. (2019). The Neonatal and Adult Human Testis Defined at the Single-Cell Level. Cell Rep. *26*, 1501–1517.e4.

Svingen, T., and Koopman, P. (2013). Building the mammalian testis: origins, differentiation, and assembly of the component cell populations. Genes Dev. *27*, 2409–2426.

Tharmalingam, M.D., Jorgensen, A., and Mitchell, R.T. (2018). Experimental models of testicular development and function using human tissue and cells. Mol. Cell. Endocrinol. *468*, 95–110.

Velte, E.K., Niedenberger, B.A., Serra, N.D., Singh, A., Roa-DeLaCruz, L., Hermann, B.P., and Geyer, C.B. (2019). Differential RA responsiveness directs

formation of functionally distinct spermatogonial populations at the initiation of spermatogenesis in the mouse. Development 146, dev173088.

Vergouwen, R.P., Huiskamp, R., Bas, R.J., Roepers-Gajadien, H.L., Davids, J.A., and de Rooij, D.G. (1993). Postnatal development of testicular cell populations in mice. J. Reprod. Fertil. 99, 479–485.

Walker, W.H. (2011). Testosterone signaling and the regulation of spermatogenesis. Spermatogenesis 1, 116–120.

Wang, M., Liu, X., Chang, G., Chen, Y., An, G., Yan, L., Gao, S., Xu, Y., Cui, Y., Dong, J., et al. (2018). Single-Cell RNA Sequencing Analysis Reveals Sequential Cell Fate Transition during Human Spermatogenesis. Cell Stem Cell 23, 599–614.e4.

Weinbauer, G.F., Schubert, J., Yeung, C.H., Rosiepen, G., and Nieschlag, E. (1998). Gonadotrophin-releasing hormone antagonist arrests premeiotic germ cell proliferation but does not inhibit meiosis in the male monkey: a quantitative analysis using 5-bromodeoxyuridine and dual parameter flow cytometry. J. Endocrinol. 156, 23–34.

Wen, Q., Cheng, C.Y., and Liu, Y.-X. (2016). Development, function and fate of fetal Leydig cells. Semin. Cell Dev. Biol. 59, 89–98.

Yeh, S., Tsai, M.-Y., Xu, Q., Mu, X.-M., Lardy, H., Huang, K.-E., Lin, H., Yeh, S.-D., Altuwaijri, S., Zhou, X., et al. (2002). Generation and characterization of androgen receptor knockout (ARKO) mice: an in vivo model for the study of androgen functions in selective tissues. Proc. Natl. Acad. Sci. USA 99, 13498–13503.

Yoshida, S., Sukeno, M., Nakagawa, T., Ohbo, K., Nagamatsu, G., Suda, T., and Nabeshima, Y. (2006). The first round of mouse spermatogenesis is a distinctive program that lacks the self-renewing spermatogonia stage. Development 133, 1495–1505.

STAR★METHODS

KEY RESOURCES TABLE

REAGENT or RESOURCE	SOURCE	IDENTIFIER
Antibodies		
Mouse monoclonal anti-UTF1 Dilution: 1:100 - 1:1000	Millipore	cat# Mab4337 (5G10.2), RRID:AB_827541
Rat polyclonal anti-MKI67 Dilution: 1:100	Abcam	cat# ab15580, RRID:AB_443209
Rabbit monoclonal anti-MKI67 Dilution: 1:200	Abcam	cat# ab16667, RRID:AB_302459
Mouse polyclonal anti-ACTA2 Dilution: 1:400	Abcam	cat# ab5694, RRID:AB_2223021
Mouse monoclonal anti-ACTA2 Dilution: 1:300	Atlas Antibodies	cat# cab013531, RRID:AB_2677383
Mouse polyclonal anti-ACTA2 Dilution: 1:250	Sigma Aldrich	cat# A2547, RRID:AB_476701
Mouse monoclonal anti-AMH Dilution: 1:300	Santa Cruz	cat# sc-166752 RRID:AB_2289536
Mouse monoclonal anti-AR Dilution: 1:300	Atlas Antibodies	cat# CAB000001, RRID:AB_2685535
Rabbit monoclonal anti-AR Dilution: 1:250	Abcam	cat# ab133273, RRID:AB_11156085
Goat polyclonal anti-KIT Dilution: 1:25	R&D systems	cat# AF332, RRID:AB_355302
Rabbit polyclonal anti-INHA Dilution: 1:1000	Atlas Antibodies	cat# HPA019141, RRID:AB_1851789
Mouse monoclonal anti-LGALS3 Dilution: 1:500	Santa Cruz	cat# sc-32790, RRID:AB_627657
Rabbit polyclonal anti-MYH11 Dilution: 1:100	Atlas Antibodies	cat# HPA015310, RRID:AB_1854261
Rabbit polyclonal anti-S100A6 Dilution: 1:750	Atlas Antibodies	cat# HPA007575, RRID:AB_1079859
Rabbit polyclonal anti-SOX9 Dilution: 1:1000	Millipore	cat# AB5535, RRID:AB_2239761
Rabbit monoclonal anti-SOX9 Dilution: 1:300	Abcam	cat# ab185966, RRID:AB_2728660
Rabbit monoclonal anti-SYCP3 Dilution: 1:400	Abcam	cat# ab15093, RRID:AB_301639
Rabbit polyclonal anti-CYP11A1 Dilution: 1:250	Atlas Antibodies	cat# HPA016436, RRID:AB_1847423
Mouse polyclonal anti-PDPN Dilution: 1:500	Abcam	cat# ab77854, RRID:AB_1566117
Donkey anti-Mouse IgG (H+L) Highly Cross-Adsorbed Secondary Antibody, Alexa Fluor 488	Thermo Fisher Scientific	cat# A21202, RRID:AB_141607
Donkey anti-Goat IgG (H+L) Highly Cross-Adsorbed Secondary Antibody, Alexa Fluor 555	Thermo Fisher Scientific	cat# A21432, RRID:AB_141788
Donkey anti-Rabbit IgG (H+L) Highly Cross-Adsorbed Secondary Antibody, Alexa Fluor 488	Thermo Fisher Scientific	cat# A31573, RRID:AB_141788
Donkey anti-Mouse IgG (H+L) Highly Cross-Adsorbed Secondary Antibody, Alexa Fluor 555	Thermo Fisher Scientific	cat# A31570, RRID:AB_2536180
Biological Samples		
Human testis samples for donors	DonorConnect	NA
Human testis samples from transfemale	Universityf of Utah Andrology laboratory	NA
Human testis samples for immunohistochemistry	MRC Centre for Reproductive Health, The Queen's Medical Research Institute, The University of Edinburgh and Royal Hospital for Children and Young People	NA
Deposited Data		
Single cell RNA-seq for pre- and peri-pubertal human testes	This paper	GEO: GSE134144
Single cell RNA-seq for transfemale testes	This paper	GEO: GSE134144
Software and Algorithms		
Seurat (2.3.4)	Butler et al., 2018	https://satijalab.org/seurat/
Monocle (2.10.1)	Qiu et al., 2017	http://cole-trapnell-lab.github.io/monocle-release/
GO (David 6.7)	Huang et al., 2009	https://david-d.ncifcrf.gov
Cell Ranger (2.2.0)	NA	https://support.10xgenomics.com/single-cell-gene-expression/software/pipelines/latest/what-is-cell-ranger

REAGENT or RESOURCE	SOURCE	IDENTIFIER
Cluster 3.0	NA	http://bonsai.hgc.jp/~mdehoon/software/cluster/software.htm
scran (1.6.5)	Lun et al., 2016	https://bioconductor.org/packages/3.7/bioc/vignettes/scran/inst/doc/scran.html
Other		
Single cell RNA-seq for infant and adult human testes	Guo et al., 2018	GEO: GSE120508
The Human Protein Atlas	Lindskog, 2016	http://www.proteinatlas.org

LEAD CONTACT AND MATERIALS AVAILABILITY

Further information and requests for reagents should be directed to and will be fulfilled by the Lead Contact, Bradley R. Cairns (brad.cairns@hci.utah.edu). This study did not generate new unique reagents.

EXPERIMENTAL MODEL AND SUBJECT DETAILS

Human Testicular Tissues
Pre- and peri-pubertal human testicular samples were obtained from four healthy boys aged 7, 11, 13 and 14 years old, through the University of Utah Andrology laboratory and Connect Donor (formerly named Intermountain Donor Services). Those samples were removed from deceased individuals who consented to organ donation for transplantation and research.

Transfemale (testosterone-suppressed) samples were obtained through the University of Utah Andrology laboratory consented for research (IRB approved protocol #00075836).

Pre- and peri-pubertal tissues for orthogonal validation studies were obtained from males undergoing testicular tissue cryopreservation for fertility preservation with prior ethical approval from the South East Scotland Research Ethics Committee (Reference: 13SS/0145).

METHOD DETAILS

Sample Storage by Cryopreservation
Once collected, the pair of whole-testis was transported to the research laboratory on ice in saline or Hank's Balanced Salt Solution (HBSS; GIBCO cat # 24020117) and processed within 1 hour of removal by surgery. Around 90% of each testis was divided into smaller portions (~500 mg – 1g each) using scissors and directly transferred into cryovials (Corning cat # 403659) in DMEM medium (Life Technologies cat # 11995073) containing 10% DMSO (Sigma-Aldrich cat # D8779), 15% fetal bovine serum/FBS (GIBCO cat # 10082147) and cryopreserved in Mr. Frosty container (Thermo Fisher Scientific cat #5100-0001) at a controlled slow rate, and stored at −80°C for overnight. Cryovials were transferred to liquid nitrogen for long-term storage.

Sample Fixation for Immunostainings
Around 10% of the remaining testis tissues were placed in 1X PBS containing 4% paraformaldehyde/PFA (Thermo Fisher Scientific cat # 28908) and incubated overnight at 4C with agitation on a rotor (60 rpm). Fixed samples were then washed with three times in cold PBS, and stored in PBS at 4C until immunostaining processing.

Human Testis Sample Preparation for Single Cell RNA Sequencing
For each single-cell sequencing experiment, 1 or 2 cryovials were thawed quickly. Tissues were then washed twice with PBS, and subject to digestion as described previously (Guo et al., 2018). For pubertal samples, tissues were washed twice in 1 x PBS, and minced into small pieces for better digestion outcome. Tissues were then treated with trypsin/ethylenediaminetetraacetic acid (EDTA; Invitrogen cat # 25300054) for 20-25 min and collagenase type IV (Sigma Aldrich cat # C5138-500MG) at 37°C. For the transfemale samples, tissues were digested following the standard two step enzymatic isolation protocol as described in (Guo et al., 2018). The digestion was then stopped by adding 10% FBS (GIBCO cat # 10082147). Single testicular cells were obtained by filtering through 70 μm (Fisher Scientific cat # 08-771-2) and 40 μm (Fisher Scientific cat # 08-771-1) strainers. The cells were pelleted by centrifugation at 600 g for 15 min, and wash with PBS twice. Cell number was counted using hemocytometer, and the cells were then resuspended in PBS + 0.4% BSA (Thermo Fisher Scientific cat # AM2616) at a concentration of ~1,000 cells/uL ready for single-cell sequencing.

Single Cell RNA-seq Performance, Library Preparation and Sequencing
Here, we aimed to capture ~4,000-5,000 cells. Briefly, cells were diluted following manufacturer's instructions, and 33.8 uL of total mixed buffer together with cells were loaded into 10x Chromium Controller using the Chromium Single Cell 3′ v2 reagents. The

sequencing libraries were prepared following the manufacturer's instructions, using 13 cycles of cDNA amplification, followed by an imput of ~100 ng of cDNA for library amplification using 12 cycles. The resulting libraries were then sequenced on a 2 X 100 cycle paired-end run on an Illumina HiSeq 2500 or Novaseq 6000 instruments.

Processing of Single Cell RNA-seq Data
Raw data were demultiplexed using mkfastq application (Cell Ranger v2.2.0) to make Fastq files. Fastq files were then run with count application (Cell Ranger v2.2.0) using default settings, which performs alignment (using STAR aligner), filtering and UMI counting. The UMI count tables were used for further analysis.

Immunostaining of Testicular Tissues
The immunofluorescence (IF) stainings were performed on 5μm formalin-fixed paraffin embedded (FFPE) or cryopreserved sections from portions of the collected testicular samples following deparaffinisation, rehydratation and heat-mediated antigen retrieval in 10mM sodium citrate buffer solution (pH 6). After treatment with Superblock (PBS) Blocking Buffer (Thermo Fisher Scientific, cat# 37515) for 30 mins, individual sections were incubated overnight at 4°C with a mix of diluted antibodies (for antibodies details and dilutions, see the Key Resources Table). Antigen detection was conducted using the appropriate combination of Alexa Fluor 488 and 555 secondary antibodies (all 1:500; Thermo Fisher Scientific, cat#A21202, cat#A21432, cat#A31570, cat#A21206, respectively) for 2 hr at room temperature in the dark. All primary/secondary antibodies were diluted in SignalBoost Immunoreaction Enhancer Kit (Calbiochem, cat#407207-1KIT). After three washes in PBS, sections were incubated with DAPI (4',6-Diamidine-2-phenylindole dihydrochloride) (Roche, cat#10236276001) to facilitate nuclear visualization (dilution 1:2000). Specificity of the antibody staining was confirmed using the same protocol but with omission of primary antibodies. Following multiple washes in PBS, slides were mounted using Vectashield mounting medium for fluorescence (Vector Laboratories, Inc., Burlingame, CA, cat#H-1000). Images were obtained under 25x objective (LD LCI PA 25x/0.8 DIC WD = 0.57 mm Imm Corr (UV)VIS-IR (Oil-Immersion) with a Zeiss LSM 780 Upright Multi-Photon Confocal Microscope and analyzed using ImageJ software (NIH, Bethesda, MD, USA).

Immunohistochemistry staining
For validation using the four pubertal samples, immunohistochemistry on 5 μm sections from FFPE or cryopreserved testis samples was performed using the Rabbit specific HRP/DAB (ABC) Detection IHC Kit (Abcam, cat# 236466). Briefly, after deparaffinisation, rehydration and heat-mediated antigen retrieval in 10mM sodium citrate buffer solution (pH 6), sections were blocked with Protein block and incubated overnight at 4°C with a variety of different antibodies in 1x TBS. Subsequently, sections were incubated with HRP conjugate before chromogenic detection using DAB (3,3′Diaminobenzidine). Nuclei were counterstained with hematoxylin (Poly Scientific, cat#s212A), slides mounted in Aquatex (Merck, cat#108562) and images were acquired using the Hamamatsu NanoZoomer slide scanner and the NDP.view 2 software (Hamamatsu Photonics).

For validation in additional human testis tissue samples, immunohistochemistry was performed on Bouin's fixed, paraffin-embedded tissue sections of approximately 5μm thickness. The sections were deparaffinized with xylene and rehydrated in ethanol using a reducing concentration from 100% to 70% (20secs each). Between each step sections were washed in TBS. If required, heat-mediated antigen retrieval in 10mM citrate buffer, pH6 was performed in a pressure cooker. Sections were cooled in TBS and endogenous peroxidase activity was blocked in 3% (v/v) hydrogen peroxide (VWR International) in methanol (Fisher Chemicals) for 30mins. Sections were blocked in Normal Horse Serum (Diagnostics Scotland) diluted (1:5) in TBS with 5% Bovine Serum Albumin (Sigma Aldrich). Sections were incubated in primary antibody diluted in blocking serum overnight in a humidified chamber at 4°C. The following day, sections were incubated with the relevant Impress HRP secondary antibody at room temperature for 30mins. Visualization of staining was performed using DAB (1drop/ml) diluted in buffer. Sections were counterstained with Haematoxylin for 2.5mins, Scott's tap water for 30 s and dehydrated by gradual introduction to ethanol from 70% to 100% (20secs each) and Xylene (2x 5mins). Sections were mounted using Pertex (CellPath). Brighfield images were captured using the ZEISS Axio Scan.Z1 at 20x magnification.

H&E staining
For hematoxylin and eosin (H&E) staining, deparaffinized and rehydrated 5 μm sections were incubated in hematoxylin for 3 min and rinsed with running tap water for 5 min. Afterward, the sections were dipped in acid alcohol (0,5% v/v hydrochloric acid in 70% ethanol), washed with distilled H2O, and incubated in eosin (Poly Scientific, cat#176) for 30 s. The sections were dehydrated before mounting with Histomount (National Diagnostics, cat# 12954910).

Johnsen scores are the standard quantitative/clinical histological grading system utilized by testis pathologists, which assesses the degree of spermatogenic maturation in individual tubular cross-sections, ranging between 1 to 10, with 1 representing complete azoospermia, and 10 representing full spermatogenesis(Johnsen, 1970).

Cell counting
For quantification of UTF and/or KIT expressing cells, single-positive and double-positive cells were counted in cross-sections of seminiferous tubules. The number of positive cells per cross-section were normalized to the total number of cells located in the periphery of the seminiferous tubule. The bars represent means + SD of independent tubules. Data were analyzed using unpaired two-sided Student's t test. $p < 0.05$ was considered statistically significant.

QUANTIFICATION AND STATISTICAL ANALYSIS

The Seurat program (https://satijalab.org/seurat/, R package, v.2.3.4) was used as a first analytical package. To start with, UMI count tables from both replicates from all four juvenile donors were loaded into R using Read10X function, and Seurat objects were built from each experiment. Each experiment was filtered and normalized with default settings. Specifically, cells were retained only if they contained > 500 expressed genes, and had < 25% reads mapped to mitochondrial genome. We first run t-SNE and clustering analysis on each replicate, which resulted in similar t-SNE map. Data matrices from different donors and replicates were then combined with the previously published infant and adult data (Guo et al., 2018). Next, cells were normalized to the total UMI read counts, as instructed in the tutorial (http://satijalab.org/seurat/). t-SNE and clustering analyses were performed on the combined data using the top 6,000 highly variable genes and 1-30 PCs, which showed the most significant p values.

Detailed pseudotime for different cell types were performed using the Monocle package (v2.10.1) following the default settings. After pseudotime coordinates/order were determined, gene clustering analysis was performed to establish the accuracy of pseudotime ordering. Here, cells (in columns) were ordered by their pseudotime, and genes (in rows) were clustered by k-means clustering using Cluster 3.0. Different k-mean numbers were performed to reach the optimal clustering number. Cell cycle analysis was performed using scran program (https://bioconductor.org/packages/3.7/bioc/vignettes/scran/inst/doc/scran.html, R Package; v1.6.5).

DATA AND CODE AVAILABILITY

All software tools can be found online (see Key Resources Table). The accession number for all sequencing data reported in this paper is GEO: GSE134144.